Electronic Thesis and Dissertation Repository

12-5-2012 12:00 AM

Controlled Synthesis of One Dimensional Nanostructured Materials and Their Applications as Catalyst Supports in Proton Exchange Membrane Fuel Cells

Mohammad Norouzi Banis
The University of Western Ontario

Supervisor
Xueliang (Andy) Sun
The University of Western Ontario

Follow this and additional works at: https://ir.lib.uwo.ca/etd

⬤ Part of the Ceramic Materials Commons, and the Nanoscience and Nanotechnology Commons

Recommended Citation

CONTROLLED SYNTHESIS OF ONE DIMENSIONAL NANOSTRUCTURED
MATERIALS AND THEIR APPLICATIONS AS CATALYST SUPPORTS IN
PROTON EXCHANGE MEMBRANE FUEL CELLS

(Spine Title: Nanostructured Catalyst Supports for Fuel Cells)

(Thesis format: Integrated Article)

by

Mohammad Norouzi Banis

Graduate Program in Mechanical and Materials Engineering

A thesis submitted in partial fulfillment
of the requirements for the degree of
Doctor of Philosophy

The School of Graduate and Postdoctoral Studies
The University of Western Ontario
London, Ontario, Canada

© Mohammad Norouzi Banis 2012

THE UNIVERSITY OF WESTERN ONTARIO
School of Graduate and Postdoctoral Studies

CERTIFICATE OF EXAMINATION

Supervisor

_____
Dr. Xueliang (Andy) Sun

Supervisory Committee

_____
Dr. Jun Yang

_____
Dr. Robert Klassen

Examiners

_____
Dr. Liying Jiang

_____
Dr. Zhifeng Ding

_____
Dr. Xianguo Li

_____
Dr. Jun Yang

The thesis by

Mohammad Norouzi Banis

entitled:

Controlled Synthesis of One Dimensional Nanostructured Materials and Their Applications as Catalyst Supports in Proton Exchange Membrane Fuel Cells

is accepted in partial fulfillment of the
requirements for the degree of
Doctor of Philosophy

_____   _____
            Date   Chair of the Thesis Examination Board

Abstract

Nanomaterials have attracted significant interest in the past decade due to their unique structure and properties compared to their bulk counterparts. Nanomaterials-based solutions can address challenges in various technologies such as proton exchange membrane fuel cells (PEMFCs). PEMFC is an innovative energy conversion technology to directly convert chemical energy to electrical energy by using hydrogen as fuel. However, the current PEMFC system still faces significant technological roadblocks which have to be overcome before the system can become economically viable. A major impediment to the commercialization of PEMFC is the high cost of materials and manufacturing and stability, which is primarily associated with the cost of Pt catalysts and their support in membrane electrode assembly (MEA). One approach in addressing these issues is the controlled synthesis and application of nanostructured Pt-based catalysts and their support in PEMFCs. The objective of this thesis is to synthesize and characterize various nanostructures (e.g. metal oxides and metal silicides or composites) and evaluate their performance as Pt supports used in the PEMFCs. Various advanced characterization techniques such as high resolution scanning and transmission electron microscopy, X-ray absorption spectroscopy and electrochemical characterization methods have been used to understand growth mechanism of obtained nanostructures and their roles in PEMFCs.

We also reported the synthesis of WSi_2 and Ta_5Si_3 heterostructures using a low pressure chemical vapor deposition (LPCVD) method. The morphologies of these nanostructures were found to be sensitive to the concentration of reactive species and silica vapor in the CVD chamber. The results indicated that the morphology of WSi_2 and Ta_5Si_3 nanostructures varied from nanowires, networked nanoribbons to nanosheets with the control of the oxygen concentration. A vapor solid growth mechanism based on silica sheath formation was proposed for the synthesis of these nanostructures.

To take advantage of unique properties of carbon nanotubes, metal oxide and metal silicides as catalyst support, a new method was developed for the synthesis of composite nanostructures. $TiSi_2O_x$-NCNTs and TiO_2-NCNTs nanocomposites were synthesized using a combination of CVD process and magnetron sputtering and their performance as catalyst

supports in PEMFCs were studied. Pt nanoparticles deposited on these nanostructures showed enhanced catalytic activity compared to commercial Pt/carbon electrodes. The electronic structure of Pt on the catalyst supports was investigated using X-ray absorption spectroscopy, to obtain insight into the interaction between the catalyst supports and Pt nanoparticles.

As an example of well controlled synthesis of nanostructures, one-dimensional tungsten oxide nanostructures ($W_{18}O_{49}$) have been synthesized using a conventional chemical vapor deposition method (CVD). The morphology of the nanostructures such as diameter and length, were controlled during the synthesis process via sulfur doping. The dependence of morphology, composition and structure of tungsten oxides on the sulfur flow rate has been studied. Further, one step synthesis of tungsten sulfide/tungsten oxide nanocables ($WS_2/W_{18}O_{49}$) have been achieved for the first time using tungsten and sulfur powder as the starting materials.

In summary, the research work presented in this thesis aims at contributing to the development of various novel nanostructured catalyst supports and probing the correlation between synthesis approach, fine structure, and catalytic performance of the nanostructures as well as exploring their potential applications in highly active electrocatalysts for PEMFCs.

Keywords: Nanomaterials, Tungsten oxide nanowires, Core shell nanostructures, Nanosheet, Networked nanoribbons, Metal silicide, Chemical vapor deposition, Electrocatalyst support, Composite catalyst support, Proton exchange membrane fuel cells, Oxygen reduction reaction, Methanol oxidation reaction, Co tolerance, X-ray absorption spectroscopy

Co-Authorship Statement

1. Title: One-step tunable Controlled synthesis of pristine, sulfur-doped $W_{18}O_{49}$ nanowires and long $WS_2/W18O_{49}$ nanocables

Authors: Mohammad Norouzi Banis, Yong Zhang, Ruying Li, and Xueliang Sun

All the experimental and theoretical work was carried out by Mohammad Norouzi Banis under the guidance of Dr. Xueliang Sun. The initial draft and the followed modification of this manuscript were conducted by Mohammad Norouzi Banis under the supervision of Dr. Xueliang Sun. The other coauthors contributed to the formation of the final version with discussion and related characterization. The final version of this manuscript is to be submitted for publication.

2. Title: $TiSi_2O_x$ coated N-doped Carbon Nanotubes for the Oxygen Reduction Reaction in Proton Exchange Membrane Fuel Cells (PEMFCs)

Authors: Mohammad Norouzi Banis, Shuhui Sun, Xiangbo Meng, Yong Zhang, Ruying Li, Mei Cai, Tsun-Kong Sham and Xueliang Sun

All the experimental and theoretical work was carried out by Mohammad Norouzi Banis under the guidance of Dr. Xueliang Sun. The initial draft and the followed modification of this manuscript were conducted by Mohammad Norouzi Banis under the supervision of Dr. Xueliang Sun. The other coauthors contributed to the formation of the final version with discussion and related characterization. The final version of this manuscript is to be submitted for publication.

3. Title: TiO_2 Nanoparticle Decorated Nitrogen Doped Carbon Nanotubes as Pt Catalyst Support for Low Temperature Fuel Cells

Authors: Mohammad Norouzi Banis, Shuhui Sun, Yong Zhang, Ruying Li, Mei Cai, Tsun-Kong Sham and Xueliang Sun

All the experimental and theoretical work was carried out by Mohammad Norouzi Banis under the guidance of Dr. Xueliang Sun. The initial draft and the followed modification of

this manuscript were conducted by Mohammad Norouzi Banis under the supervision of Dr. Xueliang Sun. The other coauthors contributed to the formation of the final version with discussion and related characterization. The final version of this manuscript is to be submitted for publication.

4. Title: Spatial Sequential Growth of Various WSi_2 Networked Nanostructures and Mechanisms

Authors: Mohammad Norouzi Banis, Xiangbo Meng, Yong Zhang, Mei Cai, Ruying Li, and Xueliang Sun

All the experimental and theoretical work was carried out by Mohammad Norouzi Banis under the guidance of Dr. Xueliang Sun. The initial draft and the followed modification of this manuscript were conducted by Mohammad Norouzi Banis under the supervision of Dr. Xueliang Sun. The other coauthors contributed to the formation of the final version with discussion and related characterization. The final version of this manuscript is to be submitted for publication.

5. Title: Tailoring Growth of Single Crystalline Complex Ta_5Si_3 Nanostructures: From Networked Nanowires to Nanosheets

Authors: Mohammad Norouzi Banis, Yong Zhang, Mei Cai, Ruying Li, and Xueliang Sun

All the experimental and theoretical work was carried out by Mohammad Norouzi Banis under the guidance of Dr. Xueliang Sun. The initial draft and the followed modification of this manuscript were conducted by Mohammad Norouzi Banis under the supervision of Dr. Xueliang Sun. The other coauthors contributed to the formation of the final version with discussion and related characterization. The final version of this manuscript is to be submitted for publication.

DEDICATION

This thesis is dedicated to my beloved family, my mother, father, brother and my wife. My mother and father, you have always been my pillar of support, helping me purse my dreams. I am always indebted to you and can't imagine how to repay all your kindness. My brother, you have been my best friend throughout my life making it fun to live. My beloved wife, you have supported me in this journey, making it enjoyable and memorable, thank you for being here.

I LOVE YOU

Acknowledgments

This Ph.D. thesis work was carried out in Dr. Sun's Nanomaterial and Clean Energy lab at the University of Western Ontario, Canada. I would like to express my most sincere gratitude to all those who supported me during my Ph.D. work.

First and foremost, I would like to express my sincere gratitude to my supervisor, Dr. Xueliang Sun, a professor in Department of Mechanical and Materials Engineering at UWO, for providing me with the opportunity to work under his supervision and his continual encouragement and support throughout the whole course of my graduate studies. I am indebted to him for his kindness, patience and guidance during my studies. I would not have been able to complete my work without his extensive and comprehensive help. He has been great mentor, teacher, friend and a role model as an excellent scientist.

I am also very grateful to Mrs. Ruying (Kathy) Li, a research engineer in the group and Dr. Sun's wife. She has been supporting and encouraging me from the day I arrived in UWO. I have learned a lot from her during these years and she has had an important role in my graduate life in UWO. I really appreciate Mrs. Li and Prof. Sun's kind help and support in my life.

I would like to thank Dr. Sham, a professor in Department of Chemistry at UWO, for providing me with the opportunity to work with him and expand my area of study. I am grateful for all his support and advice throughout my studies.

Many thanks to Dr. Yong Zhang, a fellow in Dr. Sun's group, for his support and help during my graduate studies. I have learned a lot from our valuable discussions and working together.

I would like to thank my advisory committee members in MME at UWO for their advices and support in my studies in every stage. I would like to also thank the examiners of my thesis defense for their careful examination and insightful suggestions and comments and discussions.

Table of Contents

List of Tables

List of Figures

xvi

List of Abbreviations

0D: zero dimensional

1D: one dimensional

2D: two dimensional

3D: three dimensional

C

CB: carbon black

CLS: Canadian light source

CNTs: carbon nanotubes

CO: carbon monoxide

CP: carbon paper

CV: cyclic voltammetry

CVD: chemical vapor deposition

D

DMFC: direct methanol fuel cell

E

ECSA: electrochemical surface area

EDS: energy dispersive X-ray spectroscopy

EXAFS: extended X-ray absorption fine structure

F

FCC: face-centered cubic

FCs: fuel cells

FWHM: full width at half maximum

G

GM: general motors

H

HAADF: high angle annular dark field

HRTEM: high resolution transmission electron microscopy

HXMA: hard X-ray micro-analysis

I

ICP-OES: inductively coupled plasma-optical emission spectroscopy

M

MCFC: molten carbonate fuel cell

MEA: membrane electrode assembly

MOR: methanol oxidation reaction

MWCNTs: multiwall carbon nanotubes

N

NCNTs: nitrogen-doped carbon nanotubes

NPs: nanoparticles

NNRs: networked Nanoribbons

NSs: nanosheets

NNWs: networked Nanowires

NWs: nanowires

O

ORR: oxygen reaction reduction

P

PAFC: phosphoric acid fuel cell

PECVD: plasma enhanced CVD

PEMFCs: proton exchange membrane fuel cells

PVD: physical vapor deposition

R

RHE: reversible hydrogen electrode

S

SAED: selected area electron diffraction

SEM: scanning electron microscopy

SMSI: strong metal support interaction

SOFC: solid oxide fuel cell

SWCNTs: single-walled carbon nanotubes

SR: synchrotron-radiation

T

TEM: transmission electron microscopy

X

XAS: X-ray absorption spectroscopy

XANES: X-ray absorption near edge structure

XPS: X-ray photoelectron spectroscopy

XRD: X-ray diffraction

Chapter 1

1   Introduction

1.1   Nanomaterials

In recent years, significant interest has been focused on nanotechnology and related fields. This surge in the study of nanoscale systems is due to the promise of addressing challenges in existing industries and novel technologies via development of nanotechnologies. The emergence of nanosensors[1], faster and more efficient electronic systems and stronger and lighter structures[2] are examples of developments in nanoscience and nanotechnologies. With the growing research in these areas, general definitions for phrases such as nanotechnology, nanoscience is required. A nanometer is 10^{-9} meter. Figure 1.1 illustrates a length scale which better puts nanostructured materials (nanomaterials) into context.

Among various descriptions of nanotechnology, the definition presented by the Royal Society of London is the most generalized which reads:

"Nanoscience is the study of phenomena and manipulation of materials at atomic, molecular scale where properties differ significantly from those at a large scale. Nanotechnologies are the design, characterization and application of structures, devices and systems by controlling shape and size at nanometer scale."[3]
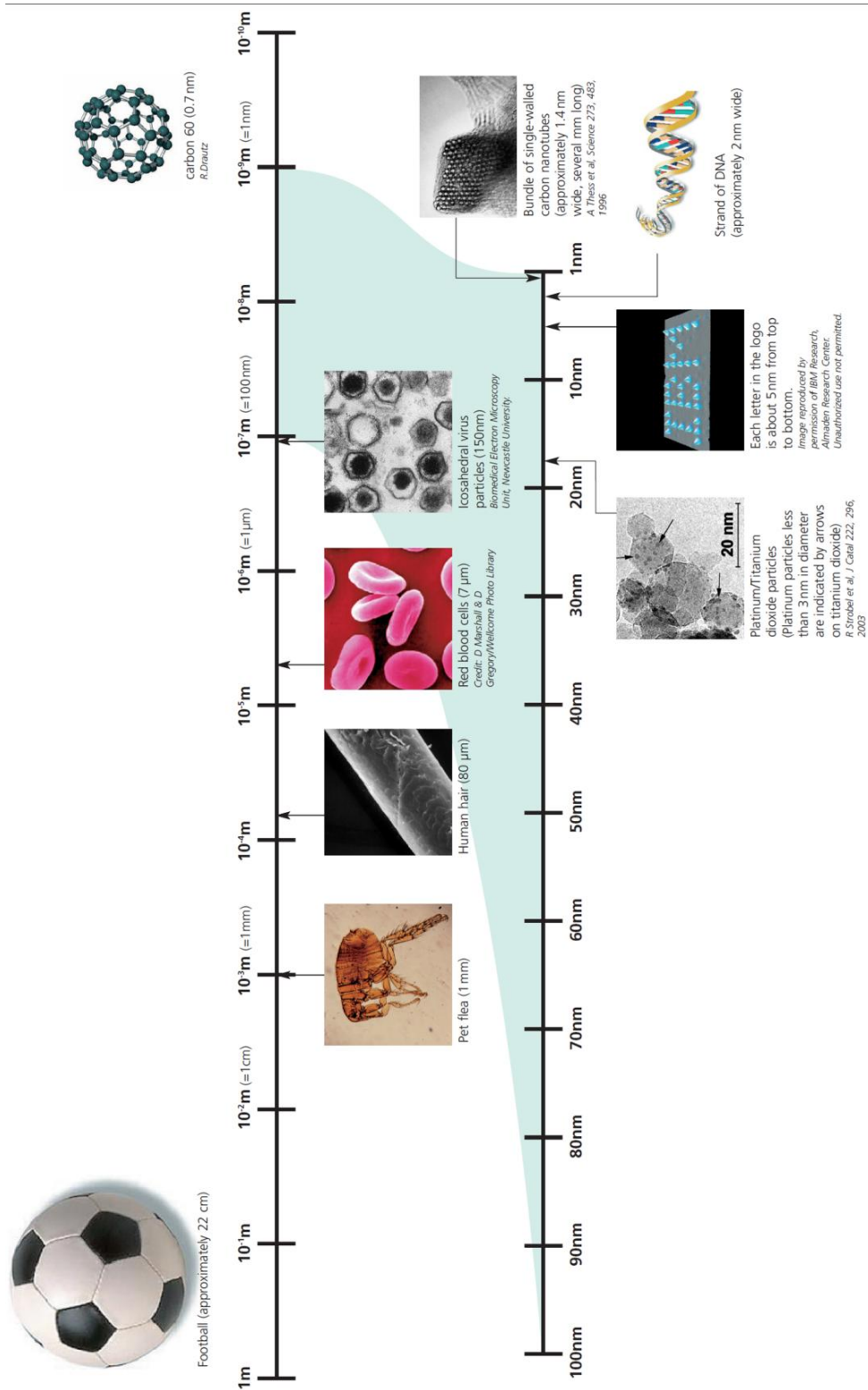
Figure 1.1 Length scale, illustrating nanoscale material compared to other scales [3].

Nanotechnology might be considered a new field of study, but the application of nanomaterials can be found in nature and man-made artifacts dating back to Roman Empire, where glass makers were fabricating glasses containing nanosized metal clusters. The metal nanoparticles in the glass enabled the production of variety of colors in the window glasses of medieval cathedrals. The advances in photography in eighteen and nineteen centuries depended on the production of silver nanoparticles. Furthermore, use of colloidal gold has a long history as it was used for treatment of arthritis, and a number of diseases were diagnosed by the interaction of these nanomaterials with spinal fluids obtained from the patient [4].

Many examples of nanomaterials can also be found in nature. Examples of nanomaterials in nature can be found in the form of milk a nanoscale colloid to more complex structures such as DNA and proteins controlling various biological reactions [3].

Nanomaterials are considered as the building blocks of any nanotechnology based systems. A general description of nanomaterials is the material with at least one dimension in nanoscale (1- 100nm). To date there has been considerable research on the synthesis and characterization of various types of nanostructures. This growing interest in the nanomaterials is due to the possibility of change in the size dependent properties of material in nanoscale, such as optical, electrical, chemical, magnetic and other chemical and physical properties. Exploiting these possibilities will result in the novel application and enhancement of current technologies. The changes in the properties of nanomaterials arise from the fact that when materials are synthesized at nanoscale, there are major changes in the electronic structure of the material, which is partly due to the high surface to volume ratio.

Studies have shown that nanomaterials exhibit some remarkable properties compared to their bulk counterparts. It has been shown that many nanomaterials such as gold show lower melting point than their bulk form [5]. Figure 1.2 shows the relationship between the Au particle radius and its melting point. Researchers have shown that nanomaterials

have superior mechanical properties compared to bulk materials [6]. For example, ZnO nanowires have shown to have 5 times higher fracture strains of those exhibited in bulk material [7]. Nanomaterials such as platinum (Pt) [8,9], gold (Au) [10] and ruthenium (Rh) [11] have been shown to exhibit higher catalytic activity for various reactions. Furthermore, detailed experimental and theoretical studies have shown that the shape and morphology of materials in nanoscale influences their properties. Research has shown that, different crystal plane of Pt nanomaterial has a different catalytic activity, thus the shape of Pt nanomaterials affects its overall electrochemical activity [12,13].
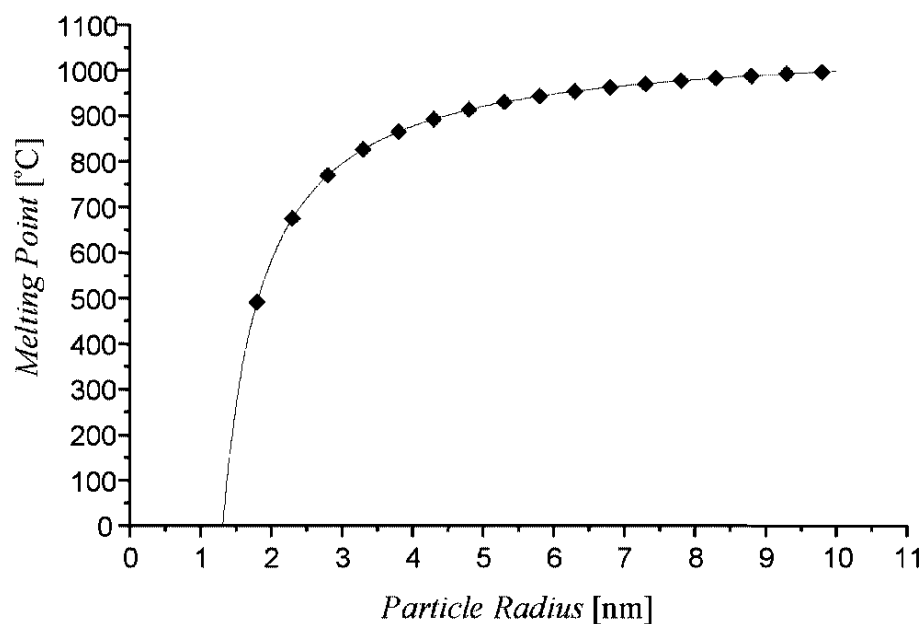
Figure 1.2 The dependence of Au melting point on the nanoparticle size [5].

1.1.1 Nanomaterial Classification

Based on their dimensions, nanomaterials are generally classified into three groups:

a) Zero dimensional nanostructures (0D) – nanoparticles

b) One dimensional nanostructures (1D) – nanowires and nanotubes

c) Two dimensional nanostructures (2D) – thin films

Compared to mature thin film technology, 0D and 1D nanostructures have attracted more substantial interest in recent years.

1.1.1.1   0D Nanomaterial (Nanoparticles)

0D nanomaterials have been synthesized from a wide range of materials, such as metal, ceramic and polymer based materials. These nanomaterials have various shapes and morphologies such as cubes, core shell and hollow spheres, having a high surface to volume ratio [12,13]. Nanoparticles have been used in many applications such as medical for cancer treatment [14], catalyst for different reactions [12,13], chemical and biological sensors [15] and optical devices [16].

Nanoparticles can be divided into different types according to their physical and chemical properties. For example metallic nanoparticles have been used for catalysts in electrochemical applications such as fuel cells [12,13]. Pt [12], Pd [13] and Au [17] single component nanoparticles have been extensively studied as active catalyst for various fuel cells. It has been shown that nanoparticle size affects their catalytic activity towards electrochemical reactions[12,13]. Furthermore, alloyed nanoparticles and composite nanoparticles such as Pt/Ni [18], CuPt [19], FeN/C [20], Pt/Au [21] and core shell structures have also been shown to act as suitable catalysts in these reactions [13].

Semiconductor, metal, carbon and polymer [22] based nanoparticles have also found application in biological technologies including bio-imaging, bio-sensing and drug delivery. Doped and un-doped ZnO nanoparticles have been prepared for bio imaging

applications. These nanoparticles were processed and surface treated to be bio-compatible and showed intense photoluminescence emission in the UV-blue region [23]. Researchers have studied the use of magnetic nanoparticle-polymer composites for controlled drug delivery. These studies focused on poly methylmethacrylate containing a magnetite or cobalt nanoparticles [24].

Studies have also indicated that optical properties of both metal and semiconductor nanoparticles can be tuned throughout the visible and near infrared region of the spectrum as a function of nanoparticle size, shape composition and local environment, making them potential material for biological and chemical sensing applications [25,26].

With the synthesis of novel nanomaterials, novel types of nanostructures are emerging continuously such as composite nanomaterials and hetero-nanostructures.

1.1.1.2   1D Nanomaterial

1D nanomaterials, including nanowires and nanotubes are structures with two dimensions in the nanoscale range. Compared to other structures (nanoparticles and thin films), these nanomaterials are the most recent type of nanostructures that have attracted growing interest in the past decade since "1D systems are the smallest dimension structures that can be used for efficient transport of electrons and optical excitations, and are thus expected to be critical to the function and integration of nanoscale devices." [27]. 1D nanomaterials can be classified into two major groups based on their structure and morphology: i) nanowires and ii) nanotubes.

i) Nanotubes

Nanotubes are structures which have a hollow cavity inside forming tubular structures. There have been many reports of organic and inorganic nanotubes to this date. Carbon

nanotubes (CNTs) are a good example of such nanotubes. Following the discovery of carbon nanotubes in 1991 [28], synthesis and application of carbon nanotubes have received tremendous attention due to their superior mechanical properties, unique electronic and chemical behaviors [28–32]. For example, CNTs are 100 times stronger than steel and show electrical conductivity of 4 times higher than copper [4]. Research on these nanostructures has brought about major advances in a wide range of fields and applications such as chemistry, electronics and medicine [30,32–34]. CNTs exhibit unique chemical and physical properties.

CNTs have also been proposed as potential candidates for electrodes in Li-ion batteries [35]. Researchers have shown that CNTs can also be used as catalyst supports enhancing the performance of low temperature fuel cells [36]. In addition, CNTs have been studied for hydrogen storage [37], chemical, biological sensors and controlled drug delivery [34].

The factor which distinguishes nanotubes from other types of 1D and 0D nanomaterials is that the surface and bulk atoms are positioned in almost similar chemical and physical environment in nanotubes. This enables a uniform behavior from the nanostructures in surface sensitive properties such as superconducting and luminescence.

To understand the origin of unique properties of nanotubes, their structure has been studied extensively [29,32,38,39]. CNTs are considered as cylinder formed by rolling up graphite sheets [4]. Depending on the number of walls, these nanostructures are divided into single wall carbon nanotubes (SWNTs) and multi walled carbon nanotubes (MWCNTs). SWNTs are formed by rolling up a single graphite plane forming a tube like structure and MWCNTs are formed from several coaxial graphite tubes as shown in Figure 1.3. It has been shown that the electrical properties of SWNTs are highly dependent on the arrangement of its atoms or the rolling direction of the graphite layer [4]. SWNTs can be either metallic or semiconductors depending on chirality, while MWCNTs are always metallic.

In recent years, studies have been moving towards tuning the properties of CNTs by introducing foreign elements into the structure and doping the CNTs [40–42]. Nitrogen doped carbon nanotubes (NCNTs) are a typical example of these studies [41]. It has been shown that NCNTs provide more active chemical surface compared to pristine CNTs [43]. The addition of nitrogen into the CNTs structure also affects the electrical properties of CNTs [41].
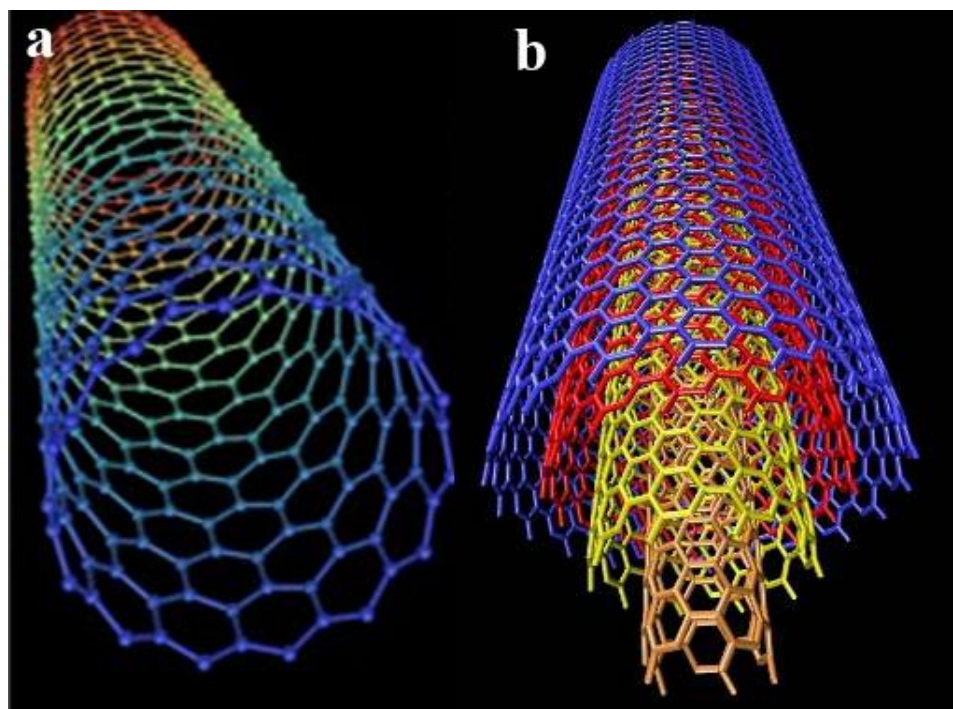
Figure 1.3 Schematic diagram of a) single walled carbon nanotubes and b) Multiwalled carbon nanotubes.

Compared to CNTs, research on the synthesis and characterization of other inorganic nanotubes (INTs) is still at the starting block [30–32]. WS2, MoS_2, BN and TiO_2 are typical examples of INTs, which show some similarities but also some difference from CNTs. For example, unlike CNTs, BN nanotubes are wide band gap semiconductors, independent of the physical structures [44]. It has been shown that WS_2 nanotubes are good candidates for solid state lubricants and as shock resistant material [45,46]. Furthermore, WS_2 nanostructures have been studied for application in Li-ion batteries

[47] and polymer nanocomposites applications. Studies have shown that addition of WS_2 nanomaterial increases the thermal stability of composites. BN nanotube containing nanocomposites have also been prepared showing an enhanced mechanical performance [32]. TiO_2 nanotube arrays have been synthesized for solar cell application, showing enhancement in the cell efficiencies [48]. INTs have also been investigated as material for gas sensing purposes [32].

ii) Nanowires

Nanowires are part of 1D nanomaterial with solid structures, which are regarded as model material for studying the relations between electrical transport, optical and other properties with dimensionality and size confinement. These nanomaterials are expected to play important roles as interconnects, functional components in the fabrication of nanoscale electronic and optoelectronic devices and electrochemical applications. Recently a variety of inorganic materials from elements, oxides, nitrides and carbides have been synthesized and characterized via various methods [49–51]. Metal oxide nanowires such as WO_x nanowires have been shown to be good supports in fuel cell applications [52]. SnO_2 nanowires have been studied as electrodes for Li-ion battery applications [53]. TiO_2 nanowires have been investigated for their photoluminescence properties and ultraviolet sensors [54]. Metal carbides such as WC_x have been shown to have catalytic properties for various reactions [55]. In addition, element nanowires such as Pt nanowires have been shown to have higher catalytic activity compared to Pt nanoparticles for electrochemical reactions such as oxygen reduction reaction [56,57].

To strengthen the functionalization of nanomaterials, hetero-nanostructures and composite nanostructures with complex architecture have recently become the focus of intensive research [58–60]. Figure 1.4 shows an example of these nanostructures. These nanomaterials include, branched nanowires [61], networked nanobelts [62], core-shell nanowires [32], nano-dendrites and nanosheets [63]. These nanomaterials that take

advantage of different classes of nanomaterial have been shown to have exhibited enhanced properties compared to their single component counter parts [56,60,64].
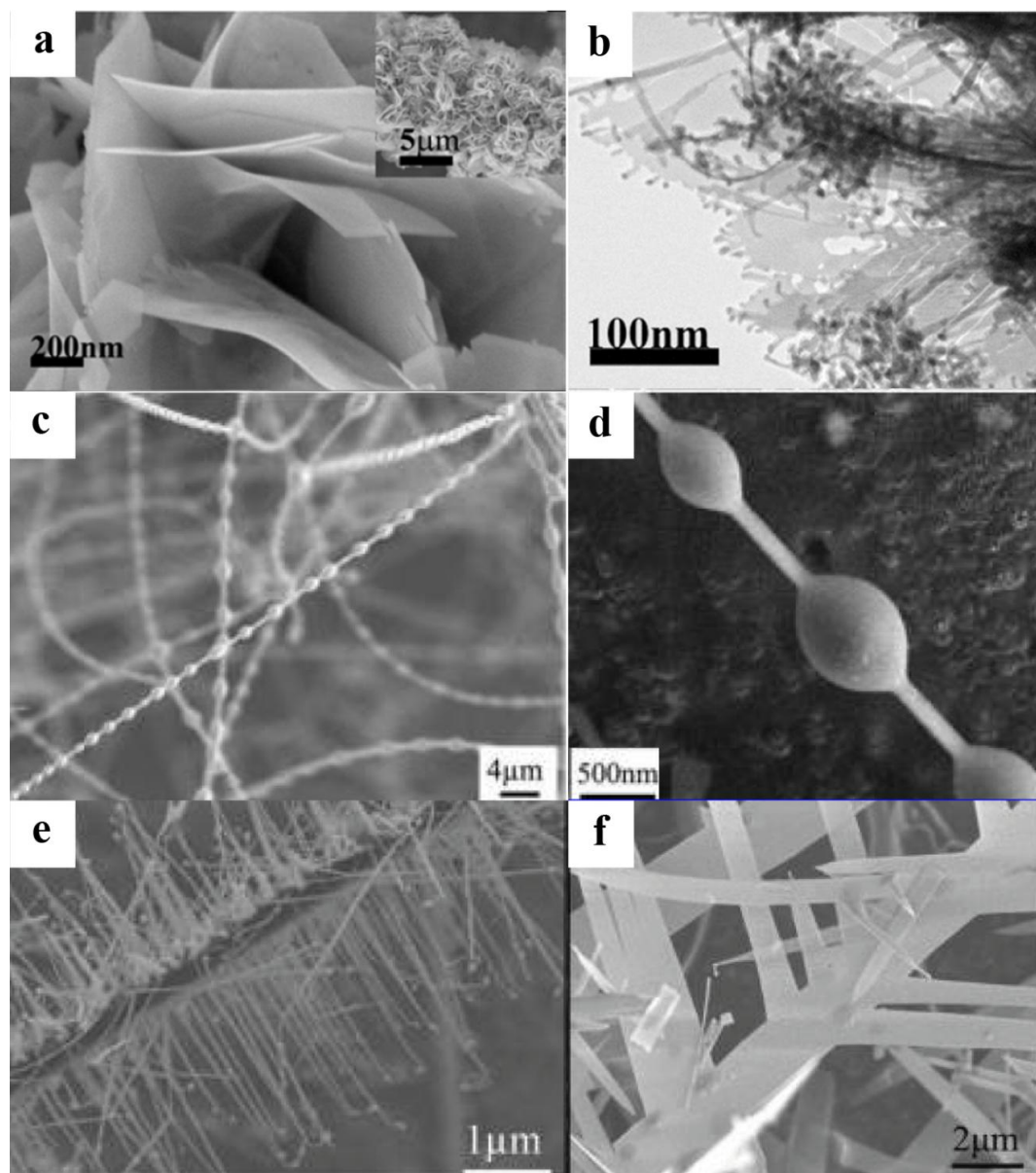
Figure 1.4 Examples of nanostructures material. a, b) WSi₂ nanosheets, c, d) MgAl₂O₄ nanochains [59], e, f) Hierarchical Al₂O₃ nanobelts [60].

In order to better study the unique properties of nanomaterials and wide spread application of these structures in various technologies, several challenges have to be

addressed. Controlled synthesis of nanomaterials with defined size, morphology and composition is one of these issues. To address these challenges, various synthesis methods have been studied and growth mechanisms have been proposed to better understand the formation of nanomaterials. In the following sections various growth mechanisms and synthesis methods have been described for the synthesis mainly 0D and 1D nanomaterials.

1.1.2 Nanomaterial Synthesis Process

To this date, various methods have been developed for the synthesis of 1D and 0D nanomaterials. However, most of these methods can be divided into two major groups of i) liquid, and ii) vapor based methods.

i) Liquid Based Methods

Liquid based methods are processes in which nanostructures are synthesized in a liquid via specific chemical reaction, deposition or template. Liquid based synthesis methods provide a suitable environment for controlled synthesis of nanostructures with various morphologies. Compared to vapor based methods, solution based methods operate at relatively lower temperature. With advances in microwave assisted growth methods the synthesis time has been greatly decreased making solution based methods, attractive for the synthesis of novel nanostructures.

0D nanomaterial are mainly synthesized using solution based methods. Pt nanoparticles with various shapes and sizes have been prepared via wide range of reactions [9,13]. They are commonly prepared by reducing a Pt salt with hydrogen [9,12,13], ethanol [65], formic acid [66] and sodium borohydride [67]. Pt nanocubes have been synthesized by reduction using ethylene glycol and polyvinylpyrrolidone in the presence of Ag as a catalyst [13]. Synthesis of alloy and composite nanoparticles has also been reported using similar methods [13].

There have been also many reports on the synthesis of 1D nanostructures via liquid based methods. In these processes 1D nanostructures are synthesized using anisotropic growth resulting from the crystallographic structure of the material, by template confinement, suitable capping agent or kinetically controlled by supersaturation [49,50].

Synthesis of Pt nanowires has been reported using reduction of Pt salt via formic acid [57]. There are many reports of synthesis of metal, metal oxide and sulfide such as Au, Ag, Pt, ZnO, SnO_2, CdS and CNTs that have been synthesized using template method [50]. Anodic alumina membranes are one of the most common templates used for the synthesis of 1D nanostructures.

Vapor Based Methods

Vapor based methods are a major part of synthesis processes of nanomaterials. These methods are mostly developed for the synthesis of 2D and 1D nanomaterials. Vapor based methods are generally based on the evaporation of the source materials, their transport in vapor phase to the reaction zone and deposition of nanomaterials based on specific growth mechanisms. The advantage of vapor based method is the possibility of large scale production using these methods. In addition, in contrast to solution based methods, a much wider range of nanostructures can be synthesized. Synthesis of compounds susceptible to oxidation in liquid environment such as metal silicides is limited to vapor based methods. The main difference between vapor phase methods is the source evaporation techniques. Vapor based methods include: chemical vapor deposition (CVD), plasma enhanced CVD (PECVD), laser ablation, atomic layer deposition, magnetron sputtering and molecular beam epitaxy (MBE). The synthesis process of most nanomaterials using vapor based techniques, as different as they may seem, follows a few well known growth mechanisms.

1.1.2.1 Growth Mechanism

The synthesis process of nanomaterials can be altered to induce the activation of certain growth mechanism, leading to a controlled growth of desired nanostructures. In the following section, typical growth mechanisms dominated in vapor based methods have been briefly reviewed.

i) Vapor-Liquid-Solid (VLS) mechanism

This growth mechanism was first reported for the growth of Si single crystals in 1964 [50]. Since the early studies on 1D nanomaterial, VLS has been widely applied for the synthesis of a variety of nanostructures such as Si, ZnO, SnO_2 and SiO_2. Figure 1.5 shows a schematic diagram of the VLS growth mechanism. In this process, the growth of 1D nanostructures are promoted by a catalyst seed [49,50]. Based on this mechanism, at high temperatures, vapor from the source material is transported to the catalysts containing substrates. The metal catalysts at high temperature form liquid alloy droplets by adsorbing vapor species. In the synthesis environment, the diffusion of vapor species into the liquid droplet continues, until the concentration of the components in the liquid alloy exceeds the equilibrium concentration based on their phase diagram. At this state the liquid droplet is supersaturated and this drives the precipitation of the solid components at the solid liquid interface.
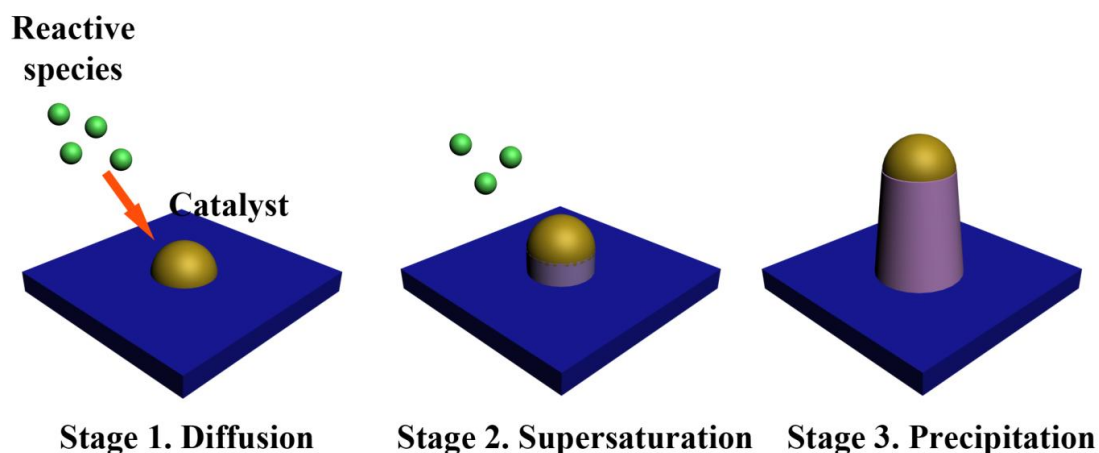
Figure 1.5 Schematic diagram of a vapor liquid solid growth mechanism.

In this mechanism the growth of the nanostructures is dependent on the vapor supply and chemical state of the catalyst. The diameter and position of the nanostructures are controlled via the catalysts droplet diameter and position. As an example of this mechanism, Wu et al[68], explained the growth of Ge nanowires using Au clusters, based on the Ge-Au phase diagram shown in figure 1.6a. A real time observation of Ge nanowire growth was conducted in situ high temperature electron microscope to confirm the proposed VLS growth mechanism (shown in figure 1.6b).

The synthesis of nanostructures using this mechanism requires several conditions. The requirements of this mechanism include:

1) Catalyst and source material: by knowing the equilibrium phase diagram one can predict the catalyst material and growth conditions of the VLS approach.

2) Method to vaporize the source material and melt the catalyst.

Nanostructures grown by this method often have certain features which help identify their growth mechanism. For example most nanowires synthesized by VLS process have an alloy droplet at their tip [50].
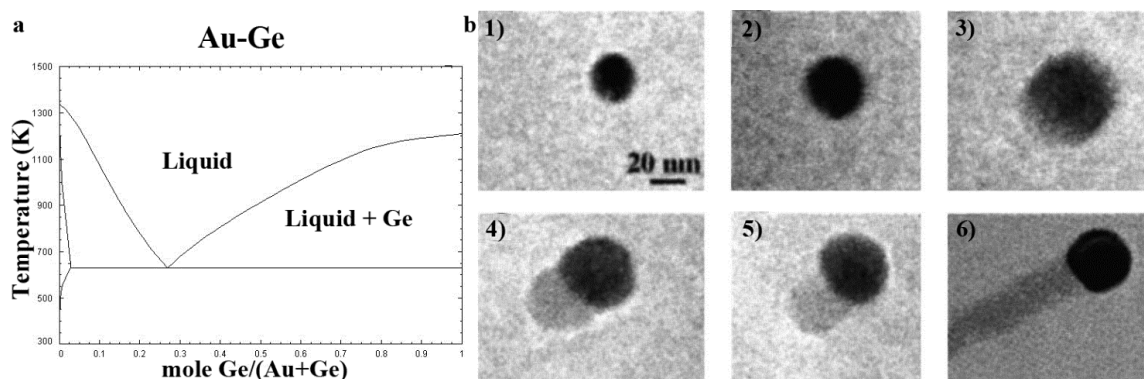
Figure 1.6 a) Binary phase diagram of Ge and Au, b) TEM images of Ge nanorods synthesized with Au catalyst nanoparticles via VLS method (in situ TEM study) [67].

ii) Vapor-Solid (VS) mechanism

Vapor-solid mechanism is another process by which the growth of 1D nanomaterials have been explained. In VS mechanism, no catalyst is used for the synthesis of 1D nanostructures. Figure 1.7 shows as schematic diagram of this process. According to this diagram, the generated vapor from the source material is transported over the substrate and condensed forming 1D nanostructures [49,50]. Sears [69] was the first one who explained the growth of mercury whiskers by axial screw dislocation induced growth in 1955. These whiskers were grown by VS method at -50°C, under high vacuum condition.

Subsequently considerable research has been devoted to studying the growth of nanostructures using this method. To this date, VS growth mechanism has been used to prepare a wide range of nanostructure with different compositions, from metal oxide whiskers with micrometer diameters, nanometer size nanorods to branched hetero-structure nanomaterial.

Reactive species

Stage 1. Diffusion   **Stage 2. Nulcie**   **Stage 3. Nanowire**
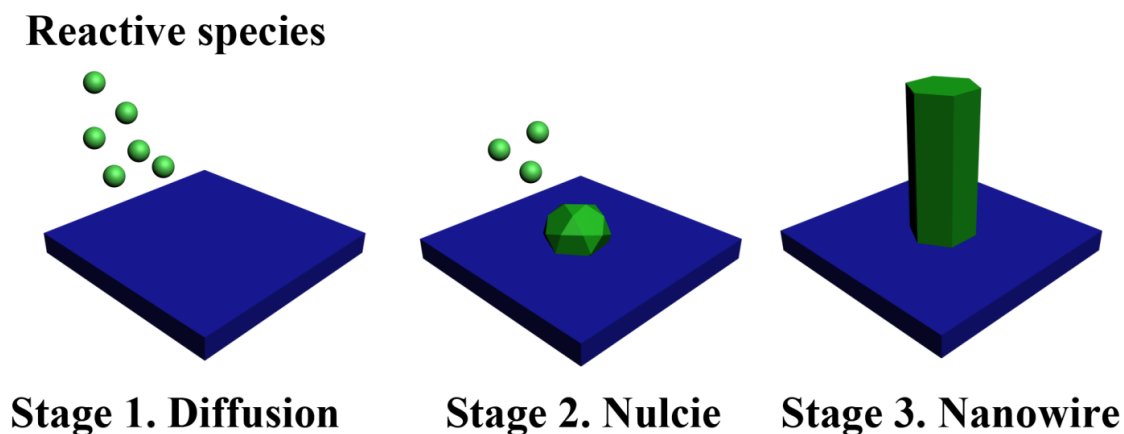
Figure 1.7 Schematic diagram of vapor solid mechanism.

Nanostructures grown following VS mechanism are single crystals with little imperfection. The formation of nanostructures through this method is due to anisotropic growth of the crystal structures. This can be induced by:

1) Different growth rates of the different crystal facets

2) Presence of imperfections in specific crystal directions such as screw dislocation

3) Preferential accumulation, poisoning or passivation by impurities on specific facets

Herein, impurity poisoning and passivation of crystal facets have often been cited as the mechanism resulting in anisotropic growth of nanostructures, especially hetero-structured nanomaterials [58].

1.1.2.2   Synthesis Techniques

Corresponding to various growth mechanisms, some vapor deposition techniques have been developed for the synthesis of 1D nanomaterials. Two most important techniques of the methods are:

i) Physical vapor deposition (PVD)

ii) Chemical vapor deposition (CVD)

i) Physical vapor deposition (PVD)

Physical vapor deposition method is a process often used for growing thin films. In this process the growth species in vapor phase are transferred and deposited on the substrate, without involvement of any chemical reactions. Simple thermal evaporation, laser assisted or sputtering can be used to form the vapor phase. By adjusting the conditions such as use of catalyst particles or templates, 1D and 0D nanostructures have been synthesized using PVD methods.

Previously, nanostructures synthesized using PVD usually were usually confined to low melting point material such as SnO_2 [70] and CdS [71]. However, in recent years with the development of laser assisted processes, sputtering and plasma enhanced vapor deposition systems, a wide range of nanostructured materials has been synthesized using PVD methods [72].

ii) Chemical vapor deposition (CVD)

The advantages of chemical vapor deposition are the possibility of large scale production of nanostructures and often their simple setup. In CVD, the source material is dissociated into various radicals and reactive groups in the gas phase. These species are transported to the substrate and adsorb onto the surface. On the surface they participate in the surface chemical reactions forming nanostructures. CVD processes were originally developed for the deposition of thin films, largely for solid state microelectronics. With the development of various growth mechanisms for 1D nanostructures, CVD processes have become suitable techniques for the controlled synthesis of these nanostructures.

The energy for the dissociation of the source material can be supplied via heating in a thermal CVD process or through plasma in plasma enhanced CVD. Figure 1.8 shows the schematic diagram of these methods. These processes have been used for the synthesis many nanostructures such as Si [73], MnO_2 [74], GaN [75], ZnO [76] and SnO_2 [77].
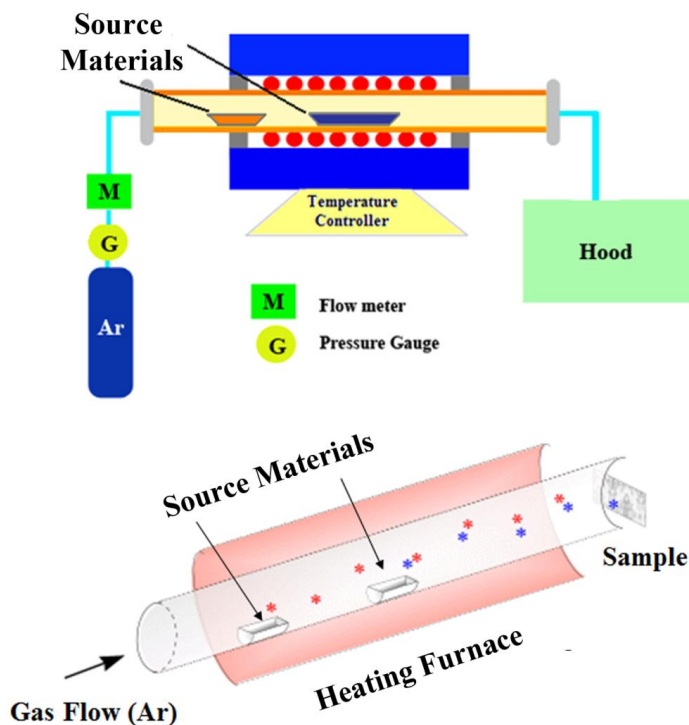
Figure 1.8 Schematic diagram of a CVD process.

1.2   Metal Silicides

Among various materials that have been studied for nanotechnology applications, metal silicides are a family of materials that have attracted considerable attention in recent years. Metal silicides are intermetallic compounds between Si and metals [78]. These compounds have a wide range of properties, making them candidates for variety of applications. Transition metal silicides are a major part of metal silicide materials which

have application mainly in electronic industries. The interest in these silicides is due to their two important properties:

      1) Their electrical resistivity, generally exhibiting a metallic behavior with typical specific resistivity values between 15 to 150 $\mu\Omega$cm at room temperatures

      2) They exhibit good high temperature stability and oxidation resistance.

These properties have encouraged the use of these materials in various applications such as heating elements for electrical furnaces, protective layer for jet engine parts, interconnects in integrated circuits. Furthermore these materials have been proposed as replacement for poly silicon in Si technologies, because of their high temperature stability and electrical conductivity. Metal silicides such as WSi_2 and $TaSi_2$ have been studied for these applications [79]. The silicide materials were mainly deposited as thin films for electronic application through CVD and sputtering processes [80,81]. Metallic silicides such as $TiSi_2$, $NiSi$, $CoSi_2$ have been used as interconnects in nanoscale devices due to their low contact resistance [78]. Furthermore, metal silicides including $CoSi_2$ [82] and Ni_2Si [83] have been studied as field emitters. $FeSi_2$ has also been shown to be a promising material for optoelectronic applications due to its direct band gap, high resistance to oxidation and low vapor pressure [78]. In addition to various applications metal silicides have been as models for fundamental theoretical and experimental studies in condensed matter physics [78].

Metal silicide thin films have been deposited using a variety of methods such as chemical vapor deposition, magnetron sputtering, and thermal annealing.

1.2.1 Application

Nanostructured metal silicides such as nanowires, nanoparticles, nanosheets and nanonets have been synthesized for various applications such as nanoelectronics, energy storage, solar cells and fuel cells. Zhou et al. [84]., have reported the synthesis of Si/$TiSi_2$ heterostructures for Li ion batteries. Their results indicate that these nanostructures have

a high capacity and long cycling life as anode material making them ideal for Li ion batteries. This is due to the high conductivity and structure integrity of $TiSi_2$ nanostructures. $TiSi_2$ nanostructures have also been studied as catalyst support in low temperature fuel cells. Results indicate these nanostructures provide a stable support for Pt catalyst in fuel cell environment [85].

Similar to their bulk counterparts, metal silicides have been extensively studied for applications in nanoelectronics and nanoscale field emitters. Schmitt et al. synthesized CoSi nanowires with diameters of 10 to 150nm and lengths of about 10μm for nanoelectronic applications. The average resistivity of these nanostructures is found to be around 510μΩcm [86]. $NiSi_2$ nanowires with low resistivity have also been shown to be potential candidates for electronic systems. Li-Wei et al. studied the field emission properties of $GdSi_x$ nanowires, indicating a significant improvement in the field emission properties of these nanostructures [87].

Metal silicides have also been studied for other applications such as thermoelectricity. Metal silicides, for decades, have been considered a promising group of materials for thermoelectric applications. Thermoelectirc effect is the direct conversion of temperature differences to electric voltage and vice-versa. Recent research in the material development of such applications is focused on materials with complex crystal structures and nanoscale morphologies [78]. Studies have shown that a phase of $MnSi_{2-x}$ nanowires exhibits excellent thermoelectric performance [88].

1.2.2 Synthesis Methods of Metal Silicides

Many different methods have been developed for the synthesis of metal silicide nanostructures. However, due to the nature of metal silicides and presence of silicon element in their composition, there have been very few reports of synthesis of metal silicides via solution liquid based methods. Most metal silicide nanostructures synthesis

methods involve the vapor deposition silicon and/or metal precursor with low melting point and their reaction and deposition on suitable substrates.

Synthesis methods of silicide nanowires include:

1) Silicidation of silicon nanowires,

2) Reaction of metal sources with silicon substrate, reaction of silicon sources with metal thin film,

3) Simultaneous delivery of silicon and metal sources,

4) Magnetron sputtering.

Using these methods a wide range of metal silicides, especially transition metal silicides have been synthesized.

In silicidation of silicon nanowires, silicon nanowires are synthesized at the first stage. These nanowires are placed in a metal vapor containing environment, transforming into metal silicides via diffusion of metal atoms into the silicon nanowires. Examples of this method are reported in the synthesis of $NiSi_x$ nanowires [89]. There have also been *in situ* TEM studies on the process of silicidation and the diffusion controlled process of synthesizing metal silicide using this method [90].

In the process of synthesizing metal silicide using a reaction of metal precursor with silicon, metal vapor or a low melting point metal precursor such as metal chlorides are used. In this method, the vapor produced from the source material is transported over the silicon substrate and through various growth mechanisms such as VLS and VS, metal silicide nanostructures are synthesized. Synthesis of $TaSi_2$ nanowires has been reported via annealing of silicon substrate with $FeSi_2$ thin film in a Ta rich atmosphere [91]. It was proposed, the Si atoms segregate from the $FeSi_2$ to form Si nanoparticles, in which the Ta atoms diffuse to form $TaSi_2$ nanowires. It is believed that the $FeSi_2$ thin film and nanodots act as catalysts and means for Si nanoparticle formation [78,91,92]. The synthesis of other silicides such as FeSi [93], $TiSi_2$ [94], Ti_5Si_3 [95], CoSi [96], have been reported using the metal halides. In most cases, a VS mechanism has been proposed for

the growth of metal silicide nanowires. For example FeSi nanowires have been synthesized using $FeCl_3$ precursor [93].

Delivery of silicon precursors to metal thin films for the growth of metal silicides has also been well studied. In these studies, SiH_4 and $SiCl_4$, due to their low melting point have been used as silicon precursors. Zhang et al.[97] reported the synthesis of Ti_5Si_3 nanowires via reaction of $SiCl_4$ and Ti thin film and gold nanoparticles as catalyst. They observed a gold alloy droplet on the tip of the nanowires and proposed a VLS mechanism for the synthesis of Ti_5Si_3 nanowires. In addition many phases of nickel silicides such as $NiSi_2$, NiSi and Ni_2Si nanowires have been synthesized using SiH_4 as the silicon precursors [78].

The synthesis of metal silicide nanowires, using simultaneous metal and silicon delivery has recently attracted considerable attention. This is due to the control provided over the concentration of reactive species in the CVD chamber with the aim to control the phase of deposited nanostructures. An example of this process is the use of iodine as the transport agent for the synthesis of metal silicide nanostructures. Researchers have reported the synthesis of Ni_2Si nanowires using Ni_2Si powder as the precursor [78,98]. To synthesize Ni_2Si nanowires, iodine was introduced into the synthesis chamber to move the reactive species from Ni_2Si powder to the substrate. In most cases using iodine ensures the stoichiometry of product to be identical to the source powder.

In addition, single source precursors containing silicon and metal species have been used for the synthesis of various metal silicide nanostructures. FeSi, CoSi, $MnSi_x$ nanostructures are examples of nanostructures synthesized using precursors containing $SiCl_x$ and metal species [78]. Various growth mechanisms have been proposed for the growth of nanostructures using this method, however they mainly depend on the composition of the precursors and experimental conditions.

1.3   Fuel Cells

During the last decade environmental concerns such as global warming, the need to reduce CO_2 emissions and the shortage of energy, have provided the stimulus to seek for alternative clean energy convertors. This has motivated new and expanding interest in fuel cell technology [99]. Fuel cells are innovative energy convertors that convert chemical energy into electricity with the aid of catalysts [100] without involving any moving parts, therefore the process is clean, quiet and highly efficient [101,102].

In fuel cells, often electrochemical reactions take place on two electrodes, the electrochemical oxidation of the fuel, at the other and electrochemical reduction of the oxidant at the cathode. The electrons pass through the external circuit to provide electricity. Fuel cells under favorable circumstances can have efficiencies up to 60% which is 2 to 3 times higher than combustion engines using fossil fuels. This is due to the direct conversion of chemical energy to electricity in fuel cells compared to the indirect approach in combustion engines. Further, fuel cells compared to batteries, which have limited capacity, can produce electricity continuously as long as fuel is provided.

Based on the type of electrolyte used in fuel cells they can be classified into the following groups:

1) Alkaline fuel cells,
2) Phosphoric acid fuel cells,
3) Molten carbonate fuel cells,
4) Solid oxide fuel cells,
5) Proton exchange membrane fuel cells (PEMFCs).

Each of these fuel cells operates in a specific temperature range. Solid oxide and molten carbonate fuel cells are considered high temperature fuel cells due to their operation at temperature above $600^{o}C$. The other three types of fuel cells have operating temperatures below $200^{o}C$. Depending on their start up time and operating temperature these fuel cells

are used in a variety of applications from portable power supply to electric utility and large generation stations.

1.3.1 PEMFCs

Among various types of fuel cell systems, Proton Exchange Membrane Fuel Cells (PEMFCs) have attracted considerable attentions due to their advantages over other fuel cell systems [102]. These fuel cells have a very fast startup and low operating temperature (50-100°C).

A PEMFC single cell consists of two electrodes (anode and cathode) separated by a polymer membrane (often Nafion® based polymers – proton conductors). Figure 1.9 shows a schematic diagram of a PEMFC single cell. At the anode, H$_2$ is fed and on anode catalyst it splits into two proton atoms and two electrons.

$$2H_2 \quad \rightarrow \quad 4H^+ + 4e^-$$

The protons are transported to the cathode side through the polymer membrane and the electrons are conducted through the external circuit. In the cathode side, O$_2$ supplied to the cathode reacts with protons and electrons to form water and heat [103].

$$O_2 + 4H^+ + 4e^- \quad \rightarrow \quad 2H_2O$$
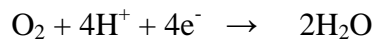
In general, each cell of PMEFC generates around 0.6-0.7 volts [102,103]. To provide suitable voltage for various applications single cells are stacked forming fuel cell stacks [102].

$$O_2 + 2H_2 \quad \rightarrow \quad 2H_2O \qquad E_0=1.229 \text{ V}$$
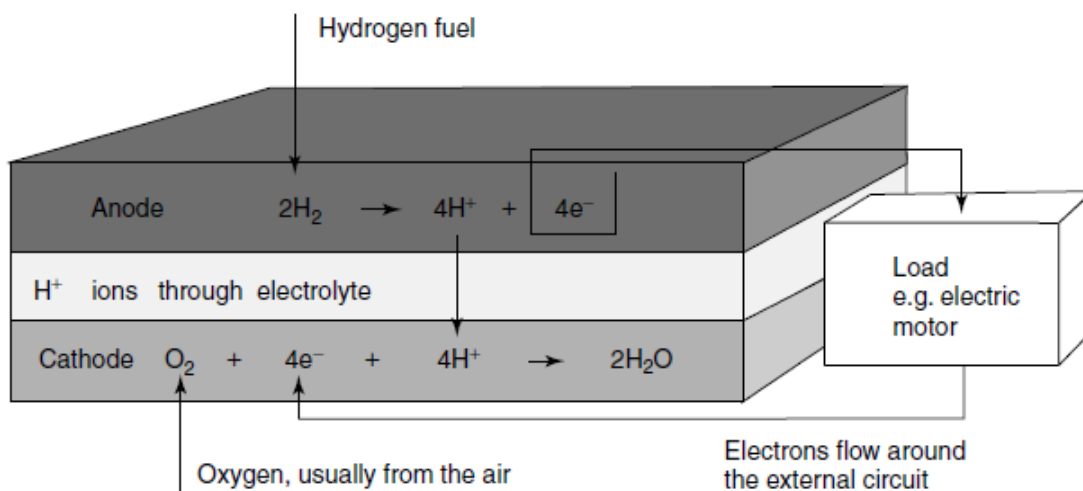
Figure 1.9 Schematic diagram of a PEMFC single cell [99].

One of the most important part of a PEMFCs system is the electrocatalysts, where electrochemical reactions occur. The PEMFC electrocatalyst is generally composed of a catalyst and a catalyst support. Up to now, the most effective electrocatalyst used in both anode and cathode of PEMFCs is platinum (Pt) as catalyst deposited on carbon black particles as catalyst support [101].

1.3.2 Challenges in PEMFCs

High cost and insufficient durability and slow kinetic of reaction are some of the major challenges undermining the commercialization of PEMFCs.

Unfortunately, Pt is considered as one of the most expensive metals in the world and in the past few years the price of Pt has tripled and contributes to over 50% of the total price of PEMFCs [13,104]. In addition Pt catalysts in PEMFCs are readily poisoned by CO and/or other contaminants during the oxidation of fuel. Further, Pt catalyst supported on carbon black, is not stable in the acidic fuel cell environment which will lead to loss of active surface area and reduction of performance and life time of fuel cells.

In order to address these challenges, intensive research has been focused on reducing the Pt content of PEMFCs without compromising the fuel cell performance. This is to meet the cost requirements for fuel cell commercialization. These researches have focused on two areas:

1) Catalyst

2) Catalyst support

Studies on the novel catalyst design have focused on several areas, such as new Pt nanostructures, alloyed and composite catalysts and non-precious catalysts. Studies have shown that Pt nanostructures with different morphologies exhibit different catalytic activity towards oxygen reduction reaction and have different stability and CO tolerance [13].

1.3.3 New Catalyst Supports

Another important area of study in PEMFCs is the development of new catalyst support. Catalyst supports play an important role in PEMFCs. Catalyst support materials are necessary to obtain a high dispersion and a narrow distribution of catalyst nanoparticles which is the prerequisite to obtain a high catalytic performance of catalysts. The support material can also interplay with catalytic metals which influence the catalytic activity. The durability of the catalyst is also greatly dependent on its support.

Generally, the requirements for catalysts support material can be summarized as:

1) High specific surface area , which is necessary for improving the dispersion of catalytic metals

2) Low combustive reactivity under both dry and humid air conditions at low temperatures

3)   High electrochemical stability under fuel cell operating conditions

4)   High electrical conductivity

5)   Easy Pt recovery in used electrocatalysts

In addition, the interaction between the catalytic metals and the support materials should be considered in improving the catalytic activity and durability [99].

Currently- used catalysts (Pt based material) are usually supported on porous conductive materials with a high specific surface area. The most popular support material is Vulcan XC-72 carbon black. While there has been significant achievement on modifying these materials to enhance the performance of fuel cells [105,106], the use of carbon black has several draw backs such as corrosion and instability in fuel cell environment [107,108]. These disadvantages have led researchers to look for novel catalyst supports.

In recent years, novel nanostructured carbon materials such as carbon nanotubes (CNTs) [64], carbon fibers [109] and mesoporous carbons [110] have been receiving attention as catalyst supports for PEMFCs because of their unique structure and properties. Studies have shown that CNTs have overwhelming advantages compared to conventional carbon black in PEMFC electrocatalyst supports. These nanostructures provide high electrical conductivity due to their unique structure and electrical properties and due to fewer defects. Therefore, it has been reported that they are more stable catalyst supports in fuel cell conditions [64,109,111]. Furthermore, the 1D nanostructure of CNTs enables the construction of an ordered catalyst layer in PEMFCs which provides benefits for mass/electron transport resulting in higher cell performance [109].

Other than nanostructured carbon material, many conductive or semi-conductive ceramic nanostructures have attracted attention as catalyst support materials or as secondary supports to modify and promote the catalyst supports for PEMFCs, including TiO_x [112], SnO_2 [113] and WO_x [52]. These metal oxides have shown promising effects on the catalytic activity and durability of PEMFC catalysts. For example, it has been shown that

Pt catalyst supported on SnO_2 can show higher electrocatalytic activities which are attributed to the enhanced properties achieved by combining Pt nanoparticles with SnO_2 [113].

Even though these materials exhibit promising performance as support for fuel cell catalysts, ceramic catalyst supports have several problems, including synthesis process of nanostructured ceramics and their electronic conductivity.

Since the use of only carbon or ceramic materials as catalyst supports is not satisfactory in some cases, composite catalyst supports have been recently proposed as fuel cell catalyst supports [60]. For example studies have shown that the performance of PEMFCs can be significantly enhanced using composite nanostructures such as CNT-SnO2 [114] nanostructures as catalyst support.

1.4   Objectives and Motivations

PEMFCs are innovative clean energy technologies with high efficiency which provide clean energy. However, the high cost and low durability and slow kinetics of reaction in PEMFCs are major challenges in the road to their commercialization. Nanostructured electrocatalysts are one of promising solutions to address these challenges.

To this date, there have been many reports on using nanostructured material as catalysts and catalysts support in PEMFCs. However, many areas still remain to be fully explored. In addition, the mechanisms responsible for enhancing the performance of fuel cell by these nanostructures have to be studied. This can be achieved to some extent by studying the interaction between the catalyst nanoparticles and catalyst supports and electrochemical characterization of electrocatalyst systems. Once these areas are fully explored, it will become possible to design the next generation of electrocatalysts for a broad range of technological important applications.

The objectives of thesis are to develop various novel nanostructures as catalyst supports for PEMFCs such as 1D networked nanowires, composite nanostructures and core/shell structures (nanocables). The studies were mainly focused on the synthesis and characterization of novel 1D networked transition metal silicide nanostructures, carbon nanotube based composite nanostructures of $TiSiO_x$ and TiO_2 and $W_{18}O_{49}$ nanowires and WS_2-$W_{18}O_{49}$ nanocables. The electrochemical properties of these nanostructures were studied under PEMFC conditions. The electronic structure of Pt catalysts on some of these supports was studied to understand the change in their electrochemical properties. The as-synthesized catalysts supports were expected to improve the performance of PEMFCs.

1.5   Thesis Outline

This thesis consists of eight chapters (two introductory chapters and five manuscripts and one final chapter) and fulfills the requirements on "Integrated-Article" form as outlines in the *Thesis Regulation Guide* of the school of graduate and postdoctoral studies (SGPS) of the University of Western Ontario. The thesis chapters are arranged as follows.

Chapter 1 is an introduction to three different fields of study related to this thesis. It gives an overview on nanomaterials, their properties, application and their synthesis methods, it describes some of the growth mechanisms involved in the synthesis of nanomaterials. In the following section, the focus is on metal silicides and the synthesis of nanostructured metal silicides, followed by an introduction to fuel cells, especially proton exchange membrane fuel cells (PEMFCs). In this section the working and structure of a single cell fuel cell is described as well as challenges of the catalyst electrodes and the solution offered by application of nanomaterials. At the end, the research objectives and thesis organization of this study are clearly stated.

Chapter 2 describes several experimental processes and analytical techniques, used in the synthesis and characterization of nanostructured samples in the following chapters.

The principal results of this thesis are presented in chapters 3-7.

Chapter 3 (Spatial Sequential Growth of Various WSi_2 Networked Nanostructures and Mechanisms) describes the synthesis of novel transition metal silicide nanostructures such as WSi_2 networked nanosheets and nanowires. WSi_2 networked nanostructures were synthesized using a low pressure chemical vapor deposition method. Experimental results indicated, the synthesis process and the morphology of these nanostructures are governed by vapor solid mechanism and depend on the concentration of reactive species in the CVD chamber. These nanostructures provide a high surface area with good corrosion and oxidation resistant properties, making the potential candidates for PEMFC catalyst supports.

Chapter 4 (Tailoring Growth of Single Crystalline Complex Ta_5Si_3 Nanostructures: From Networked Nanowires to Nanosheets) describes the synthesis of another novel metal silicide nanostructure Ta_5Si_3 networked nanoribbons and nanosheets. These nanostructures are synthesized using a low pressure chemical vapor deposition method. Results indicate the vapor pressure of $TaCl_x$ and SiO_x plays an important role in determining the morphology of Ta_5Si_3 nanostructures.

Chapter 5 ($TiSi_2O_x$ coated N-doped Carbon Nanotubes for the Oxygen Reduction Reaction in Proton Exchange Membrane Fuel Cells) describes the synthesis of composite nanostructures as alternative catalyst supports for PEMFCs. These nanostructures were prepared using a combination of chemical vapor deposition and magnetron sputtering. Pt nanoparticles were deposited on the composite nanostructures using wet chemical reduction method. Electrochemical properties such as oxygen reduction reaction of $Pt/TiSi_2O_x$-NCNTs were compared to Pt/NCNTs and commercial Pt/C electrocatalysts. Results indicated composite nanostructures to be promising catalyst supports for PEMFC applications.

Chapter 6 (TiO_2 Nanoparticle Decorated Nitrogen Doped Carbon Nanotubes as Pt Catalyst Support for Low Temperature Fuel Cells) reports another composite nanostructure as alternative catalyst support for PEMFCs. Pt nanoparticles were deposited on TiO_2-NCNTs using a wet chemical reduction method. The electrochemical

properties of these electrocatalysts such as oxygen reduction reaction, methanol oxidation and CO tolerance indicate that TiO_2-NCNTs are promising catalyst supports for PEMFCs.

Chapter 7 (One-step tunable synthesis of pristine, sulfur-doped $W_{18}O_{49}$ nanowires and $WS_2/W_{18}O_{49}$ nanocables) describes the controlled synthesis of $W_{18}O_{49}$ nanowires directly on tungsten powder by sulfur doping of these nanowires. Results indicated sulfur diffusion into the surface layers of $W_{18}O_{49}$ nanowires, changes the surface chemistry of the nanowires, reducing their diameters. Further increase in the sulfur flow rate in the synthesis chamber resulted in the one step synthesis of long $WS_2/W_{18}O_{49}$ nanocables. Detailed experimental results show this process to be diffusion dependent. Similar concept can be used for controlled synthesis of nanostructures for PEMFCs applications.

Chapter 8 summarizes the results and contributions of the thesis work. In addition, the authors present some suggestion for future work.

1.6   References

[1]   Bogue R 2009 Sensor Review 29 310–315

[2]   Gibson RF 2010 Composite Structures 92 2793–2810

[3]   Nanoscience and nanotechnologies: opportunities and uncertainties, The Royal Society, 2004

[4]   Jr CPP and Owens FJ 2003 Introduction to Nanotechnology John Wiley & Sons

[5]   Schmid G and Corain B 2003 European Journal of Inorganic Chemistry 17 3081-3098

[6]   Espinosa HD, Bernal RA and Minary-Jolandan M 2012 Advanced Materials 24 4656–4675

[7]   Agrawal R, Peng B and Espinosa HD 2009 Nano Letters 9 4177–4183

[8]   Beck IE, Bukhtiyarov VI, Pakharukov IY, Zaikovsky VI, Kriventsov VV and Parmon VN 2009 Journal of Catalysis 268 60–67

[9]   Cuenya BR 2010 Thin Solid Films 518 3127–3150

[10]   Schwartz V, Mullins DR, Yan W, Chen B, Dai S and Overbury SH 2004 Journal of Physical Chemistry B 108 15782–15790

[11]   Ligthart DAJM, Van Santen RA and Hensen EJM 2011 Journal of Catalysis 280 206–220

[12]   Mostafa S, Behafarid F, Croy JR, Ono LK, Li L, Yang JC, Frenkel AI and Cuenya BR 2010 Journal of American Chemical Society 132 15714–15719

[13]   Mazumder V, Lee Y and Sun S 2010 Advanced Functional Materials 20 1224–1231

[14]   Kennedy LC, Bickford LR, Lewinski NA, Coughlin AJ, Ying Hu, Day ES, West JL and Drezek RA 2011 Small 7 169–83

[15]   Yuanyuang Li, Schluesener HJ and Shunqing Xu 2010 Gold Bulletin 43 29–41

[16]   Matheu P, Lim SH, Derkacs D, McPheeters C and Yu ET 2008 Applied Physics Letters 93 113108-113111

[17]   Baker WS, Pietron JJ, Teliska ME, Bouwman PJ, Ramaker DE and Swider-Lyons KE 2006 Journal of the Electrochemical Society 153 1702–1707

[18]   Gyenge E, Atwan M and Northwood D 2006 Journal of the Electrochemical Society 153 150–158

[19]   Zengcai Liu, Shirlaine Koh, Chengfei Yu and Strasser P 2007 Journal of the Electrochemical Society 154 1192–1199

[20]   Tsai C-W, Chen HM, Liu R-S, Asakura K, Zhang L, Zhang J, Lo M-Y and Peng Y-M 2011 Electrochimica Acta 56 8734–8738

[21]   Chen G, Li Y, Wang D, Zheng L, You G, Zhong C-J, Yang L, Cai F, Cai J, Chen B H, 2011 Journal of Power Sources 196 8323–8330

[22]   Sudeep PK and Emrick T 2007 Polymer Reviews 47 3–11

[23]   Senthilkumar K, Senthilkumar O, Yamauchi K, Sato M, Morito S, Ohba T, Nakamura M and Fujita Y 2009 Physica Status Solidi B 246 885–888

[24]   Urbina MC, Zinoveva S, Miller T, Sabliov CM, Monroe WT and Kumar CSSR 2008 Journal of Physical Chemistry C 112 11102–11108

[25]   Chan Kyu Kim, Kalluru RR, Singh JP, Fortner A, Griffin J, Darbha GK and Ray PC 2006 Nanotechnology 17 3085–3093

[26]   Shipway AN, Katz E and Willner I 2000 Angewandte Chemie 39 19–52

[27]   Hu J, Odom TW and Lieber CM 1999 Accounts of Chemical Research **32** 435–445

[28]   Iijima S 1991Letters to Nature 56–58

[29]   Bar-Sadan M, Kaplan-Ashiri I and Tenne R 2007 European Physical Journal Special Topics 149 71–101

[30]   Zettl A 1996 Advanced Materials 8 443–445

[31]   Guozhen Shen, Bando Y and Golberg D 2007 International Journal of Nanotechnology 4 730–749

[32]   Kreizman R, Enyashin AN, Deepak FL, Albu-Yaron A, Popovitz-Biro R, Seifert G and Tenne R 2010 Advanced Functional Materials 20 2459–2468

[33]   Heinze S, Radosavljevic M, Tersoff J and Avouris P 2003 Physical Review B 68 235418–23551

[34]   Polizu S, Savadogo O, Poulin P and Yahia L 2006 Journal of Nanoscience and Nanotechnology 6 1883–1904

[35]   Bandaru PR 2007 Journal of Nanoscience and Nanotechnology 7 1239–1267

[36]   Maarouf AA, Kane CL and Mele EJ 2000 Physical Review B 61 11156–11165

[37]   Sui X-M, Giordani S, Prato M and Wagner HD 2009 Applied Physics Letters 95-98

[38]   Wiggins-Camacho JD and Stevenson KJ 2009 Journal of Physical Chemistry C 113 19082–19090

[39]   Dai L, Patil A and Vaia R 2005 Synthetic Metals 154 229–232

[40]   Venkateswara Rao C and Ishikawa Y 2012 Journal of Physical Chemistry C 116 4340–4346

[41]   Chen J, Wang JZ, Minett AI, Liu Y, Lynam C, Liu H and Wallace GG 2009 Energy and Environmental Science 2 393–396

[42]   Lafuente E et al. 2006 Journal of Materials Research 21 2841–2846

[43]   Prosini PP, Pozio A, Botti S and Ciardi R 2003 Scientific Advances in Fuel Cell Systems 265–269

[44]   Hal-Shun Wu, Jian-Feng Jia and Haijun Jiao 2006 Physica B 381 90–195

[45]   Rapoport L, Bilik Y, Feldman Y, Homyonfer M, Cohen SR and Tenne R 1997 Nature 387 791–793

[46]   Li Y-H, Zhao YM, Ma RZ, Zhu YQ, Fisher N, Jin YZ and Zhang XP 2006 Journal of Physical Chemistry B 110 18191–18195

[47]   Liu HK, Wang GX, Guo ZP, Wang JZ and Konstantinov K 2007 Journal of New Materials for Electrochemical Systems 10 101–104

[48]   Grimes CA, Mor GK, Varghese OK, Paulose M and Shankar K 2006 Solar Energy Materials and Solar Cells 90 2011–2075

[49]   Wang N, Cai Y and Zhang RQ 2008 Materials Science and Engineering: R: Reports 60 1–51

[50]   Rao CN., Deepak F., Gundiah G and Govindaraj A January Progress in Solid State Chemistry 31 5–147

[51]   Lu W 2006 Journal of Physics D: Applied Physics 39 387–406

[52]   Saha MS, Banis MN, Zhang Y, Li R, Sun X, Cai M and Wagner FT 2009 Journal of Power Sources 192 330–335

[53]   Wang J, Du N, Zhang H, Yu J and Yang D 2011 Journal of Physical Chemistry C 115 11302–11305

[54]   Chinnamuthu P, Dhar JC, Mondal A, Bhattacharyya A and Singh NK 2012 Journal of Physics D: Applied Physics 45 135102-135107

[55]   Antolini E and Gonzalez ER 2009 Solid State Ionics, Diffusion & Reactions 180 746–763

[56]   Sun S, Zhang G, Geng D, Chen Y, Banis MN, Li R, Cai M and Sun X 2010 Chemistry - A European Journal 16 829–835

[57]   Sun S, Jaouen F and Dodelet J 2008 Advanced Materials 20 3900–3904

[58]   Junqing Hu, Bando Y and Golberg D 2009 Journal of Materials Chemistry 19 330–343

[59]   Liu X, Lin Y, Zhou S, Sheehan S and Wang D 2010 Energies 3 285–300

[60]   Zhang Y, Li R, Zhou X, Cai M and Sun X 2008 Journal of Physical Chemistry C 112 10038–10042

[61]   Zhang Y, Li R, Zhou X, Cai M and Sun X 2008 Journal of Nanomaterials 2008 1–8

[62]   Wang Y et al. 2008 Advanced Functional Materials 18 1131–1137

[63]   Osada M and Sasaki T 2009 Journal of Materials Chemistry 19 2503–2511

[64]   Saha MS, Li R, Sun X and Ye S 2009 Electrochemistry Communications 11 438–441

[65]   Andreas HA, Kung SKY, McLeod EJ, Young JL and Birss VI 2007 Journal of Physical Chemistry C 111 13321–13330

[66]   Yang D-Q, Sun S, Dodelet J-P and Sacher E 2008 Journal of Physical Chemistry C 112 11717–11721

[67]   Harada M and Einaga H 2007 Journal of Colloid and Interface Science 308 568–572

[68]   Wu Y and Yang P 2001 J. Am. Chem. Soc. 123 3165–3166

[69]   Sears GW 1960 The Journal of Chemical Physics 33 563–567

[70]   Papargyri S, Tsipas DN, Papargyris DA, Botis AI and Papargyris AD 2005 Solid State Phenomena 106 57–62

[71]   Lin Y-F, Song J, Ding Y, Lu S-Y and Wang ZL 2008 Applied Physics Letters 92 022105 –022108

[72]   Zhao XW and Yang FY 2008 Journal of Vacuum Science and Technology B: Microelectronics and Nanometer Structures 26 675–677

[73]   Cham-Sol Choi and Jong-Hwan Yoon 2012 Applied Physics A: Materials Science & Processing 108 509–513

[74]   Banis MN, Zhang Y, Banis HN, Li R, Sun X, Jiang X and Nikanpour D 2011 Chemical Physics Letters 501 470–474

[75]   Cai XM, Djurisic AB and Xie MH 2006 Thin Solid Films 515 984–989

[76]   Huang H, Yang S, Gong J, Liu H, Duan J, Zhao X, Zhang R, Liu Y and Liu Y 2005 Journal of Physical Chemistry B 109 20746–20750

[77]   Kim D, Kim Y-K, Park SC, Ha JS, Huh J, Na J and Kim G-T 2009 Applied Physics Letters 95 043107–043111

[78]   Schmitt AL, Higgins JM, Szczech JR and Jin S 2010 Journal of Material Chemistry 20 223-235

[79]   Reader AH, van Ommen AH, Weijs PJW, Wolters RAM and Oostra DJ 1993 Reports on Progress in Physics 56 1397–1467

[80]   Yckache K, Boivin P, Baiget F, Radjaa S, Auriel G, Sagnes B, Oualid J and Glachant A 1998 Microelectronics Reliability 38 937–942

[81]   Doscher M, Pauli M and Muller J 1994 Thin Solid Films 239 251–258

[82]   Han BW, Lee JS and Ahn BT 2002 IEEE Electron Device Letters 23 10–12

[83]   Liu Z, Zhang H, Wang L and Yang D 2008 Nanotechnology 19 375602-375606

[84]   Zhou S, Liu X and Wang D 2010 Nano Letters 10 860–863

[85]   Jingjie Wu, Fengjie Xia, Mu Pan and Xiao-Dong Zhou 2012 Journal of the Electrochemical Society 159 654–660

[86]   Schmitt AL, Zhu L, Schmeisser D, Himpsel FJ and Jin S 2006 Journal of Physical Chemistry B 110 18142–18146

[87]   Li-Wei Chu, Shih-Wei Hung, Chiu Yen Wang, Yi-Hsin Chen, Jianshi Tang, Wang KL and Lih-Juann Chen 2011 Journal of the Electrochemical Society 158 64–68

[88]   Higgins JM, Schmitt AL, Guzei IA and Jin S 2008 Journal of the American Chemical Society 130 16086–16094

[89]   Wu Y, Xiang J, Yang C, Lu W and Lieber CM 2004 Nature 430 61-65

[90]   Liang Y-H, Yu S-Y, Hsin C-L, Huang C-W and Wu W-W 2011 Journal of Applied Physics 110 074302-074306

[91]   Chueh YL, Chou LJ, Cheng SL, Chen LJ, Tsai CJ, Hsu CM and Kung SC 2005 Applied Physics Letters 87 223113–223121

[92]   Chueh Y-L, Ko M-T, Chou L-J, Chen L-J, Wu C-S and Chen C-D 2006 Nano Letters 6 1637–1644

[93]   Liang S, Fang X, Xia T-L, Qing Y and Guo Z-X 2010 Journal of Physical Chemistry C 114 16187–16190

[94]   Che-Ming Chang, Yu-Cheng Chang, Yao-An Chung, Chung-Yang Lee and Lih-Juann Chen 2009 Journal of Physical Chemistry C 113 17720–17723

[95]   Huang-Kai Lin, Yu-Fen Tzeng, Chia-Hsin Wang, Nyan-Hwa Tai, I-Nan Lin, Chi-Young Lee and Hsin-Tien Chiu 2008 Chemistry of Materials 20 2429–2431

[96]   Kwanyong Seo, Varadwaj KSK, Mohanty P, Sunghun Lee, Younghun Jo, Myung-Hwa Jung, Jinhee Kim and Bongsoo Kim 2007 Nano Letters 7 1240–1245

[97]   Zhang Y, Geng D, Liu H, Banis MN, Ionescu MI, Li R, Cai M and Sun X 2011 Journal of Physical Chemistry C 115 15885–15889

[98]   Song Y, Schmitt AL and Jin S 2007 Nano Lett. 7 965–969

[99]   Larminie J and Dicks A 2003 Fuel Cell Systems Explained Wiley

[100]   O'Hayre R, Cha S-W, Colella W and Prinz FB 2009 Fuel Cell Fundamentals John Wiley & Sons

[101]   Barbir F 2012 Pem Fuel Cells: Theory and Practice Academic Press

[102]   Srinivasan S 2006 Fuel Cells: From Fundamentals to Applications Springer

[103]   Borup R et al. 2007 Chemical Reviews 107 3904–3951

[104]   Bing Y, Liu H, Zhang L, Ghosh D and Zhang J 2010 Chemical Society Reviews 39 2184–2202

[105]   Heung Yong Ha, Chan Hee Park, Scibioh MA, Hyoung-Juhn Kim, In-Hwan Oh and Seong-Ahn Hong 2006 Journal of Power Sources 162 1023–1028

[106]   Schiraldi DA, Guha A, Weijie Lu and Zawodzinski TA 2007 Carbon 45 1506–1517

[107]   Hoogers G 2013 Fuel Cell Technology Handbook, Second Edition 2nd ed. CRC Press

[108]   Roen LM, Paik CH and Jarvi TD 2004 Electrochemical and Solid-State Letters 7 19–22

[109]   Shao Y, Liu J, Wang Y and Lin Y 2009 Journal of Material Chemistry 19 46–59

[110]   Sahu AK, Sridhar P and Pitchumani S 2009 Journal of the Indian Institute of Science 89 437–445

[111]   Chen Y, Wang J, Liu H, Li R, Sun X, Ye S and Knights S 2009 Electrochemistry Communications 11 2071–2076

[112]   Park K-W, Lee Y-W, Oh J-K, Kim D-Y, Han S-B, Ko A-R, Kim S-J and Kim H-S 2011 Journal of Industrial and Engineering Chemistry 17 696–699

[113]   Saha MS, Li R, Cai M and Sun X 2007Electrochemical Solid State Letters 10 130–133

[114]   Dao-Jun Guo and Jin-Mao You 2012 Journal of Power Sources 198 127–131

Chapter 2

2   Experimental and Characterization Methods

2.1   Synthesis Process

2.1.1 Metal Oxides

The synthesis of pristine and sulfur doped $W_{18}O_{49}$ nanowires and $WS_2/W_{18}O_{49}$ nanocables were carried out using a chemical vapor deposition method. There have been reports of synthesis of $W_{18}O_{49}$ nanowires using similar method [1,2]. In this method, tungsten powder (99% Aldrich) was used as the source and substrate and high purity Ar as the carrier gas. In contrast to previous studies [3,4], sulfur powder was added to the system for the synthesis of sulfur doped $W_{18}O_{49}$ nanowires and $WS_2/W_{18}O_{49}$ nanocables. Figure 2.1, shows a schematic diagram of the CVD setup used for the synthesis of tungsten based nanostructures.
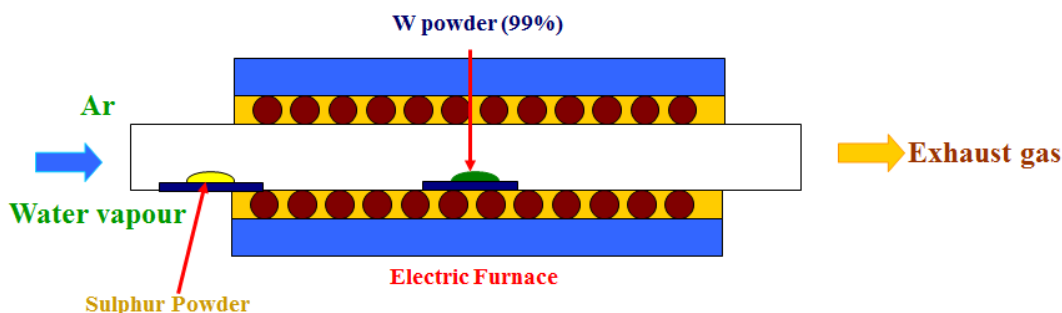
Figure 2.1 Schematic diagram of CVD setup for the synthesis of $W_{18}O_{49}$ nanowires and $WS_2/W_{18}O_{49}$ nanocables.

To synthesize tungsten oxide nanostructures, tungsten powder was placed in the middle of a quartz tube and mounted on horizontal electric furnace. Sulfur powder was positioned in the upstream region of the furnace. Prior to heating the furnace, the CVD chamber was saturated with water vapor via introduction of Ar gas, passed through a

heated water bubbler, into the CVD chamber for 30 min at a flow rate of 300sccm (standard cubic centimeters per minute). The system was heated to a set temperature and kept at this temperature for 60 min at a constant flow rate of water vapor saturated Ar. At the end of the experiment, the system was cooled down to room temperature slowly. In these experiments, the effect of various growth parameters such as temperature, time and sulfur vapor concentration in CVD chamber on the morphology of nanostructures synthesized were studied. The growth parameters used in this thesis were optimized for the high density synthesis of nanostructured material, through a series detailed experiments.

2.1.2 Metal Silicides

Metal silicide nanostructures (WSi_2, W_5Si_3 and Ta_5Si_3) were synthesized using a low pressure CVD method, shown in Figure 2.2. In this process metal chlorides (WCl_6 or $TaCl_5$) were used as low melting point metal sources and silicon powder was used as the silicon source. The nanostructures were synthesized on a conductive substrate for fuel cell application, such as carbon paper (E-TEK, De Nora North America, Somerset, NJ). As shown in Figure 2.2, the metal chloride was placed in the upstream region (low temperature zone) of a quartz tube, and the substrate was positioned over the silicon powder in the middle of the tube. The tube was mounted on an electric furnace and attached to a homemade, vacuum system. To purge oxygen from the system, the pressure in the CVD chamber was decreased to 100 Pa, and argon was flushed into the system increasing the pressure to over 5 kPa. This procedure was repeated several times. In the next stage, the system was heated to a set temperature with a controlled heating rate and kept at this temperature for fixed duration. During the experiment the pressure inside the chamber was maintained at 500 Pa with a constant flow of Ar gas which acted as a carrier gas. After the experiment the chamber was cooled down to room temperature slowly at 500 Pa.
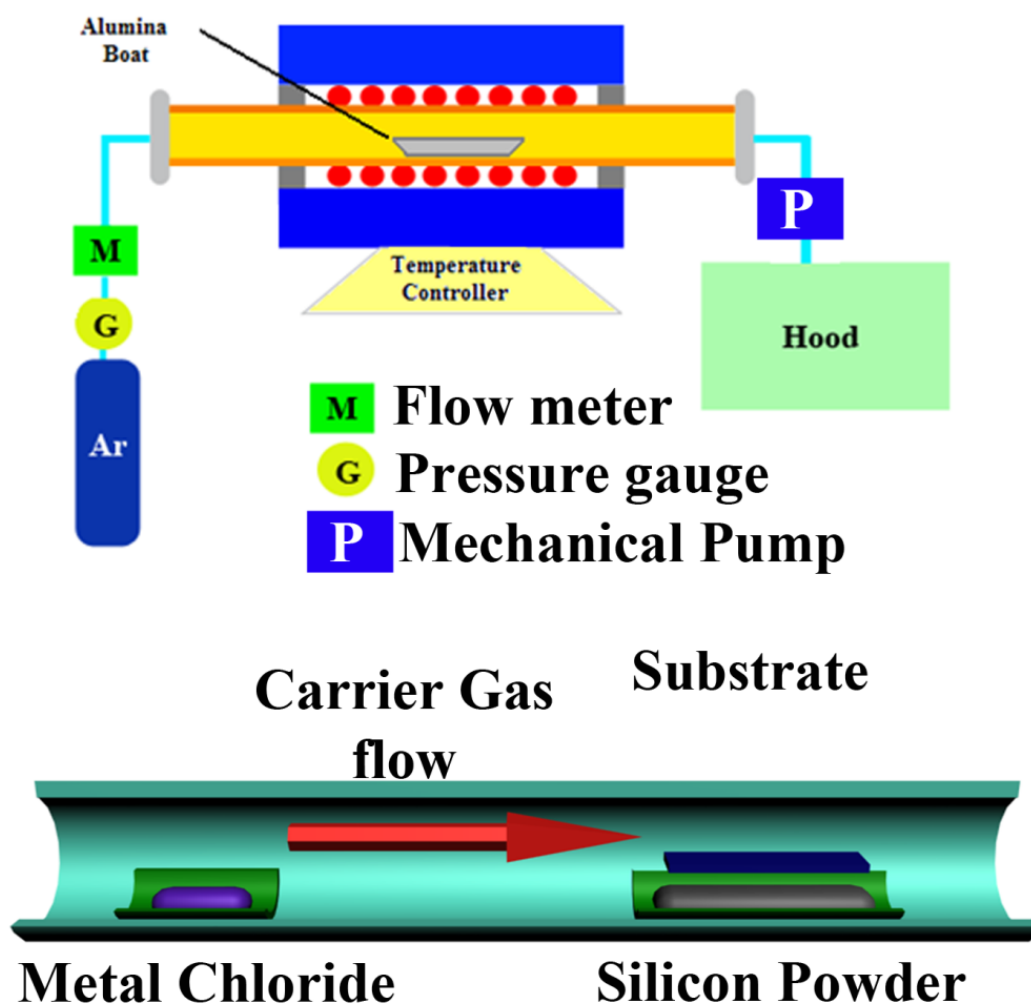
Figure 2.2 Schematic diagram of low pressure CVD process of metal silicide synthesis.

2.1.3 Composite Nanostructures

Composite nanostructures of $TiSi_2O_x$-NCNTs and TiO_2-NCNTs were synthesized using a combination of CVD, magnetron sputtering and solution based methods. Nitrogen doped carbon nanotubes as reported previously [5] were synthesized using a CVD with melamine ($C_3H_6N_6$) as the carbon and nitrogen source and Fe as the catalyst at 800^oC. In

this process, carbon paper with a pre-sputtered aluminum buffer layer (30 nm) was used as the substrate.

In the next stage, the NCNTs were placed in a modified plasma enhanced CVD (PECVD)/sputtering system, 10 cm from a $TiSi_2$ sputtering target (2 inch in diameter) as shown in Figure 2.3. The pressure of the system was decreased to 2.5×10^{-3} Pa to purge oxygen from the sputtering chamber. Ar gas was introduced into the system with a flow rate of 15 sccm to maintain a 2×10^{-1} Pa working pressure in the chamber. A 100nm layer $TiSi_2O_x$ layer was deposited on the NCNTs using a RF magnetron.

Figure 2.3 A photo of the modified PECVD/Sputtering system used for $TiSiO_x$ coating of NCNTs.

To synthesize TiO$_2$-NCNTs composite nanostructures, the sputtered TiSi$_2$O$_x$-NCNTs, were annealed at 1000°C, for 6 hrs under a constant flow of Ar at 500 Pa. After heat treatment, the samples were submersed in a NaOH solution (10wt%) for 48 hrs. The resulting nanostructures were washed with deionized water and dried at room temperature overnight.

2.1.4 Pt Nanoparticles

The synthesis of Pt nanoparticles, followed a previously reported procedure via reduction of Pt precursor with formic acid at 80°C under atmospheric pressure [6,7]. In this method, 1mL of 0.03M Pt precursor (H$_2$PtCl$_6$.6H$_2$O, Aldrich, 99.95%) and 1mL of formic acid (HCOOH, Aldrich, 98%) were mixed with 20mL of water at room temperature. The samples were immersed in the solution and the solution was placed in a water bath with a temperature of 80°C for 15min. The solution turned from golden color to dark brown color during the reaction, indicating the synthesis of Pt nanoparticles in the solution. After the experiment the solution was cooled down to room temperature. The samples were washed with deionized water and dried at room temperature overnight.

2.2   Characterization Technique

The physical and chemical properties of the samples synthesized in this thesis were characterized with a variety of analytical methods.

2.2.1 Scanning Electron Microscopy

Scanning electron microscope (SEM) shown in Figure 2.4, is part of electron microscope family, which can provide information of the surface topography and composition of a sample. SEM uses a focused high energy beam of electrons which interact with atoms on the sample producing secondary electrons, back scattered electrons and characteristic x-rays of sample atoms. The produced electrons and characteristic x-ray can be detected using various detectors providing information about the surface region of the sample. Secondary and back scattered electrons can provide high resolution images of the sample surface, making SEM one of the most widely used instruments in surface science studies.

Based on the detection of characteristic x-ray originating from the interaction of focused beam electrons with the atoms of the sample, energy dispersive x-ray spectroscopy (EDS) is developed. This analytical method is used for elemental analysis of the surface of the sample. Generally this technique is in conjunction with either SEM or TEM.

In this thesis, the samples were examined by SEM (Hitachi S-4800) operated at 5kV.

Figure 2.4 A photo of SEM (Hitachi, S-4800) machine.

2.2.2 Transmission Electron Microscopy

Transmission electron microscopes (TEM) shown in Figure 2.5 are another family of electron microscopes which provide information on thin samples via interaction of focused high energy electron beam with the sample atoms. TEM can arguably be the most efficient and versatile tools for characterization of material over spatial ranges from atomic scale through to nanoscale (from <1nm to ~ 100nm). These instruments, in

addition to high resolution atomic scale images can provide detailed information on the crystal structure and chemical state of atoms in the specimen. However TEM analysis has some limitation such as the thickness of the specimen. In these microscopes, the specimen needs to be very thin to allow the incoming electrons to pass through the sample after their interaction with the sample. Z – contrast imaging of samples containing heavy atoms such as Pt and Ti were carried out using High angle annular dark field (HAADF) technique in TEM.

Figure 2.5 A photo of TEM (Philips CM10) machine.

2.2.3 X-ray Diffraction

X-ray diffraction (XRD) methods are a family of physical characterization methods that provide information on the crystal structure, chemical composition and physical properties of material. In this thesis the XRD pattern was recorded on a Bruker D8 advance diffractometer with Co and Cu Kα radiation sources (Figure 2.6).

Figure 2.6 A photo of Bruker D8, advance XRD machine.

2.2.4 X-ray Absorption Fine Structure

X-ray absorption fine structures (XAFS), is a widely used method in various fields including catalysts research and material science. XAFS describes a method in which core level electrons are excited to unoccupied levels or to the continuum via absorption of x-rays. This method often requires a synchrotron radiation source which can provide high intensity and focused X-ray beam with tunable energies. XAFS spectra are especially sensitive to the formal oxidation state, coordination chemistry and the distances, coordination number and species of the atoms immediately surrounding the selected element.

2.3   Electrochemical Characterization

The electrochemical characterizations of samples were conducted in a standard three-compartment electrochemical cell using an Autolab potentiostat/galvanostat (Model, PGSTAT-30, Ecochime, Brinkman Instruments) as shown in Figure 2.7. A Pt wire was used as the counter electrode and a Ag/AgCl (3M NaCl) or saturated calomel electrode (SCE) was used as the reference electrode. Samples for electrochemical characterization were all prepared on carbon paper. The working electrode was attached to the carbon paper via gold foils for better conductivity.
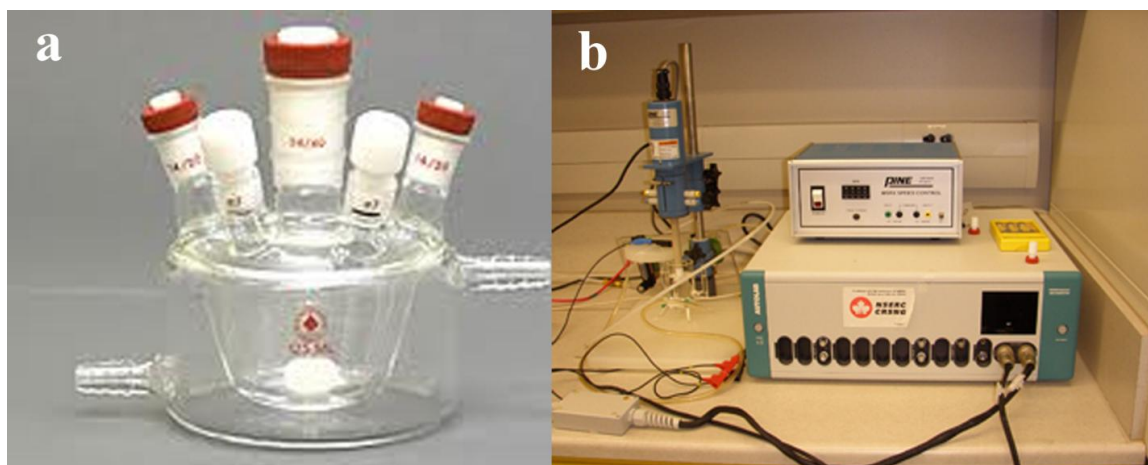
Figure 2.7 A photo of a) Three compartment electrochemical cell, b) Autolab potentiostat/galvanostat (Model, PGSTAT-30, Ecochime, Brinkman Instruments).

2.3.1 Cyclic Voltammetry

The cyclic voltammetry (CV) measurements of each sample was conducted by cycling between 0.05 and 1.2V (vs RHE) with a sweep rate of 50 mVs^{-1} in a nitrogen saturated 0.5M H_2SO_4 solution. The samples were first immersed in the solution, while connected to the working electrode. Nitrogen gas was introduced into the solution for 30 min to saturate the solution. In the next stage each sample was cycled for at least 50 times.

Each sample was tested at least three times under the same conditions. The electrochemical surface area (ESCA) was calculated by measuring the charge associated with H_{ads} (Q_H) and Q_{ref} according to the following equation:

$$A_{EL}=Q_H/(Q_{ref} \text{ x Pt loading})$$

The AEL is expressed in cm^2mg^{-1} where the Pt loading is in $mgptcm^{-2}$. Q_{ref} is the charge required for the monolayer adsorption of hydrogen on a Pt surface ($210\mu Ccm^{-2}$) [8,9].

2.3.2 Oxygen Reduction Reaction

The catalytic activity of samples for the oxygen reduction reaction (ORR) was evaluated using the cyclic voltammetry setup. O_2 gas was introduced into the solution for 30 min to saturate the solution. While maintaining a small flow O_2 in the solution, cyclic measurements were conducted by cycling between 1 and 0.3V (vs RHE) at a scan rate of $50mVs^{-1}$. Current densities were normalized to the Pt loading of each sample.

2.3.3 Methanol Oxidation Reaction

The catalytic activity toward the methanol oxidation reaction was investigated in a N_2 saturated solution containing 1 M MeOH and 0.5M H_2SO_4. The samples were cycled between 0.05 and 1.2V (vs RHE) three times at a scan rate $50mVs^{-1}$.

2.3.4 CO stripping

To evaluate the CO tolerance of samples prepared, CO stripping voltammetry was carried out. In this method, pure CO (99.5%) was introduced into the solution for 30 min to achieve saturation, while the working electrode was polarized at 0.05V (vs RHE) in the fume hood. This will insure a CO monolayer on the catalysts. In the next step, excess CO is purged out by the introduction of N_2 gas into the solution for 30 min with the working electrode polarized at 0.05V (vs RHE). Cyclic voltammetry between 0.05 and 1.2V (vs RHE) was carried out at a scan rate of $50mVs^{-1}$ to strip the CO from the catalysts.

2.4 References:

[1]   Zhou Y, Zhang Y, Li R, Cai M and Sun X 2009 Journal of Materials Research 24 1833–1841

[2]   Gu G, Zheng B, Han WQ, Roth S and Liu J 2002 Nano Letters 2 849–851

[3]   Chen J, Li S-L, Gao F and Tao Z-L 2003 Chemistry of Materials 15 1012–1019

[4]   Li Y-H, Zhao YM, Ma RZ, Zhu YQ, Fisher N, Jin YZ and Zhang XP 2006 Journal of Physical Chemistry B 110 18191–18195

[5]   Liu H, Zhang Y, Li R, Sun X, Désilets S, Abou-Rachid H, Jaidann M and Lussier L-S 2010 Carbon 48 1498–1507

[6]   Yang D-Q, Sun S, Dodelet J-P and Sacher E 2008 The Journal of Physical Chemistry C 112 11717–11721

[7]   Sun S, Zhang G, Geng D, Chen Y, Li R, Cai M and Sun X 2011 Angewandte Chemie International Edition 50 422–426

[8]   Saha MS, Banis MN, Zhang Y, Li R, Sun X, Cai M and Wagner FT 2009 Journal of Power Sources 192 330–335

[9]   Sun S, Zhang G, Geng D, Chen Y, Banis MN, Li R, Cai M and Sun X 2010 Chemistry - A European Journal 16 829–835

Chapter 3

3 Spatial Sequential Growth of Various WSi$_2$ Networked Nanostructures and Mechanisms[1,2]

Recently transitional metal silicides, such as TiSi$_2$ have attracted significant interest in energy applications due to their excellent thermal stability, good corrosion resistance and superior electrical conductivity. In this chapter, the authors report the synthesis of WSi$_2$ nanostructures with controlled morphologies. Networked WSi$_2$ nanoribbons and nanosheets were synthesized using a chemical vapor deposition method and the growth mechanism of these nanostructures was studied via a series of controlled experiments. Our results indicate that the formation of WSi$_2$ nanostructures is governed by a vapor deposition method and the concentration of reactive species plays a crucial role in controlling the morphology of deposited nanostructures.

---

[1] Co-authors: Xiangbo Meng[a], Yong Zhang[1], Mei Cai[b], Ruying Li[a], and Xueliang Sun[a]

a. Department of Mechanical and Materials Engineering, The University of Western Ontario, London, Ontario N6A 5B9 (Canada)

b. General Motors R&D Center, Warren, MI 48090-9055 (USA)

Email: xsun@eng.uwo.ca

3.1   Introduction

The continuing dimensional shrinkage of conventional electronic devices requires new building blocks that are able to provide a high device density, especially through their novel nanostructures [1]. Among potential materials, metal silicides, a family of refractory, intermetallic compounds between metals and silicon, have attracted much interest, especially in the field of electronics [2–7] and energy [8–11] . Research on these materials is driven by their distinguished properties, such as high electrical conductivity [1–3,12], superior thermal [13] and chemical stability [13–15]. Metallic silicides including $TiSi_2$ [2,10], MnSi [16] and NiSi [5,6,17] have been used as interconnects in electronic devices due to their low contact resistance. In addition, these materials are attractive for high temperature applications as they usually have high melting points and show good oxidation resistance [13,14,18,19].

Recent studies focused on synthesizing nanostructured metal silicides, such as Ti_5Si_3 [1], $TiSi_2$ [10], $FeSi_2$ [4], $NiSi_2$ [11] and $TaSi_2$ [20], for the reduction on material dimensions to nanoscale often brought new physical phenomena and interesting applications [2,5,10,21]. However, synthesis of such materials with high melting point is still challenging. Previous studies demonstrated that complex nanostructures including nanonets or branched structures are favored to simple 1D nanostructures in many applications [2,8,9,22,23]. Consequently, they add additional challenges to a synthesis process. To overcome this difficulty, various efforts have been reported, for example, using silicon or metal nanowires as templates or chemical vapor deposition (CVD) methods via low temperature precursors [5].

Tungsten silicides (WSi_2, W_5Si_3) are among the refractory transition metal silicides and have high oxidation resistance [13,19,24]. Further, researchers have reported that tungsten silicides exhibit superconducting properties and have been studied as prime candidates for replacing doped polysilicon of low resistivity [12,25]. To date, there have been no reports on any growth of tungsten silicide nanostructures.

In this work, for the first time, we developed a facile method to synthesize high melting point tungsten silicide nanostructures from networked nanorods to nanoribbon nets to nanosheets by low pressure chemical vapor deposition (LPCVD). The method features the simultaneous growth of these nanostructures in different spatial zones. Through investigating time-dependent growth characteristics of these nanostructures of tungsten silicides, their growth mechanisms were proposed.

3.2   Experimental method

WSi_2 nanostructures were synthesized via a home-built LPCVD system. WCl_6 (Aldrich, 99.9%) and Si (Aldrich, 99%) powder were used as the starting materials. The carbon paper was used as the substrate. Carbon paper was chosen as the substrate due to their conductivity and porous structure, making it suitable for electrodes; for instance, as fuel cell backing in low temperature fuel cells. The substrates were placed on an alumina boat containing silicon powders. The source materials and substrates were placed inside a quartz tube. The tube was mounted horizontally in a furnace. WCl_6 powders were positioned in the low temperature region (200°C) and Si powders were situated in the high temperature region (900°C). The system was purged of oxygen by decreasing the pressure to 100Pa and flushing argon gas (Ar) into the system several times. The system was then heated to a set temperature with a heating rate of 10°Cmin^{-1} and kept at the temperature for 1 hour. In this period the pressure was kept at 500 Pa with a continuous flow of Ar (99.999% in purity). After cooling down to room temperature a dark layer was deposited on the substrates. Figure 3.1a illustrates the schematic arrangement of the CVD setup for the growth of tungsten silicide nanostructures.

The morphology of the products was observed under field emission scanning electron microscope (FE-SEM, Hitachi S4800) operated at 5.0 kV equipped with energy dispersive X-ray analysis (EDX), Transmission electron microscope operated at an accelerating voltage of 100 kV (TEM, Hitachi 7000). Further detailed morphology

characterization was carried out by high resolution transmission electron microscope (HRTEM, JEOL 2010) and selected area electron diffraction (SAED) operated at 200kV. The crystal structure and composition of the products was characterized by X-ray diffractometer using Cu Kα ($\lambda = 0.154$nm) radiation operated at 30 kV and 15 mA (XRD, Bruker D8). Electrochemical behavior of the samples was evaluated by cyclic voltammetry in 0.5M H_2SO_4 saturated with N_2 at room temperature using an Autolab potentiostat/galvanostat (model PGSTAT-30) scanned from -658 to 542 mV versus a saturated $Hg/HgSO_4$ (K_2SO_4) reference electrode at a scanning rate of 50mV/s.

3.3   Results & Discussion

3.3.1 Morphological and structural characterization

Figure 3.1 summarizes the various nanostructures synthesized on the carbon substrate in a single CVD experiment. Scanning electron micrographs (SEM, Figure 3.1b-d) show the three typical three-dimensional (3D) complex nanostructures changing from networked nanorods (Figure 3.1b, NNWs) to nanoribbon nets (Figure 3.1c, NRNs) and nanosheets (Figure 3.1d, NSs). These nanostructures were deposited at different spatial locations on the substrate. The diameter or thickness of the three morphologies, are commonly in the range of 6-10 nm. NNWs have an average diameter of 7nm and lengths up to several micrometers. NRNs and NSs are below 10 nm in thickness while their width and length are about a few micrometers.

XRD patterns (Figure 3.1e - g) reveal that these nanostructures have different crystalline structures and composition. The XRD pattern of NNWs (figure 3.1e) confirms the presence of two major tungsten crystal structures (JCPDS 04-0806, 65-6453). The weaker peaks can be assigned to WO_3 crystal structures. The results from NRNs and NSs (Figures 3.1f and g) show the presence of two types of silicides (W_5Si_3 – JCPDS 65-1617, WSi_2 – JCPDS 11-0195).
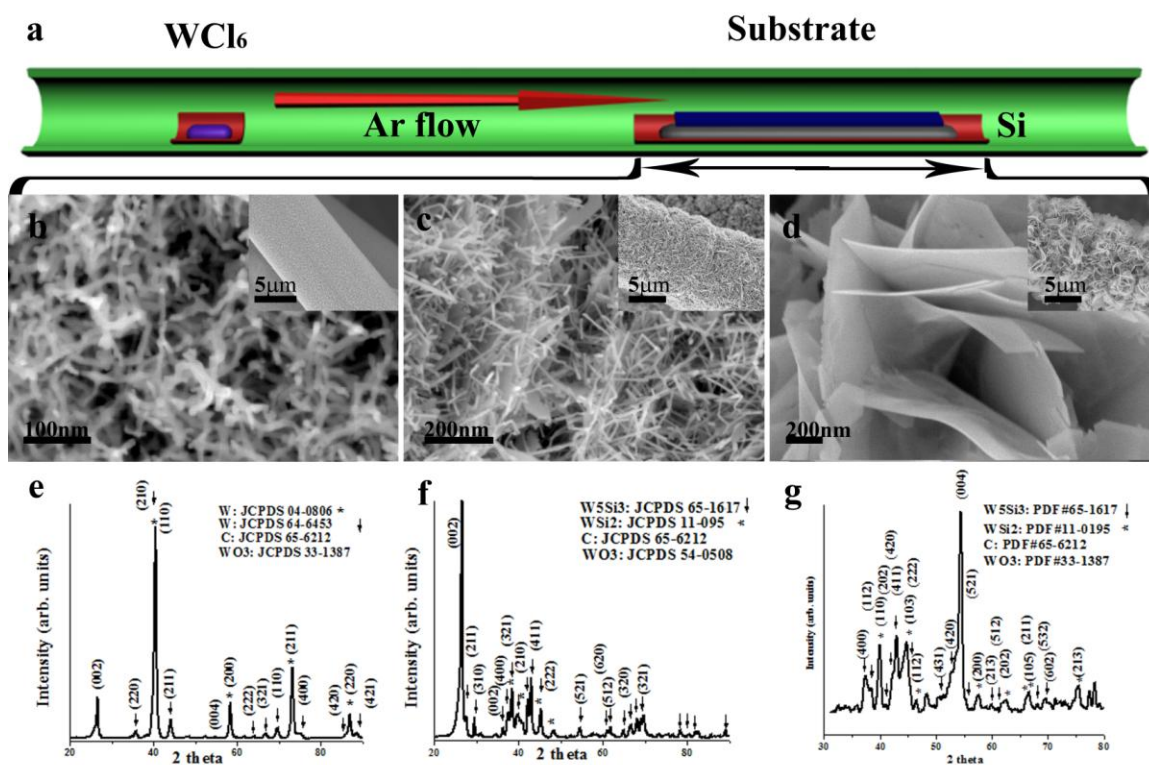
Figure 3.1 Growth of tungsten based nanostructure via one step CVD method. (a) schematic diagram of CVD setup. SEM and XRD pattern of (b, e) W networked nanorods, (c, f) WSix nanonets and (d, g) nanosheets.

HRTEM characterization of the obtained nanostructures further reveals the networked nature of these nanostructures. Figure 3.2 shows HRTEM images of tungsten based nanostructures and their evolution from tungsten networked nanowires (NNWs) into nanosheets (NSs). SAED patterns of these nanostructures reveal the crystalline nature of these complex nanostructures. Further observations of NNWs (Figure 3.2a) reveal a thin layer of 2 nm, covering the nanostructures and resulting in a core shell nanostructure. EDX analyses of these nanostructures indicate the presence of high atomic percentage of silicon and oxygen. This is attributed to the silicon oxide layer covering the NNWs. HRTEM image of these NNWs reveals clear lattice fringes, indicating a crystal structure with few defects. The *d* spacing of 0.22 nm measured from the HRTEM (Figure 3.2b)

corresponds to (210) plane of cubic metal tungsten, confirming the cubic structure of the tungsten NNWs (JCPDS 65-6453) with [210] growth direction.
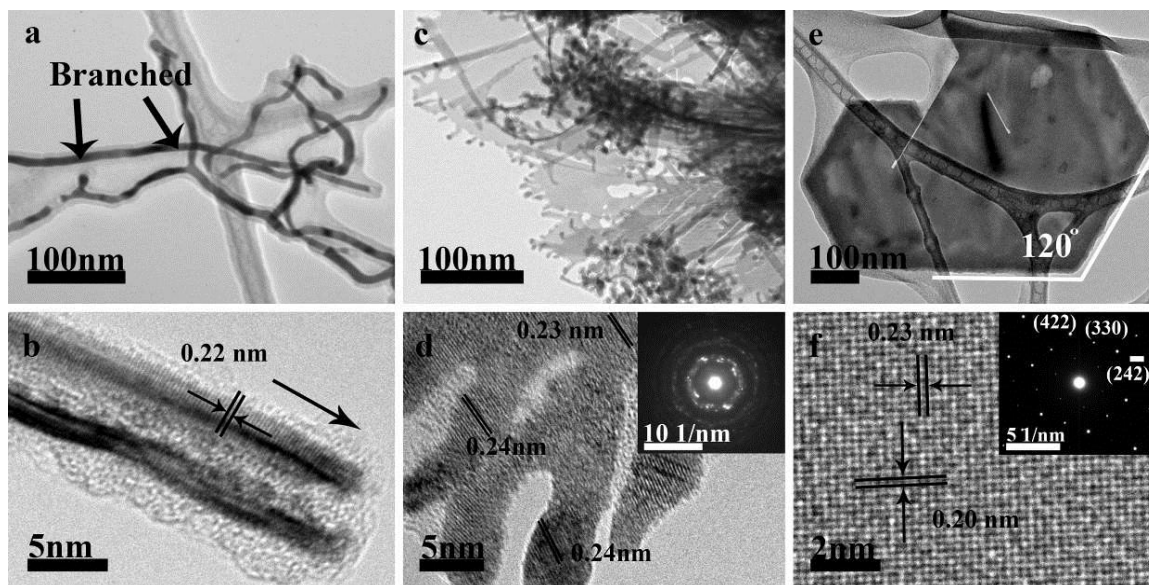
Figure 3.2 Morphology and structure of various nanomaterials deposited on the substrate depending on the concentration of tungsten species. (a, b) NNWs, (c, d) NRNs), (e, f) NS.

The TEM image of NRNs (Figure 3.2c) clearly shows ribbon and wall-like structures and the nanorods on the edges of these nanostructures forming net-like structures. The length of these nanorods is between 10nm to 30nm. The SAED pattern on these nanostructures (inset of Figure 3.2d) shows ring-like structures, indicating the presence of poly crystalline nanostructures. The SAED pattern reveals the presence of cubic WSi_2, confirmed by XRD pattern (Figure 3.1f). HRTEM analyses of these nanostructures (Figure 3.2d) indicate an increase in the distance between lattice fringes between nanosheets (0.23nm corresponding to ($24\bar{2}$) lattice planes of WSi_2 crystal structure) and nanorods (0.24nm). This can be attributed to change in the crystal morphology of these nanostructures.

Figure 3.2e shows TEM image of a single NS formed on the substrate. As seen in the image, the nanosheet nanostructures form trapezoid shapes with relatively sharp edges, exhibiting 120° angles. These nanostructures usually have few imperfections as shown in Figure 3.2e. SAED pattern of these nanostructures confirms that these nanostructures have a cubic WSi_2 crystal structure. The spacing between the lattice fringes also corresponds to the $(24\bar{2})$ and (404) lattice planes. This suggests that the nanosheets grow along equivalent planes enclosed with {111} planes of a cubic crystal structure (WSi_2).

3.3.2 Growth mechanism

For catalyst- assisted growth of nanostructures, the vapor-liquid-solid growth (VLS) mechanism has been widely accepted [1,26,27]. The presence of solidified droplets at tip of synthesized nanostructures is often considered to be the evidence of a VLS mechanism. In our study, however, no catalyst was employed for the growth of tungsten based nanostructures. TEM observations did not reveal the formation of any droplets at the tips of the nanostructures, indicating VLS is not the primary growth of the tungsten based nanostructures.

There have been several reports on the synthesis of various silicide thin films and nanostructures such as FeSi [21], $TiSi_2$ [10], WSi_2 [28] and NiSi [11] using metal chlorides. In those studies, silicon wafers were mainly used as substrates and silicon sources. The growth mechanism proposed was based on the reduction of metal chlorides and thereby the resultant formation of silicides and $SiCl_x$. In the mechanism, it was further believed that $SiCl_x$ could also induce the formation of silicides on Si substrates, following the vapor solid (VS) growth route. In VS-based growth processes free of catalyst droplets, attributed to their suitable environment for the reaction and growth of nanostructures, partial pressures of reactive species and crystal structure of nanomaterials are key factors in determining the composition and morphology of resultant nanostructures.

Based on our experimental results, VS growth mechanisms are proposed for the growth of tungsten-based nanostructures. However, different from the previous reports as discussed above, the silicide nanostructures in this study are mainly deposited on a non-silicon substrate. In addition, only one side of the substrate is covered by the nanostructures. In other words, the synthesis of the tungsten silicide nanostructures in this study features the evaporation of both silicon and tungsten reactive species.

Based on the facts discussed above and the contributions of Thomas et al. [28] from their simulation and experimental results, we speculate that our deposition of tungsten silicide on the substrate might have taken the following routes:

1) $\qquad$ $2WCl_6 + 3Si \rightarrow 2W + 3SiCl_4$

2) $\qquad$ $6WCl_6 + 14Si \rightarrow W_5Si_3 + WSi_2 + 9SiCl_4$

3) $\qquad$ $SiCl_4 + 2H_2O \rightarrow SiO_2 + 4HCl$
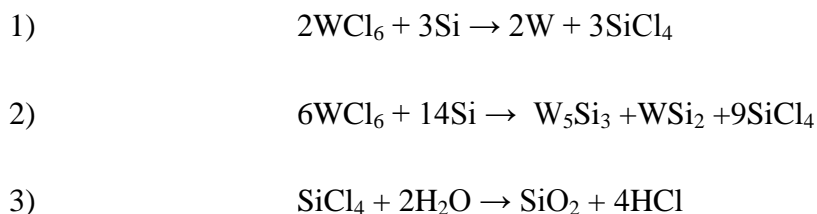
In the above reactions, the formation of silicon chloride species by reduction of metal chlorides has also been proposed for the deposition other silicides such as $TiSi_2$ [29]. In particular, the formation of tungsten and silicon chloride vapors in reaction 1- and the formation of silicides in reaction 2- are in good agreement with our results obtained on non-silicon based substrates.

In this study, ascribed to the nature of CVD processes and the use of powder-based source materials, the concentration of WCl_6 decreases of along the chamber as it continuously reacts with Si to form tungsten-based nanostructures. Upon this point, EDX results (support information 1) and XRD results (Figure 3.1) provided the direct evidence. Thus, it is believed that the formation of various tungsten based nanostructures is closely related to the gradient concentration of WCl_6 along the chamber, especially along the substrate. EDX analyses of the three types of nanostructure show the presence of oxygen, tungsten and silicon in all of the morphologies. It can be seen that NNWs have the highest tungsten to silicon (W/Si) ratio. The W/Si ratio decreases in NRNs and NSs.

This trend is consistent with the XRD patterns (Figures 5.1e-g), suggesting a decrease in the concentration of tungsten species along the CVD chamber compared to silicon species.

3.3.3 NNWs growth mechanism

Thomas et al.[28] have reported that, under high tungsten chloride partial pressures and in the presence of lower partial pressures of silane, the formation of tungsten thin film dominates the deposition of other types of tungsten silicides. In this study, at the initial section of the reaction area (silicon powder containing section), where the concentration of WCl_6 is highly dominant compared to Si based on reaction 1, tungsten networked nanorods are formed. In this stage, $SiCl_4$ reacts with residual oxygen in the system (oxygen trapped between powders, leakage in the system and in carrier gas) forming a thin layer of SiO_2 (reaction 3) around the tungsten network structures (Figure 3.2a, b).

The branching of NNWs (networked structure) is clearly marked in Figure 3.2a. Based on reports of the synthesis of branched nanostructures, branching can be induced by several processes. The branched growth is mainly reported in vapor-liquid-solid (VLS) based processes. In this growth mechanism, either catalyst nanoparticle is added to the growth process sequential (sequential seeding) or the catalyst nanoparticles are formed during the synthesis procedure (in situ seeding) [30]. The characteristic feature in VLS processes is the formation of droplet on the tip of the nanostructures.

The branched and complex nanostructures can also be obtained without catalyst induced growth, such as growth by occurrence of phase transition or difference in surface energy of crystal structures [30]. In these methods, the growth process is mainly based on VS mechanism. The growth of branched nanostructures is achieved, by anisotropic growth of crystal structures from different crystal planes with different surface energies. This difference can be intrinsic feature of the crystal structure or can be induced by passivation of specific crystal planes. In this study, it is predicted the NNWs grow via VS growth

mechanism. The networked nature of NNWs is induced by anisotropic growth of the crystal structures.

3.3.4 NRNs and NSs growth mechanism

In the middle and end sections of the reaction area, the concentration of the two reactive species are balanced due to decrease in depletion of tungsten chloride and increase in the partial pressure of Si and tungsten silicide compounds are formed (reaction 2). This is in accordance with simulation and experimental results reported by Thomas et al.[28].

 Based on the HRTEM analysis of NRNs and NSs (Figure 3.2c-f), these two types of nanostructures share similar nanowall-like structures. This indicates a similar growth condition in their deposition areas.

It is interesting to note that in this section nanosheet and nanoribbon-like structures have grown on a low surface energy crystal plane. Previously, there have been many reports on the growth of nanosheets and nanoribbons. For the synthesis of metal oxide nanosheets such as Al_2O_3 nanobelts, Zhang et al.[31] have proposed that the excessive supersaturation level of aluminum suboxide and high oxygen partial pressure in the synthesis process play key roles in the formation of 2D nanostructures. Furthermore, Ye et al.[32] have claimed that the non-equilibrium kinetic growth caused by high supersaturation of reactive species may allow the formation of a low surface energy tip, which favors 2D growth of the nanostructures.

In contrast to the above-discussed work, the nanostructures from our work are not synthesized in the low surface energy direction. Further experimental results indicate that the increase in the partial pressure of oxygen reduces the density of 2D nanostructures and promotes the growth of WSi_2 networked nanowires.

The effect of oxygen partial pressure on the growth of silicide, sulfides and metals nanocrystals such as FeSi [21] and digenite [33] via metal chloride precursors was

studied by Zhang et al. They reported the controlled growth of nanosheets and nanowires by control of SiO_2 vapor pressure via oxygen partial pressure. Zhang et al [21,33] showed that SiO_2 vapor pressure plays an important role in the determining the morphology of nanostructures. They proposed a growth mechanism based on partial coverage of low surface energy planes nanocrystals by silica sheath, such as (111) planes in a digenite FCC crystal. In this mechanism, at the first stage silica clusters are adsorbed on to only several of many low surface energy planes (e.g 2 of 8 (111) planes in FCC structure) crystal seeds due to low silica vapor pressure. At the second stage, since the silica vapor pressure is low, the silica sheath coverage will reach the critical level on some of the crystal planes rather than simultaneously on all of the similar planes. At this stage, the 2D growth of nanocrystals is induced due to the positive feedback between the imbalance of silica coverage on different planes and the net mass diffusion associated with the imbalance. This process leads faster growth of nanosheets with clear facets.

In our case, we propose that, under our experimental conditions, the partial pressure of oxygen in the system is induced by air leakage, residue oxygen and oxygen trapped in the system. Under the low oxygen partial pressure, silica vapor is formed via silicon partial pressure over the silicon substrate and by following reaction (3). At the first stage during the experiment, a layer of W_5Si_3 is formed on the substrate (supported by XRD and HRTEM results) which provides a suitable substrate for the formation of WSi_2 nuclei. In the second stage, following the growth mechanism proposed by Zhang et al.[33], the silica clusters are formed on one of the (111) planes of the WSi_2 cubic crystal. At the third stage, the silica coverage of the (111) plane reaches a critical point, causing an imbalance of silica coverage which results in net mass diffusion of tungsten and silicon species on to (121) planes and growth of nanoribbons and nanosheets.

The growth of nanorods on the tip of nanoribbons can be attributed to decrease in the partial pressure of WCl_x near the end of the experiment. This results in the increase of silicon partial pressure and consequently the increase of silica vapor pressure. At these conditions, based on the proposed growth mechanism, the synthesis of WSi_2 nanowires

and nanosheets occur simultaneously, resulting in the formation of NRNs with small nanorods at their tips (figure 3.1c).

To further understand the growth mechanism of WSi_2 nanostructures, a time-dependent growth study was carried out. As seen in figure 3.3, at the initial stages of synthesis process (figure 3.3a, 5min) the substrate is covered by a thick layer composed of nanoparticles with diameters below 5nm (formation of W_5Si_3 layer). Based on results shown by Thomas et al.[28], the formation of W_5Si_3 is favorable compared to WSi_2 in higher tungsten chloride and lower hydrogen partial pressures, so in the beginning of the experiments W_5Si_3 thin film is formed. At this stage, small networked nanorod and nanosheet-like structures were seen to grow on top of the deposited layer. This result confirms that the growth of tungsten silicide starts from the substrate. At this stage, the nanoparticles act as nuclei for the growth of complex nanostructures.
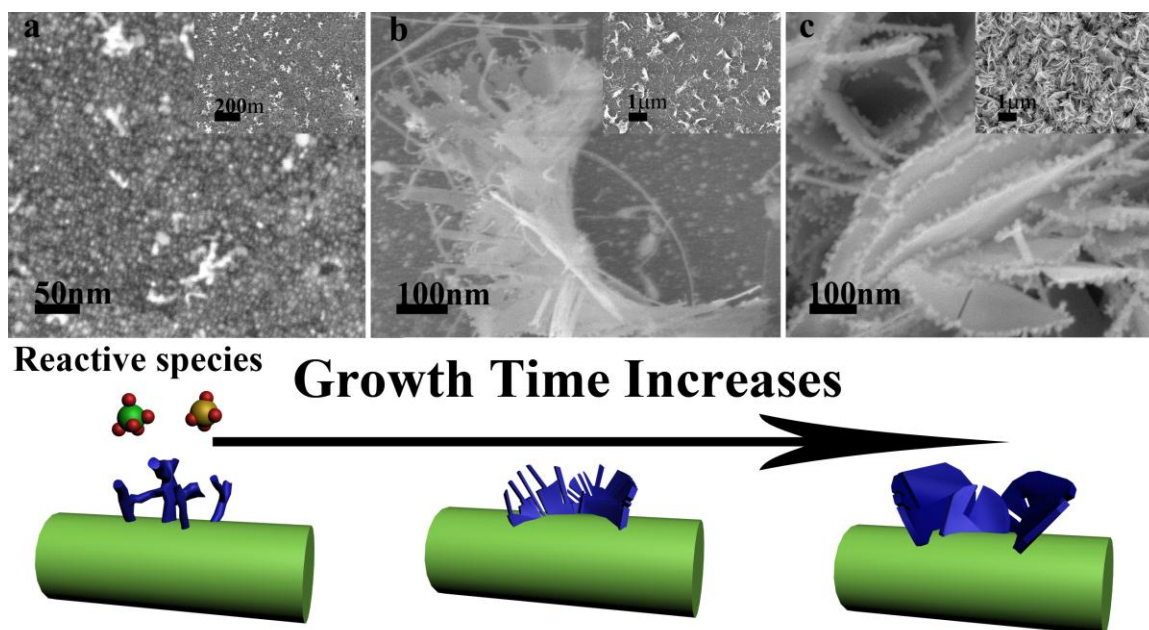
Figure 3.3 Time dependent evolution of nanoparticles into NSs. a) 5min, b) 15min, c) 45 min. d) Schematic diagram of growth processes of NSs.

By increasing the time (Figure 3.3b, 15min), low density of networked nanoribbons are synthesized on the deposited layer. These nanostructures, compared to NRNs shown in Figure 3.1c, have similar morphology and structure. A further increase in time (Figure 3.3c, 45min) resulted in the high density growth of NSs. Figure 3.3d shows a schematic illustration of the growth of WSi_2 nanostructures.

These results illustrate the evolution of NRNs into NSs, suggesting the dependence of WSi_2 NSs growth on the partial pressure of reactive species (specifically WCl_6 and oxygen) and growth time. The increase in time increases the amount of reactive spices reaching the growth front of the nanostructures (similar to higher concentration at a shorter time). At this point, the nanostructures start to grow in two dimensions filling the voids between the nanoribbons and forming nanosheets.

Recent reports have shown that nanostructures with various morphologies exhibit different capacitance performance [34,35]. Therefore we have studied the electrochemical capacitance behavior of WSi_2 nanostructures synthesized using CVD method. Figure 3.4 shows the normalized cyclic voltammograms of the WSi_2 nanostructures without any pre-treatment. From a comparison of line a) and b) in Figure 3.4, the area under the CV curve for WSi_2 NSs is apparently larger than the WSi_2 NNRs. This indicates that the WSi_2 nanosheets have a higher capacitance than that of WSi_2 networked nanoribbons. Similar to previous reports, this can be due to the higher surface and larger micropore area of the nanosheets compared with the networked nanoribbons [34,35]. This result implies that WSi_2 nanostructures especially nanosheet morphologies could be considered as promising material in the application of nanodevices for electrochemical energy storage. However, due to presence of SiO_2 shell layer, it is a challenge to calculate the exact capacity of the nanostructures. Further study is needed in our work.
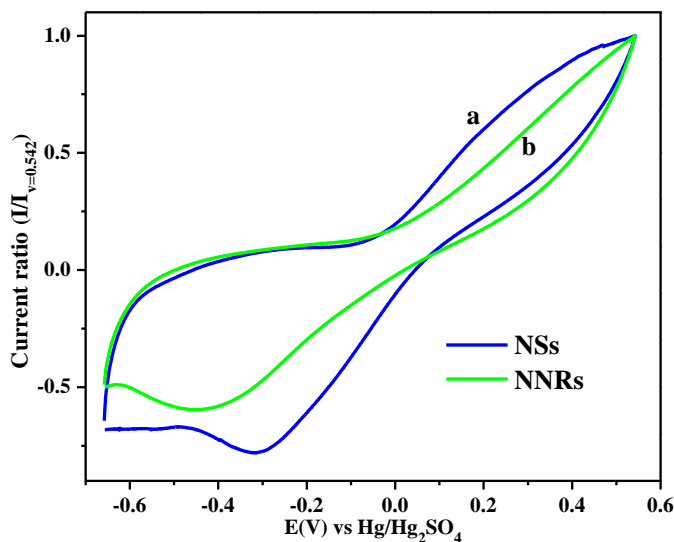
Figure 3.4 Cyclic voltammetry of the WSi2 nanostructures (normalized to current at V=0.542 V). a) NSs and b) NNRs.

3.4   Conclusions

For the first time, we have synthesized single crystalline WSi_2 nanonets and nanosheets on carbon paper substrates in a one-step LPCVD method. The concentration changes of the tungsten precursor and partial pressure of oxygen can bring the products with a wide range of morphologies and composition. The growth mechanism of the tungsten silicide nanostructures is proposed based on the formation of silica sheath on several (111) plane of WSi_2 nanostructures and morphological evolution with the growth time. These nanostructures are formed in three stages: i) forming nanoparticles, ii) growing into nanonets and iii) evolving to nanosheets. Cyclic voltammetry measurements of the nanostructures indicate that WSi_2 nanostructures show superior electrochemical capacitance with WSi_2 NSs exhibiting higher capacitance compared to WSi_2 NNRs. These nanostructures are expected to be great potential material for nanodevices and electrochemical applications.

Acknowledgements

3.5   References

[1]   Zhang Y, Geng D, Liu H, Banis MN, Ionescu MI, Li R, Cai M and Sun X 2011 Journal of Physical Chemistry C 115 15885–15889

[2]   Zhou S 2008 Angewandte Chemie International Edition 47 7681–7684

[3]   Li-Jen Chou, Yu-Lun Chueh and Mong-Tzong Ko 2007 Thin Solid Films 515 8109–8112

[4]   Kim T and Bird JP 2010 Applied Physics Letters 97 263111-263114

[5]   Schmitt AL, Higgins JM, Szczech JR and Jin S 2010 Journal of Material Chemistry 20 223-235

[6]   Jiang S, Xin Q, Chen Y, Lou H, Lv Y and Zeng W 2009 Applied Physics Express 2 75005-75009

[7]   Chenxia Zou, Xinzheng Zhang, Guangyin Jing, Jingmin Zhang, Zhimin Liao and Dapeng Yu 2008 Applied Physics Letters 92 253102–253105

[8]   Lin Y, Zhou S, Liu X, Sheehan S and Wang D 2009 Journal of the American Chemical Society 131 2772–2773

[9]   Zhou S, Liu X and Wang D 2010 Nano Letters 10 860–863

[10]   Zhou S, Liu X, Lin Y and Wang D 2009 Chemistry of Materials 21 1023–1027

[11]   Zhang H-L, Li F, Liu C and Cheng H-M 2008 Nanotechnology 19 165606-165610

[12]   Cheb JL 2005 Journal of the Minerals, Metals and Materials 57 24–30

[13]   Chirkin AD, Lavrenko VO and Talash VM 2009 Powder Metallurgy and Metal Ceramics 48 330–345

[14]   Mitra R 2006 International Materials Reviews 51 13–64

[15]   Meschter PJ and Schwartz DS 1989 Journal of the Minerals, Metals and Materials 41 52–55

[16]   Liu HJ, Owen JHG, Miki K and Renner C 2011 Journal of Physics: Condensed Matter 23 172001-172006

[17]   Wen Z, Ji S, Sun J, Tian F, Tian R and Xie J 2006 Rare Metals 25 77–81

[18]   Fitzer E and Remmele W 1987 Materials science and engineering 88 349-353

[19]   Patnaik PC 1989 Materials and Manufacturing Processes 4 133–152

[20]   Yu-Lun Chueh, Mong-Tzong Ko, Li-Jen Chou, Lih-Juann Chen, Cen-Shawn Wu and Chii-Dong Chen 2006 Nano Letters 6 1637–1644

[21]   Zhang H-X, Ge J-P, Wang J and Li Y-D 2006 Nanotechnology 17 253–261

[22]   Lin Y 2011 Journal of the American Chemical Society 133 2398–2401

[23]   Elmalem E 2008 Advanced Materials 20 4312–4317

[24]   Schultes G, Schmitt M, Goettel D and Freitag-Weber O 2006 Sensors and Actuators, A: Physical 126 287–291

[25]   Reader AH, van Ommen AH, Weijs PJW, Wolters RAM and Oostra DJ 1993 Reports on Progress in Physics 56 1397–1467

[26]   Banis MN, Zhang Y, Banis HN, Li R, Sun X, Jiang X and Nikanpour D 2011 Chemical Physics Letters 501 470–474

[27]   Rao CN., Deepak F., Gundiah G and Govindaraj A January Progress in Solid State Chemistry 31 5–147

[28]   Thomas N, Dutron AM, Vahlas C, Bernard C and Madar R 1995 Journal of Electrochemical Society 142 1608–1614

[29]   Bouteville A, Remy JC and Attuyt C 1992 Journal of Electrochemical Society 139 2260–2263

[30]   Liu X, Lin Y, Zhou S, Sheehan S and Wang D 2010 Energies 3 285–300

[31]   Yong Zhang, Ruying Li, Xiaorong Zhou, Mei Cai and Xueliang Sun 2008 Journal of Nanomaterials 1–8

[32]   Ye C, Fang X, Hao Y, Teng X and Zhang L 2005 Journal of Physical Chemistry B 109 19758–19765

[33]   Zhang H-X, Ge J-P and Li Y-D 2006 Journal of Physical Chemistry B 110 14107–14113

[34]   Xiong S, Yuan C, Zhang X, Xi B and Qian Y 2009 Chemistry – A European Journal 15 5320–5326

[35]   Yang S-Y, Chang K-H, Tien H-W, Lee Y-F, Li S-M, Wang Y-S, Wang J-Y, Ma C-CM and Hu C-C 2011 Journal of Materials Chemistry 21 2374-2380

Chapter 4

4   Tailoring Growth of Single Crystalline Complex Ta$_5$Si$_3$ Nanostructures: From Networked Nanowires to Nanosheets[1,2]

Following the previous chapter on the synthesis of tungsten silicide nanostructures, similar concept was used to synthesize Ta$_5$Si$_3$ nanostructures with controlled morphology on conductive substrates.

In this chapter, the authors report the synthesis of Ta$_5$Si$_3$ networked nanowires and nanosheets via chemical vapor deposition method. It was found that the formation of Ta$_5$Si$_3$ nanostructures is based on vapor solid growth mechanism and is highly sensitive to vapor pressure of tantalum chloride and silica. Structure characterization indicates that with the decrease of silica vapor pressure, the Ta$_5$Si$_3$ networked nanowires evolve into networked nanoribbons and nanosheets via two dimensional growth. Cyclic voltammetry measurements of Ta$_5$Si$_3$ nanostructures show their superior electrochemical capacitance. It is expected that these nanostructures have great potential applications for nanodevices in electronic and energy related applications.

[1] Co-authors: Yong Zhang[a], Mei Cai[b], Ruying Li[a], and Xueliang Sun[a]

a. Department of Mechanical and Materials Engineering, The University of Western Ontario, London, Ontario N6A 5B9 (Canada)

b. General Motors R&D Center, Warren, MI 48090-9055 (USA)

Email: xsun@eng.uwo.ca

4.1   Introduction

As a family of intermetallic compounds between metals and silicon, metal silicides have attracted great interest owing to their excellent electrical properties [1−6] and superior thermal stability[5−7] and oxidation resistance [6]. These materials constitute an important group of compounds that are used in modern silicon based microelectronics [1−3,6,8,9] and optoelectronic devices [10,11]. Metal silicides have been used as ohmic contacts [2,3,12], interconnect [3,12] and gate materials for CMOS microelectronic transistors [3,13,14] or stable, inexpensive thermoelectric materials [2,15].Rapid progress in microelectronics and miniaturization of electronic devices requires the dimensional shrinkage of its components including metal silicides [3,4,9,13,16]. For this purpose, extensive research has been focused on the synthesis of single crystalline one dimensional metal silicide nanostructures such as Ti_5Si_3 [4], $TiSi_2$ [17], $FeSi_2$ [18], $NiSi_2$ [19] and $TaSi_2$ [3,5,12]. Due to their high melting point and susceptibility to form silicon or metal oxide, however, the controlled synthesis of metal silicide nanostructures is challenging. Various methods based on vapor deposition process such as silicidation of metal nanowires or use of metal halides and chlorides have been developed [2].

Recently tantalum silicide nanostructures such as $TaSi_2$ nanowires have been synthesized by annealing $FeSi_2$ and $NiSi_2$ thin films on silicon substrate in an ambient containing Ta vapor [3,5,12]. $TaSi_2$ is a promising material as field emitters in field emission applications and interconnections between individual nanodevices due to their metallic characteristics and high thermal stability [5,12]. Ta_5Si_3 thin films have also been studied for high temperature applications and as thermoelectric materials [7,15].

Here, we report a facile method for the synthesis of tantalum silicide networked nanostructures by low pressure chemical vapor deposition method (LPCVD). The growth mechanism of the unique nanostructures based on the formation of silicon oxide passive layer is discussed in detail. We found the overall shape and crystal structure of the products is sensitive to composition of the carrier gas and partial pressure of silica on the surface of the substrate.

4.2   Experimental procedure

Ta_5Si_3 nanostructures were synthesized via a home built LPCVD system. $TaCl_5$ (Aldrich, 99.9%) and Si (Aldrich, 99%) powder were used as the starting materials. The commercially available carbon paper obtained from E-TEK, a division of De Nora North America, Somerset, NJ, composed of carbon microfibers of 5-10 μm in diameter was used as substrates. The substrates were placed on an alumina boat covering the silicon powder. The source material and the substrates were inserted in a quartz tube and it was mounted on a horizontal electric furnace. $TaCl_5$ powder was positioned upstream in the CVD chamber (200^oC) and Si powder was placed in the high temperature region (900^oC). To purge the oxygen from the system, the pressure in the CVD chamber was decreased to 100Pa. Argon was flushed into the system, increasing the pressure to over 5 kPa. This was repeated three times. The system was then heated to a set temperature with a heating rate of 10^oCmin^{-1}, and kept at this temperature for 1 hour. During the experiment, the pressure inside the chamber was maintained at 500 Pa with a continuous flow Ar (purity, 99.999%) which also acted as the carrier gas. After cooling down to room temperature, a dark layer was deposited on the substrate.

The morphology of the products was examined under field emission scanning electron microscope (SEM, Hitachi S4800) operated at 5.0 kV equipped with energy dispersive X-ray analysis (EDX), Transmission electron microscope operated at an accelerating voltage of 100 kV (TEM, Hitachi 7000). Further detailed morphology characterization was carried out by high resolution transmission electron microscope (HRTEM, JEOL 2010) and selected area electron diffraction (SAED) operated at 200kV. The crystal structure of the products was characterized by X-ray diffractometer using Co Kα (λ = 0.179nm) radiation operated at 30 kV and 15 mA (XRD, Bruker D8). Electrochemical behavior of the samples was evaluated by cyclic voltammetry in 0.5M H_2SO_4 saturated with N_2 at room temperature using an Autolab potentiostat/galvanostat (model PGSTAT-

30) scanned from -658 to 542 mV versus a saturated Hg/HgSO$_4$ (K$_2$SO$_4$) reference electrode at a scanning rate of 50mV/s.

4.3   Results and Discussion

Figure 4.1a,b shows high density of as-grown products synthesized along the CVD chamber. The reaction area can be divided into two regions based on the typical morphologies of nanostructures deposited in these areas. In the initial region (upstream), networked nanowires (NNWs, Figure 4.1a) and in the end region networked nanoribbons and nanosheets (NNRs and NSs, Figure 4.1b) were deposited on the carbon microfibers.

SEM observations indicate (Figure 4.1a), NNWs have lengths up to tens of micrometers. The major diffraction peaks from the XRD analysis of these nanostructures shown in Figure 4.1c could be ascribed to the tetragonal Ta$_5$Si$_3$ phase (JCPDS 65-2780) which is the most stable form of Ta$_5$Si$_3$ at room temperature (D8$_1$). The remaining peaks were assigned to Ta$_5$Si$_3$ (JCPDS 65-3598) and TaSi$_2$ (JCPDS 65-3548).

SEM images (Figure 4.1b) of NNRs deposited on the substrate show comparable dimensions to NNWs, with lengths up to tens of micrometers and an average thickness of 15nm. These nanostructures have well defined shapes with sharp edges, indicating a well crystallized structure. Detailed SEM observations reveal the presence of branched NNRs and small imperfections and gaps in the NSs. These features can be an indication of two-dimensional growth of nanostructures along the CVD chamber. According to the XRD pattern (Figure 4.1d), similar to NNWs, the major phase in this reaction region is the tetragonal Ta$_5$Si$_3$ phase (JCPDS 65-2780). However, XRD patterns indicate the minor phases are composed of TaSi$_2$ (JCPDS 65-2696) and Ta$_{0.83}$O$_2$ (JCPDS 28-1277). The increase in the concentration of oxygen along the CVD chamber and the presence of tantalum oxide is confirmed by the EDX results.
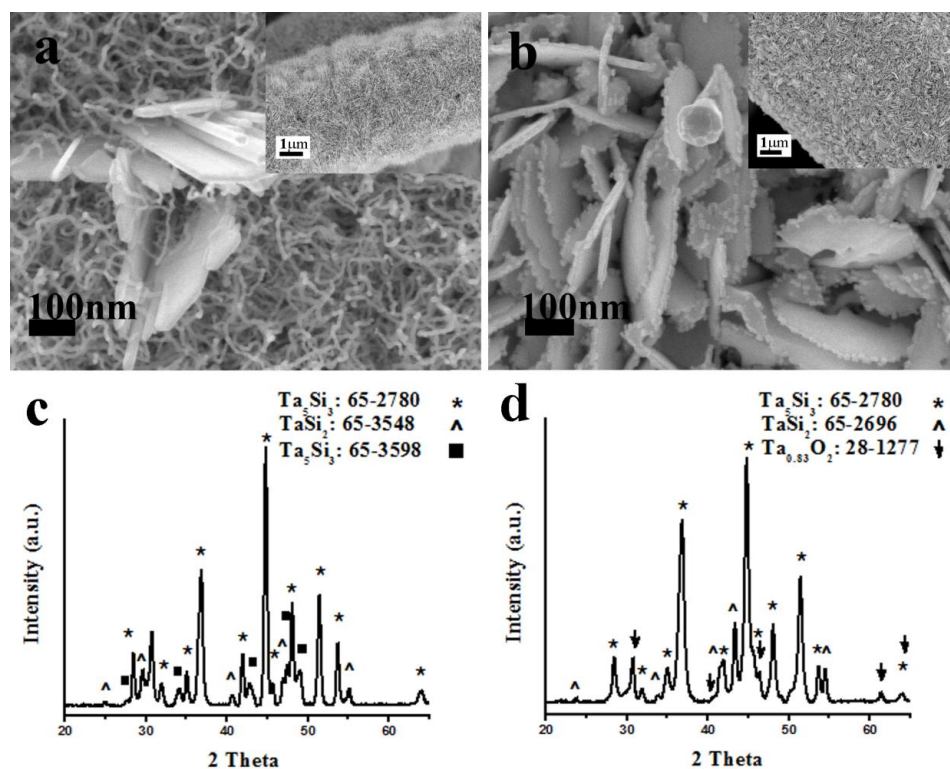
Figure 4.1 SEM images and XRD pattern of nanostructures deposited along the CVD chamber: a,c) initial section (NNWs) and b,d) end section (NNRs and NSs) of the reaction area.

TEM and HRTEM analysis further reveals the unique crystal structures of as deposited nanomaterials. TEM images (Figure 4.2a) of NNWs clearly illustrate the branching of these nanostructures. As shown in Figure 4.2a, the branches exist in planes perpendicular to the nanowires, which is consistent with the tetragonal symmetry ($D8_1$) of Ti_5Si_3. Furthermore, TEM images reveal these nanostructures have a core shell structure with an average inner diameter of 13nm and a shell thickness of 2nm. Figure 4.2b, a HRTEM image of the core section of a NNW clearly shows lattice fringes, confirming the single crystalline nature of the NNWs. The selected area electron diffraction (SAED) pattern obtained from the NNWs (inset Figure 4.2b) shows a regular spot pattern, which can be fully indexed to the tetragonal ($D8_1$) Ta_5Si_3 crystal structure (JCPDS 65-2780). This pattern is in a good agreement with the XRD results shown in Figure 4.1c. The lattice

spacing of 0.33nm measured in Figure 4.2b, corresponds well to {200} planes of the Ta$_5$Si$_3$ phase identified in the SAED pattern, indicating <010> to be the growth direction of the NNWs. The lack of lattice fringes in the HRTEM observation of the shell section covering the Ta$_5$Si$_3$ nanostructures and the well-ordered SAED pattern reveal the amorphous nature of the shell. EDX analysis of these nanostructures demonstrates the presence of oxygen on the nanostructures, which leads to the assumption of SiO$_x$ layer formation on the Ta$_5$Si$_3$ nanostructures.
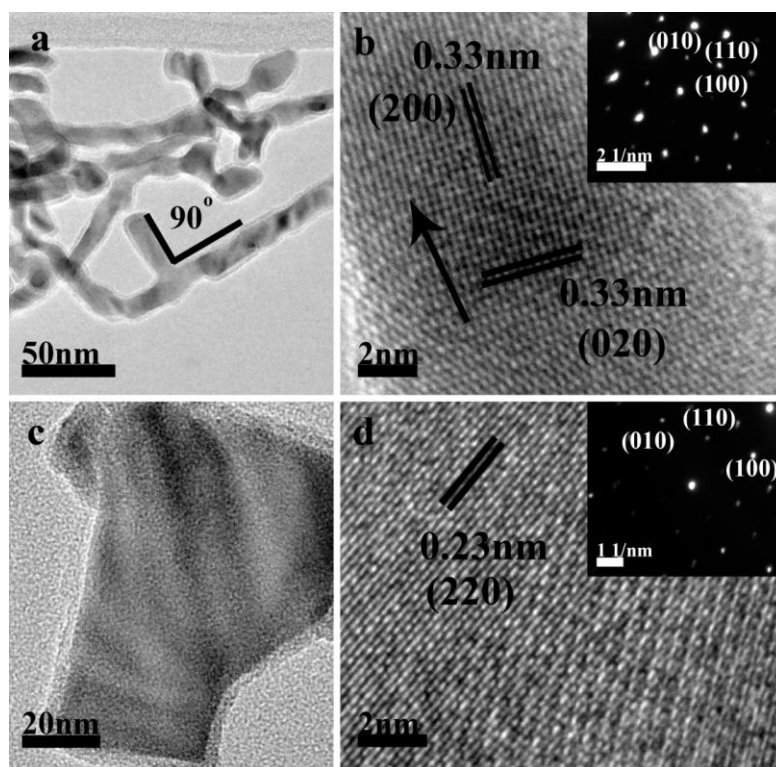
Figure 4.2 TEM and HRTEM images of a,b) NNWs and c,d) NNRs and NSs.

TEM image of NNRs and NSs is shown in Figure 4.2c, showing 90° edges. This suggests a two dimensional growth of these nanostructures similar to NNWs. Furthermore, as seen in NNWs, an amorphous SiO$_x$ layer with an average thickness of 2nm covers the NNRs. The lattice fringes clearly shown in the HRTEM image of these nanostructures (Figure 4.2d) implies these nanostructures to be single crystalline and the respective SAED pattern (inset of Figure 4.2d) corresponds to the tetragonal Ta$_5$Si$_3$ crystal structure

(JCPDS 65-2780). The lattice spacing of 0.22nm shown in Figure 4.2d can be matched to {220} plane of this crystal structure.

4.3.1 Time dependent growth of nanostructures

To better understand the morphological evolution and formation of networked nanoribbons, and demonstrate the relationship between the growth of these nanostructures and network nanowires, a time dependent growth study was carried out in the end section of the reaction area. Figure 4.3 shows the morphological evolution of nanostructures deposited on the substrates in the NNR and NSs growth region vs time.
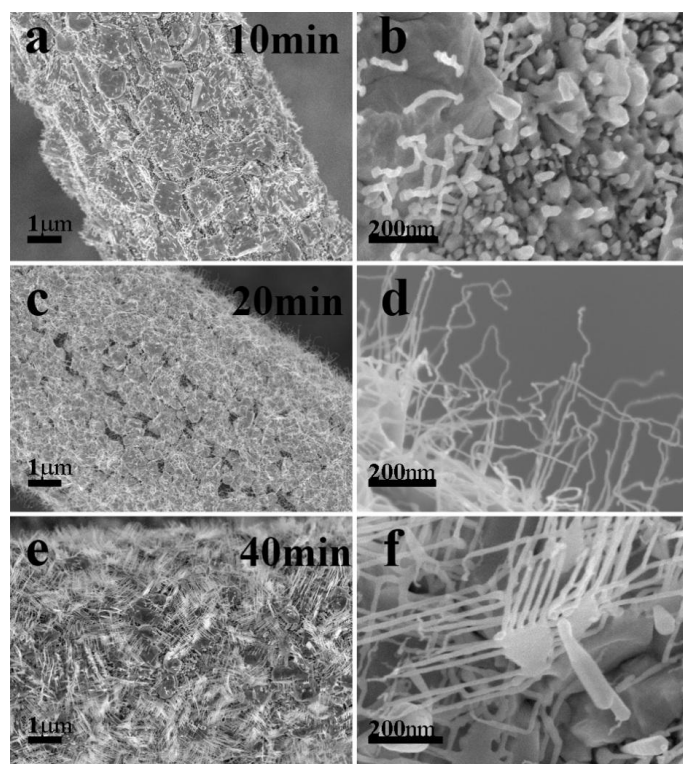
Figure 4.3 Evolution Ta$_5$Si$_3$ nanostructures deposited on carbon microfiber in the end section of the reaction area by the increase of experiment time: a,b) 10min, c,d) 20min, e,f) 40min.

As shown in Figure 4.3a, a thin layer composed of nanoparticles and micro particles are deposited on the substrate during the initial stages of the growth process. In this stage indicated by the arrows, these nanoparticles and edges of microparticles act as nucleate sites for the growth of small nanorods.Based on the XRD results (Figure 4.1) and HRTEM (Figure 4.2) observations of the Ta_5Si_3 nanostructures, it is assumed that these nanoparticles have similar crystal structures to the synthesized nanostructures (Figure 4.3b). By increasing the growth time, the nanorods grow into networked nanostructures. Further increase of synthesis time results in the development of the networked nanorods into nanoribbons and nanosheets, with nanoribbons nanowires extending from their tips indicating a two dimensional growth with different growth rates. In addition, these observations clarify the presence of imperfections between the NNRs and NSs.

4.3.2 Growth Mechanism

4.3.2.1 Ta_5Si_3 Formation

Based on the above results, a growth mechanism can be proposed for the growth of Ta_5Si_3 nanostructures. Independent of synthesis method in vapor based processes, two main growth mechanisms have been proposed for the synthesis of metal containing nanostructures. Catalyst assisted growth of nanostructures of vapor–liquid-solid mechanism (VLS) has been proposed for the growth of many metal based nanostructures [4,20]. This mechanism mainly features the presence of solidified droplets at the tip of synthesized nanostructures. The lack of a catalyst nanoparticles and the absence of these droplets at the tip of Ta_5Si_3 nanostructures imply the growth is not governed by VLS mechanism. The main catalyst free growth of nanostructures is vapor solid mechanism (VS). In this mechanism, the synthesis of nanostructures is influenced primarily by the crystal properties of nanostructures deposited, the substrates, and chemical species in the synthesis chamber.

In this study, similar to previous reports on the synthesis of metal silicides, a VS growth mechanism can be employed to explain the growth of Ta_5Si_3 nanostructures. However, in contrast to previous reports, the silicide nanostructures are mainly deposited on a non-

silicon substrate and experimental results show that the morphology of the nanostructures is sensitive to growth parameters.

Several studies have reported the formation of Ta_5Si_3 via the reaction between $TaCl_5$ and silicon species such as SiH_4 for synthesis of thin films [21,22]. Williams et al [21] studied the deposition of Ta_5Si_3 and $TaSi_2$ via reaction of $TaCl_5$ with different silicon sources such as solid silicon and SiH_4. They proposed a several possible reactions between the precursors and concluded the crystal structure and stoichiometry of the final product is dependent on the ratio of tantalum and silicon reactive species.

Based on the experimental observations in this study and reports on the synthesis of $TaSi_x$ thin films, it is suggested that the deposition of tantalum silicides occurs via the following reaction:

$$20TaCl_5 + 37Si \rightarrow 4Ta_5Si_3 + 25SiCl_4 \qquad (4.1)$$
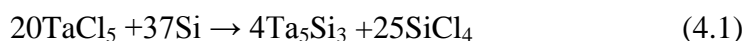
The formation of SiO_2 layer observed around the nanostructures deposited on the substrates can occur via reaction between the silicon reactive species such as silicon chloride formed in reaction 4.1 and oxygen in the CVD chamber. The origin of oxygen is assumed to be from air leakage, residue oxygen in the chamber and oxygen trapped in the system or source material.

4.3.2.2   Networked Nanostructure Formation

To explain the formation of various morphologies along the CVD chamber and propose a growth mechanism, a good understanding of the conditions in the CVD chamber is required. In this study, as observed under SEM, the morphology of Ta_5Si_3 nanostructures gradually evolves, implying a gradual change in the experimental conditions along the CVD chamber. Careful setup of CVD system insured a consistent temperature and gas flow in the experiment chamber. However, due to the nature of CVD process and powder form of the source material, there is a concentration gradient of $TaCl_5$ vapor along the CVD chamber as it is consumed in the above reaction (evident from EDX results –

support information). This consequently decreases the concentration of silicon reactive species along the CVD chamber decreasing the partial pressure of silica which play important roles in the formation different types of Ta_5Si_3 nanostructures.

To date, there have been several reports of synthesis of metal, metal silicides and metal oxide nanostructures such as networked nanowires, nanoribbons and nanosheets via metal chlorides using VS mechanism [2,4,23–26].

In these studies, two main processes have been proposed for the change from one dimensional to two dimensional growth and finally formation of networked nanostructures via VS mechanism. The first process is based on non-equilibrium kinetic growth caused by high supersaturation of reactive species such as oxygen and aluminum sub oxides, which may allow the formation of a low surface energy tip, favoring the 2D growth of the nanostructures [25,27]. In our study, however, in contrast to the Ye et al.'s [25] report, the 2D nanostructures are synthesized in regions with lower reactive species concentration and in higher surface energy directions.

The second growth mechanism is based on Zhang et al's [24,26] result on controlled growth of nanosheets via SiO_2 vapor pressure. They proposed partial coverage of low surface energy planes of nanocrystals by silica sheath. This sheath, induce a 2D growth of nanocrystals due to the positive feedback between the imbalance of silica coverage on different planes.

This growth process in the latter case closely corresponds to results observed in this study. Figure 4.4, shows a schematic diagram and corresponding SEM images indicating the growth mechanism of Ta_5Si_3 nanostructures. Based on this growth mechanism, in the initial stage of the synthesis process Ta_5Si_3 nanocrystals are formed via above reaction (Figure 4.4a). During the experiment Ta and Si species are deposited on various crystal planes of these nanocrystals. According to the Ta_5Si_3 (D8$_1$) unit cell illustrated in Figure 4.4a, these crystal structures have a Si only containing plane parallel to (001) crystal plane. During the CVD process and in the presence of silica vapor in the synthesis

chamber these planes provide a suitable surface for SiO_2 formation thus limiting the growth of Ta_5Si_3 nanocrystals in <001> direction. This is clearly shown in TEM observations (Figure 4.2). A closer look at crystal structure of Ta_5Si_3 unit cell (Figure 4.4) reveals the presence of other planes with high Si to Ta density which can present a suitable surface for SiO_2 formation, further limiting the growth of Ta_5Si_3 in these directions. The rate of deposition of silica vapor on these planes is directly related to the silica vapor pressure in the CVD chamber. In the initial region of the CVD chamber, the high concentration of $TaCl_5$ results in the increase in the partial pressure of silicon species (reaction 1), increasing the silica vapor pressure.
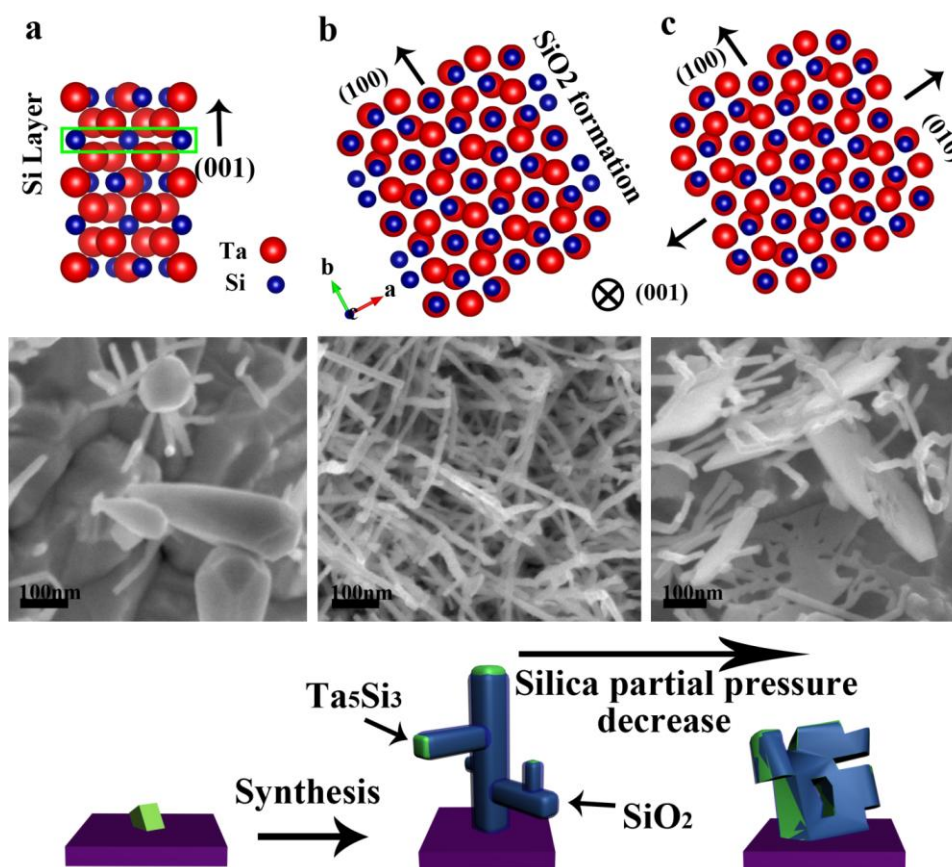
Figure 4.4 Schematic diagram of growth process of Ta_5Si_3 nanostructures with silica controlled morphologies. Ta_5Si_3 a) nanocrystals, b) Ta_5Si_3 NNWs, c) NNRs and NSs.

According to above growth mechanism, high silica vapor pressure enhances the silica coverage of planes parallel to (010) and (001) crystal planes on the nanocrystals, promoting the growth of Ta_5Si_3 networked nanowires shown in Figure 4.4b. However, with the decrease in concentration of $TaCl_5$ vapor along the downstream direction of CVD chamber due to reaction in the initial region (reaction 4.1), the silica vapor pressure decreases. This decrease enables the partial silica coverage of nanocrystals only on (001) planes (Figure 4.4c) which reach a critical point during the experiment causing an imbalance of silica coverage. This results in net mass diffusion of tantalum and silicon species onto {100} planes thereby nanoribbons and nanosheets are obtained.

Recent publications have reported the superior capacitance performance of silicide nanostructures [4]. Herein we have investigated the electrochemical capacitance behavior of the different Ta_5Si_3 nanostructures obtained in this work. Figure 4.5 shows the normalized cyclic voltammograms of the Ta_5Si_3 NNWs and NSs without any pre-treatment. By comparing the area under the curve of line a) and line b) in Figure 4.4, it is apparent that Ta_5Si_3 NSs show a higher capacitance than that of Ta_5Si_3 NNWs. This is in good agreement with previous reports [28,29] which correspond this increase to the higher surface area of nanosheets and their larger micropore area compared to networked nanowires. However, due to presence of SiO_2 shell layer, it is a challenge to calculate the exact capacity of the nanostructures in this stage. Further detailed studies will be needed in our future work.
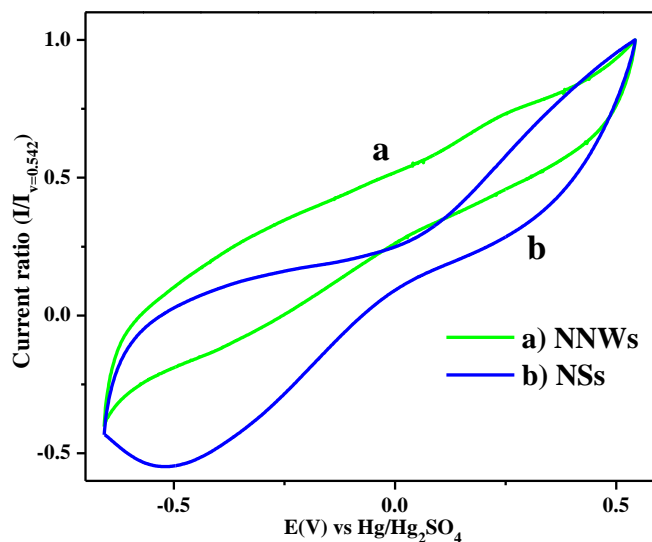
Figure 4.5 Cyclic voltammetry of the Ta₅Si₃ nanostructures (normalized to current at V=0.542 V). a)NNWs and b) NSs.

4.4   Conclusions

We have successfully synthesized single crystalline Ta₅Si₃ complex nanostructures with controlled morphology. The nanostructures were deposited on carbon microfibers via LPCVD using tantalum chloride precursor and silicon powder. It was found the morphology of these nanostructures is very sensitive to precursor and silica partial vapor pressure along the CVD chamber. The networked nanowires are grown in the high concentration region while the networked nanoribbons and nanosheets in lower concentration area. Furthermore experimental results reveal that the nanobats can be deposited on the substrate by introduction of a mixture of carbon gas and argon as carrier gas. We proposed a vapor solid mechanism based on the formation of silica sheath on {001} crystal planes of Ta₅Si₃ tetragonal nanostructures and their growth evolution with the growth time. Cyclic voltammetry measurements of different morphologies of Ta₅Si₃

nanostructures indicates that networked nanosheets exhibit a superior capacitance compared to other morphologies. The controlled synthesis of single crystalline 2D Ta_5Si_3 nanostructures as one of the highly stable silicides paves the road for new electronic and energy related applications.

Acknowledgements

4.5   References

[1]   Cui C, Zhang J, Liu L and Fu H 2010 Journal of Materials Science and Technology 26 65–68

[2]   Schmitt AL, Higgins JM, Szczech JR and Jin S 2010 Journal of Material Chemistry 20 223-235

[3]   Chou L-J, Chueh Y-L and Ko M-T 2007 Thin Solid Films 515 8109–8112

[4]   Zhang Y, Geng D, Liu H, Banis MN, Ionescu MI, Li R, Cai M and Sun X 2011 Journal of Physical Chemistry C 115 15885–15889

[5]   Chueh YL, Chou LJ, Cheng SL, Chen LJ, Tsai CJ, Hsu CM and Kung SC 2005 Applied Physics Letters 87 223113–223121

[6]   Reader AH, van Ommen AH, Weijs PJW, Wolters RAM and Oostra DJ 1993 Reports on Progress in Physics 56 1397–1467

[7]   Chirkin AD, Lavrenko VO and Talash VM 2009 Powder Metallurgy and Metal Ceramics 48 330–345

[8]   Gong QM Materials Research Bulletin 42 474–481

[9]   Cheb JL 2005 Journal of Minerals, Metals and Materials 57 24–30

[10]   Borghesi A, Nosenzo L, Piaggi A, Guizzetti G, Nobili C and Ottaviani G 1988 Physical Review B (Condensed Matter) 38 10937–10940

[11]   Amiotti M, Borghesi A, Marabelli F, Piaggi A, Guizzetti G and Nava F 1991 Applied Surface Science 53 230–236

[12]   Yu-Lun Chueh, Mong-Tzong Ko, Li-Jen Chou, Lih-Juann Chen, Cen-Shawn Wu and Chii-Dong Chen 2006 Nano Letters 6 1637–1644

[13]   Zhang S-L and Ostling M 2003 Critical Reviews in Solid State and Materials Sciences 28 1-129

[14]   Maszara WP 2005 Journal of the Electrochemical Society 152 550–555

[15]   Viennois R, Tao X, Jund P and Tedenac J-C 2011 Journal of Electronic Materials 40 597–600

[16]   Chen LJ, Wu W-W, Hsu HC, Chen SY, Chueh YL, Chou L-J, Lu KC and Tu KN 2007 Electrochemistry Society Transaction 11 3–6

[17]   Zhou S, Liu X, Lin Y and Wang D 2009 Chemistry of Materials 21 1023–1027

[18]   Kim T and Bird JP 2010 Applied Physics Letters 97 263111-263114

[19]   Zhang H-L 2008 Nanotechnology 19 1–7

[20]   Rao CN., Deepak F., Gundiah G and Govindaraj A January Progress in Solid State Chemistry 31 5–147

[21]   Williams DS, Coleman E and Brown JM 1986 Journal of Electrochemistry Society 133 2637–2644

[22]   Widmer AE and Fehlmann R 1986 Thin Solid Films 138 131–140

[23]   Zhou S 2008 Angewandte Chemie International Edition 47 7681–7684

[24]   Zhang H-X, Ge J-P, Wang J and Li Y-D 2006 Nanotechnology 17 253–261

[25]   Ye C, Fang X, Hao Y, Teng X and Zhang L 2005 Journal of Physical Chemistry B 109 19758–19765

[26]   Zhang H-X, Ge J-P and Li Y-D 2006 Journal of Physical Chemistry B 110 14107–14113

[27]   Zhang Y, Li R, Zhou X, Cai M and Sun X 2008 Journal of Nanomaterials 2008 1–8

[28]   Yang S-Y, Chang K-H, Tien H-W, Lee Y-F, Li S-M, Wang Y-S, Wang J-Y, Ma C-CM and Hu C-C 2011 Journal of Materials Chemistry 21 2374-2380

[29]   Xiong S, Yuan C, Zhang X, Xi B and Qian Y 2009 Chemistry – A European Journal 15 5320–5326

Chapter 5

5 TiSi$_2$O$_x$ coated N-doped Carbon Nanotubes for the Oxygen Reduction Reaction in Proton Exchange Membrane Fuel Cells (PEMFCs)[1,2]

Recently composite nanostructures have attracted considerable interest as catalyst supports, due to their multi-component structure and enriched function strengthening catalyst performance. These composite nanostructures enable the utilization of advantages of various materials as catalyst supports in PEMFCs. In our group we have developed carbon nanotubes and nitrogen doped carbon nanotubes as support for Pt catalyst in PEMFCs, enhancing the durability of the electrocatalysts. Furthermore, it has been shown that NCNTs can increase the electrocatalytic activity of Pt catalyst toward oxygen reduction reaction. Previous studies from others have also shown that TiO$_2$ and SiO$_2$ nanostructure as components of catalyst supports in PEMFCs electrocatalysts enhance the durability and catalytic activity of electrocatalysts.

In this chapter, authors propose a new 1D TiSi$_2$O$_x$-NCNTs composite nanostructure as catalyst support for PEMFCs. This novel nanostructure is prepared by sputtering TiSi$_2$ on NCNTs followed by heat treatments. Pt nanoparticles were deposited on these nanostructures using a wet chemical deposition method. Our results show that Pt/TiSi$_2$O$_x$-NCNTs and An-TiSi$_2$O$_x$-NCNTs exhibit a higher catalytic activity compared to

[1] Shuhui Sun[a], Xiangbo Meng[a], Yong Zhang[a], Ruying Li[a], Mei Cai[b] Tsun-Kong Sham[c] and Xueliang Sun[a]
a. Department of Mechanical and Materials Engineering, The University of Western Ontario, London, Ontario N6A 5B9 (Canada)
b. General Motors R&D Center, Warren, MI 48090-9055 (USA)
c.Department of Chemistry, University of Western Ontario, London, Ontario N6A 5B7 (Canada)
Email: xsun@eng.uwo.ca

commercial Pt/C catalysts. Detailed TEM and X-ray absorption spectroscopy analysis of Pt nanostructures deposited on these composite nanostructures revealed that morphology and electronic structure of the Pt nanostructures play an important role in the catalytic activity of electrocatalyst towards oxygen reduction reaction.

5.1   Introduction

Proton Exchange Membrane Fuel Cells (PEMFCs) is considered as one of the promising energy conversion systems, due to its low emission and high efficiency for automotive, portable and stationery applications. To succeed in large-scale commercialization, however, two major technical gaps - high cost, and low durability have to be addressed. The solutions to these challenges are associated with electrocatalyst and their support of PEMFCs. In the-state-of-the-art of PEMFCs, the most often used electrocatalysts are Pt-based nanoparticles supported by high surface area carbon material, accounting for 30-45% of the total cost [1]. Therefore, it is highly desirable to explore new methods to further enhance the catalytic activity of electrocatalyst with lower Pt content.

One of the main approaches is to develop new catalyst supports that help improve the catalytic activity of electrocatalysts such as Oxygen Reduction Reaction (ORR) activity at the cathode of the PEMFCs. In PEMFCs, this route plays a key role in enhancing the performance of fuel cells [2]. In recent years, intensive research has been focused on synthesizing various catalyst supports including nanostructured carbon material [3–7], metal oxides [8,9], carbides [10], and composite structures [11,12]. For example, carbon nanotubes (CNTs) and nitrogen doped carbon nanotubes (NCNTs) have been studied extensively due to their unique structures and excellent electrical properties. Many studies have shown that CNTs and NCNTs supported Pt catalysts [3,6] exhibit enhanced performance for ORR than commercial Pt/C. These studies suggested that the electrocatalytic activity of Pt clusters is boosted by the interaction between Pt and the doping atoms of a support (e.g., nitrogen), for the charge transfer between Pt and these atoms affects the catalytic activity. In addition, the use of CNTs and NCNTs increases the Pt dispersion, leading to higher Pt utilization [3,4]. In most cases, metal oxides and ceramic materials are electrochemically stable in fuel cell environment, and can act as co-catalysts through affecting the electronic structure of catalyst. Among metal oxides studied for catalyst supports in low temperature fuel cells, titanium oxides (TiO_2) was extensively studied in the form of micro/nano particles, nanotubes, and nanowires.

Studies have shown TiO_2 to be an interesting candidate support material since it has high stability in the fuel cell environment at potentials relevant to PEMFC cathode [11]. Kang et al. investigated ORR activity of PtCo on titanium oxide nanotube. Their results showed significant enhancement for ORR and methanol oxidation [13]. The drawback with ceramic material is their weak physical interaction with catalyst nanoparticles compared to carbon-based supports, leading to low dispersion of the catalysts and lower catalytic activity. Furthermore, the low electron conductivity of certain metal oxides (e.g., TiO_2 and SiO_2) remains as another issue at PEMFCs working temperatures.

To combine the advantages of both carbon and ceramic based supports for low temperature fuel cells, their composite materials were proposed as new supports [12]. Composite catalyst support material such as titanium oxide modified carbon nanostructures have been reported to improve the catalytic activity of the electrocatalyst. Beak et al [14] have shown that TiO_2 nanoparticles modified carbon support improved the dispersion of Pt nanoparticles. It was also found that the interaction between Pt and Ti species had an impact on the electronic state of Pt, contributing to the enhanced ORR activity of Pt. SiO_2 modified carbon nitride have also been studied by Wang et al [15], as electrocatalyst for ORR. They showed that Pt nanoparticles deposited on SiO_2 modified carbon nitride showed much higher mass activity compared to carbon and carbon nitride supports. This was attributed to the synergistic effect existing in Pt, carbon nitride and SiO_2.

To understand the effect of the catalyst supports on the activity of the electrocatalysts for ORR and to design more efficient systems, studies have been focused on several important factors. It has been shown that nitrogen content in NCNTs influences the ORR activity electrocatalysts [6,16]. Studies have shown strong metal support interaction (SMSI) between the catalyst supports and Pt nanoparticles plays a key part in the performance of the electrocatalyst [14]. X-ray absorption spectroscopy (XAS) of Pt $L_{2,3}$ and Pt $M_{2,3}$ edges of supported Pt nanoparticles provides a good means of probing the electronic structure of Pt nanoparticles and the effects of catalysts supports [17–19]. This

is directly related to the interaction between the catalysts and their supports of the electrocatalysts [17,18]. Furthermore it has been reported that the morphology and shape of Pt nanostructures influences the ORR activity of the electrocatalyst [20,21]. The Pt nanostructure morphology in turn is related to the deposition process and substrate.

Herein we report the synthesis of $TiSi_2O_x$-NCNTs hybrid composite via CVD and magnetron sputtering. The electrocatalytic properties of Pt catalyst supported on $TiSi_2O_x$-NCNTs and *An*-$TiSi_2O_x$-NCNTs (*An*: Annealed) for ORR in PEMFCs have been studied. To elucidate the influencing parameters on the ORR activity of the composite nanostructured electrocatalysts, the morphology, physical and chemical structure of the catalysts supports and Pt nanoparticles were studied. X-ray absorption spectroscopy was used to study the chemical state of Ti and Si atoms in $TiSi_2O_x$ sputtered and the effect of heat treatment on these coatings. The chemical and electronic structure of Pt nanostructures deposited on the composite catalyst supports were investigated by qualitative and quantitative analysis of x-ray absorption near edge structure spectra of the Pt $L_{2,3}$ edges.

5.2   Experimental Procedure

5.2.1 Synthesis

$TiSi_2O_x$-NCNTs nanostructures were synthesized by the combination of CVD process and magnetron sputtering. In this method, NCNTs were synthesized on carbon paper via CVD method using Fe as the catalyst and melamine ($C_3H_6N_6$, Aldrich, 99%) as the source of carbon and nitrogen [22–24]. In detail, an aluminum (Al) layer with a thickness of 30 nm was sputtered on a carbon paper as a buffer layer. On top of this layer, a 1-2 nm thick Fe layer was sputtered to act as the catalyst for NCNT growth. The substrate was placed in the center of a quartz tube. Melamine was put at the low temperature region of the quartz tube (upstream). The tube was mounted on a horizontal electric furnace and Ar (99.999%) was introduced into the system for 30 min to purge air out. The temperature

was raised to 800 °C, and held at this temperature for 30 min. During this period a constant flow of Ar (300 sccm) was maintained in the system. After cooling down the system to room temperature, the substrate was covered by a dark black layer of NCNTs.

The NCNTs on carbon paper were placed in a plasma enhanced chemical vapor deposition-sputtering system (PECVD). A 100 nm layer of $TiSi_2O_x$ was deposited on the NCNTs from a $TiSi_2$ target (Kurt J. Lesker, 2 inch, 99.9%) using a RF magnetron (150 W, 10 min) at a chamber pressure of 2 x 10^{-1}Pa. The oxygen was introduced into the layer from the residual oxygen in the sputtering chamber.

The composite nanostructures were then heat treated, resulting in *An*-$TiSi_2O_x$-NCNTs for further studies. The heat treatment of the nanostructures was carried out in a vacuum oven system. The nanostructures were positioned in a quartz tube and placed on a horizontal electric furnace. The pressure of the system was lowered to around 1mbar and Ar was introduced at a high flow rate into the system to flush out the air. This process was repeated several times. The system was heated up to 1000°C at the rate of 10 °C/min and kept at this temperature for 6 hrs. During this period the pressure of the system was maintained at 500 Pa by introducing Ar (99.999%). After heat treatment, the color of the samples turned from dark black to dark gray.

5.2.2 Characterization

The morphologies of the products were characterized using field emission scanning electron microscope (SEM, Hitachi S4800, operated at 5.0 kV) equipped with energy dispersive X-ray spectroscopy (EDX), transmission electron microscope (TEM, Hitachi 7000, operated at 100 kV), and high resolution TEM (HRTEM, JEOL 2010, operated at 200 kV) along with selected area electron diffraction (SAED) pattern. The crystal structure and composition of the products were characterized by X-ray diffractometer (XRD) using Co Kα1 (λ = 0.179 nm) radiation operated at 45 kV and 35 mA. Raman

spectroscopy (HORIBA Scientific LabRAM HR) was carried out to provide detailed information on the composite structures.

5.2.3 Pt deposition

Pt nanoparticles were deposited on $TiSi_2O_x$-NCNT composite nanostructures by a formic acid method [25,26]. In this method, the Pt precursor ($H_2PtCl_6.6H_2O$, Aldrich, 99.95%) and formic acid (HCOOH, Aldrich, 98%) were used as received. The synthesis was conducted in an environmental friendly solution of deionized water. The reduction process is given by
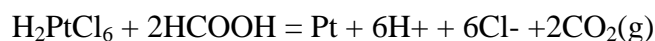
$$H_2PtCl_6 + 2HCOOH = Pt + 6H+ + 6Cl- +2CO_2(g)$$

In this process, 1 ml of 0.03 M $H_2PtCl_6.6H_2O$ and 1 ml HCOOH were simultaneously mixed with 20 ml of water at room temperature. $TiSi_2O_x$-NCNT nanostructures on carbon paper were immersed in the solution and the reaction was carried out in 80^oC for ~ 15 min. In this period the color of the solution turned from golden orange to dark brown, indicating the formation of Pt nanoparticles. After the solution was cooled down, the composite nanostructures on carbon paper was removed from the solution, washed by deionized water and dried at room temperature overnight.

5.2.4 Electrochemical Characterization

Cyclic voltammetry was conducted at room temperature using an Autolab potentiostat/galvanostat (Model, PGSTAT-30, Ecochemie, Brinkman Instrument) with a standard three-electrode, two-compartment configuration. Pt wire and Ag/AgCl (3M NaCl) electrode were used as the counter and reference electrodes, respectively. For hydrogen electrosorption curves measurement, the potential was cycled between -0.159 V and 0.991 V at 50 mVs^{-1} to obtain the voltammograms of hydrogen adsorption in Ar-purged 0.5M H_2SO_4 aqueous solution. For ORR measurement, O_2 (99.99%) was first

purged into solution at a position close to the working electrode for at least 30 min. The measurements were done by linear potential sweeping from 0.8 V to 0.2 V.

For comparison purposes, Pt nanoparticles deposited (same synthetic method as above) on pristine NCNTs were also evaluated.

5.2.5 X-ray Absorption Spectroscopy

The Si K edge and Ti K edge x-ray absorption near edge structure (XANES) measurements were obtained using the soft x-ray microcharacterization beamline (SXRMB; 06B1-1) at the Canadian Light Source (CLS). The Si K edge spectra were collected using an InSb(111) crystal monochrometer and the Ti K edge spectra were collected using a Si (111) crystal monochrometer in total electron yield (TEY). The spectra were calibrated using a Si and a Ti reference sample.

XANES measurements of Pt L_2 edge and Pt L_3 edge were conducted at the PNC-XSD (Pacific Northwest Consortium X-ray Science Division) ID-20B beamline of the Advanced Photon Source (APS) at Argonne National Laboratory. The spectra were collected in fluorescence yield using a solid state detector and the spectra of high purity metal Pt foil were collected in transmission mode for comparison and mono energy calibration.

5.3   Results & Discussion

The morphologies of NCNTs, $TiSi_2O_x$-NCNTs and *An*-$TiSi_2O_x$-NCNTs are shown in Figure 5.1. The NCNTs used as the substrates for the composite support define the ultimate morphology of the composite and are a key factor in determining the uniformity of the coated layer. In the CVD method, a thin Fe catalyst layer ensures a good control on the diameter and density of the synthesized NCNTs, as shown in Figures 3.1a and b

[22,27,28]. The NCNTs, as previously reported [22,29], exhibit typical bamboo-like structures and have a narrow range of diameter between 25 to 50 nm. Furthermore, the unique texture of carbon paper used as substrate enhances the formation of 3D open structure of NCNTs with no preferential alignment [24,30].

SEM images of $TiSi_2O_x$-NCNTs are shown in Figure 5.1c and d. As seen in these figures, the general morphology of nanostructures on carbon paper is not affected in the sputter coating process and the $TiSi_2O_x$-NCNTs maintain their 3D open structure. However, it is evident in SEM images (Figure 5.1d) that there is an increase in the diameter of nanostructures, indicating the successful deposition of $TiSi_2O_x$ layer on NCNTs. The thickness of the $TiSi_2O_x$ coating on NCNTs was controlled by sputtering power and time. The EDX analysis of these nanostructures (inset of Figure 5.1c) confirms the presence of Ti and Si with an approximate atomic ratio of 1:2. The oxygen was introduced into the deposited layer as shown in the EDX spectrum through the residual oxygen in the chamber suggested in previous reports [31–33]. A closer observation of the composite nanostructures (Figure 5.1d) shows that the $TiSi_2O_x$ coating has particle-like morphology, which is common during sputtering on nanostructured materials at room temperature [34,35].

 To study the effect of crystallinity of coated layer, $TiSi_2O_x$-NCNTs were treated at high temperature (1000^oC). The morphology of the annealed $TiSi_2O_x$-NCNTs at 1000^oC for 6h (*An*-$TiSi_2O_x$-NCNTs) is depicted in Figures 3.1e and f. The annealed nanostructures have a similar structure to pristine composite nanostructures but smoother surfaces. In addition, as indicated in Figure 5.1f, in some areas there is evidence of layer diffusion forming network structures. EDX analysis (inset of Figure 5.1f) of *An*-$TiSi_2O_x$-NCNTs indicates no significant change in the ratio of elements present in the coated layer. XRD analysis did not show any crystalline peaks corresponding to these nanostructures.
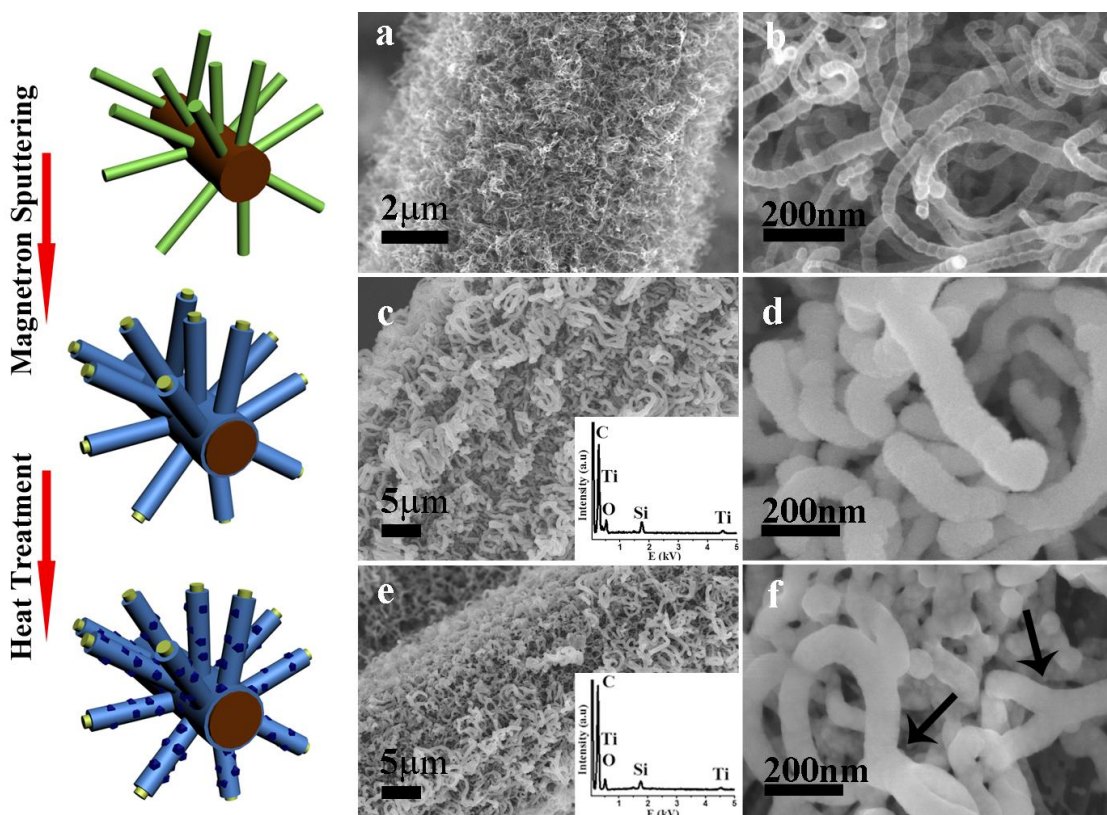
Figure 5.1 Schematic diagram and SEM images of nanostructures deposited on carbon paper. a, b) NCNTs. c, d) TiSi$_2$O$_x$ -NCNT. e, f) *An*-TiSi$_2$O$_x$ -NCNT.

TEM observations further reveal the unique morphology of these nanostructures. As shown in Figure 5.2a, the NCNTs have uniform diameters with nearly constant spaced bamboo-like structures. HRTEM image (Figure 5.2b) reveals that the NCNTs have high degree of crystallinity in spite of the distorted nanotube walls resulting from the regular joint defects, as explained by Liu et al.[22]. Figure 5.2c shows TEM image of TiSi$_2$O$_x$-NCNTs, revealing the non-uniform coverage of TiSi$_2$O$_x$ layer on NCNTs. These observations indicate that the thickness of the TiSi$_2$O$_x$ coating on NCNTs varies from 0 to 60 nm due to the shielding effect of sputtering technique. The thickness depends on the orientation of NCNTs with respect to the sputtering target. There have been similar studies on the formation of such nanostructures using sputtering on small and localized carbon nanotubes [34–36]. In these studies, sputtering was conducted on single or few

carbon nanotubes resulting in a better coverage of the coated area. HRTEM image of TiSi$_2$O$_x$ -NCNT composite nanostructures (Figure 5.2d), illustrates their amorphous nature. The SAED pattern shows diffused rings (inset of Figure 5.2d) further confirming their amorphous nature [31].
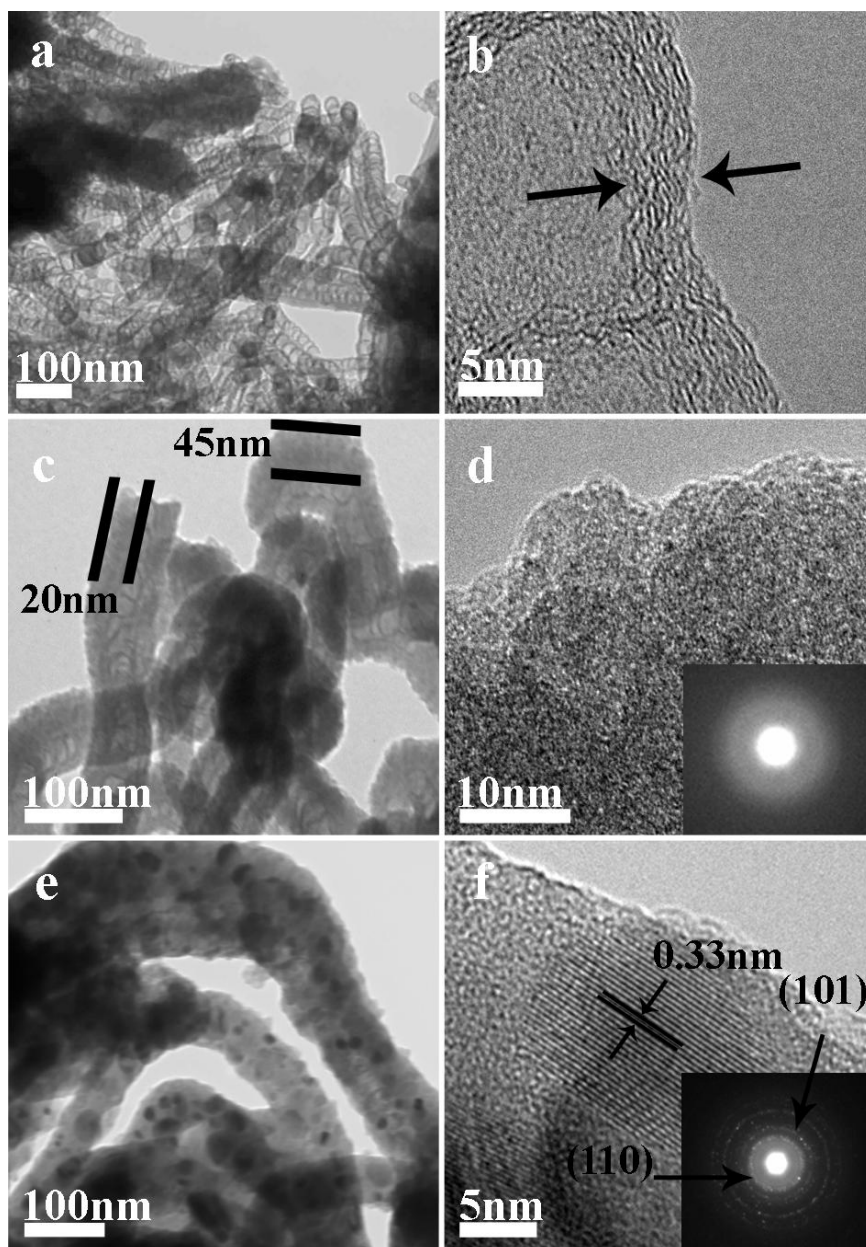
Figure 5.2 TEM and HRTEM images of composite nanostructures. a,b) NCNTs, c,d) TiSi$_2$O$_x$ -NCNT and e,f) *An*-TiSi$_2$O$_x$-NCNT.

Compared to $TiSi_2O_x$-NCNTs, the TEM images of *An*-$TiSi_2O_x$-NCNTs (Figure 5.2e) indicate the enhanced coverage of $TiSi_2O_x$ on NCNTs, confirming the diffusion of the coated layer under heat treatment. Furthermore, TEM images reveal the formation of nanoparticles in high density in the amorphous coating on NCNTs. HRTEM images of these nanoparticles shown in Figure 5.2f, reveal that these nanoparticles are single crystalline with diameters between 5 to 10nm and are partially covered by the amorphous layer. The lattice spacing of the nanoparticles is around 0.33nm, corresponding to the {110} planes of rutile TiO_2. The SAED pattern (inset of Figure 5.3f) can be indexed as tetragonal structure of rutile TiO_2. This is consistent with the results reported by Sankur et al. [37] and Goldstein et al. [38]. Sankur et al. [37] reported the formation rutile TiO_2 through annealing a co-sputtered TiO_2-SiO_2 thin film at 1000^oC. They show that the growth of TiO_2 crystalline particles in the amorphous matrix is diffusion-limited and decreases with decreasing TiO_2 content. There also have been several reports on the formation of various nanocrystals such as Si [39] and metal silicides [31,32,40,41] in an amorphous matrix. Since these types of reactions are diffusion-controlled process, in order to obtain higher degree of crystallinity, longer annealing time and higher temperature are required.

The chemical states of $TiSi_2O_x$ coating of the composite nanostructures were further studied using XAS. Figure 5.3a show the Si K-edge (TEY) XANES of the $TiSi_2O_x$ samples. The XANES of a clean amorphous SiO_2 is also shown for comparison. According to figure 5.3a, Si K edge XANES of both $TiSi_2O_x$-NCNTs and An-$TiSi_2O_x$-NCNTs exhibit features that are characteristic of SiO_2 at 1847 eV. In addition to the sharp SiO_2 resonance the coated samples show a small feature at 1845 eV which is enhanced in $TiSi_2O_x$-NCNTs samples compared to annealed specimens. This feature is attributed to the 1s-σ^* resonance of the Si-O bond in the presence of silicon suboxides [42]. The reduction of intensity of this feature in *An*-$TiSi_2O_x$-NCNTs samples is due to oxidation of the suboxides during the annealing process and formation of highly crystalline SiO_2 as judged by the sharpness of the resonance.

Figure 5.3b shows the Ti K-edge XANES spectrum of the composite nanostructures and TiO$_2$ (rutile) powder as a reference sample. The characteristic feature of the Ti K-edge spectra is the pre-edge weak features and the edge resonance arising from the excitation of a 1s electron into an empty bound state derived from the d and p states of Ti respectively [43,44]. These pre-edge features probe the local symmetry of the Ti t$_{2g}$ and E$_g$ orbitals and their behavior upon local distortion [45]. The post edge features are mainly due to the multiple scattering contribution of the ejected photoelectron from higher shell neighboring atoms [44]. A number of studies have used the pre edge intensity of Ti K-edge along with their positions to derive information from the Ti coordination chemistry, in compounds such as titanosilicate glass [43,46,47]. Shuji et al. [47], have reported that the pre edge features of Ti K edge XANES provide the Ti coordination number based on the plot of peak energy versus peak high. They estimated the distortion using the intensity ratio between pre-edge peaks and Ti-Ti interaction strength from the rise and fall in peak intensity in the whole pre edge region.

The XANES features of TiSi$_2$O$_x$-NCNTs shown in figure 5.3b reveal a high intensity pre edge peak with two small broad peaks on either side and a broad region with no distinct peaks in the multiple scattering regions. The broad peak in the multiple scattering regions can be attributed to the absence of medium to long range order around the Ti atoms in the amorphous layer confirming the HRTEM analysis of these samples. The distortion in the structure surrounding the Ti atoms in the short range, based on Shuji et al.[47] results can further be confirmed by the features seen in the pre edge region of TiSi$_2$O$_x$-NCNT samples, where the Ti is not is a well-defined symmetry environment on average

However, the XANES features of *An*-TiSi$_2$O$_x$-NCNTs closely resembles that of the TiO$_2$ (rutile) and the pre-edge region of these composite structures has similar peak position and intensity, indicating the coordination chemistry of Ti in *An*-TiSi$_2$O$_x$-NCNTs is same as rutile TiO$_2$, a D4h symmetry This is also consistent with the HRTEM results of TiO$_2$ nanoparticle formation entailed by annealing. The small differences in the peak intensity in the pre edge region and the multiple scattering area can be attributed to the size effect,

as the same trend was reported by Wu et al through comparing bulk and nanostructured TiO$_2$ [44].
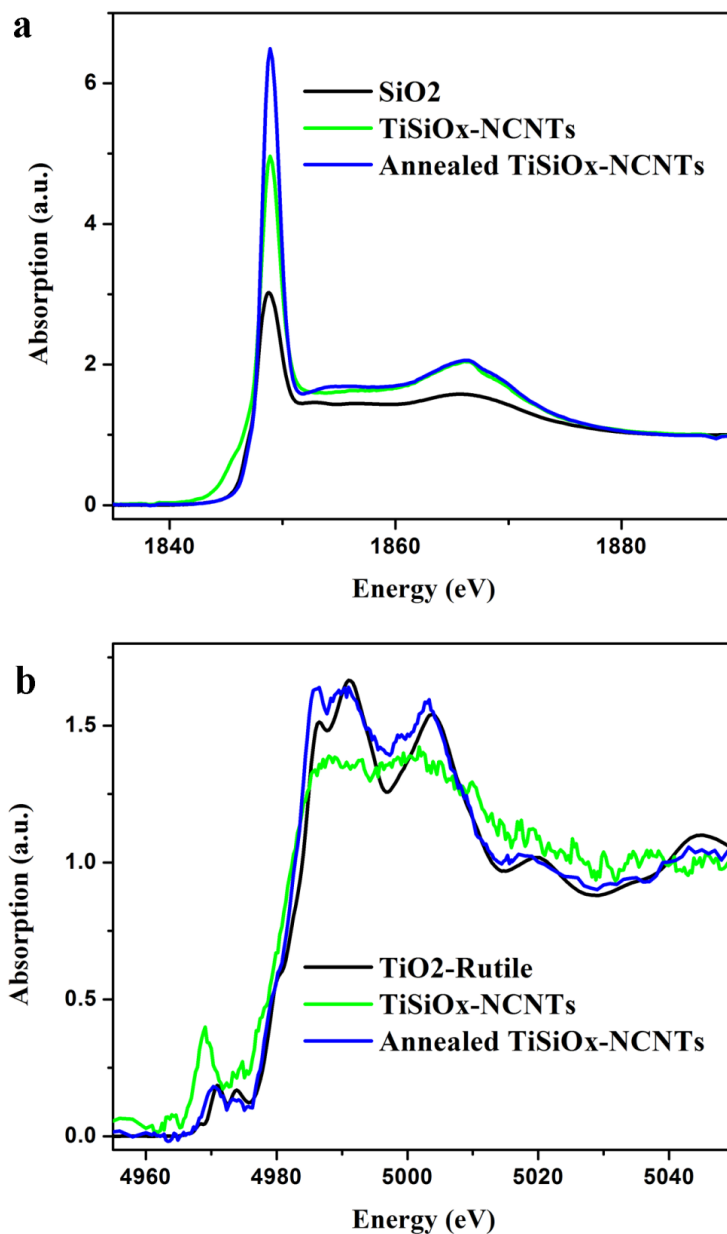
Figure 5.3 Normalized XANES spectra of composite catalysts supports at a) Si K-edge and Ti K-edge.

To test the performance of TiSi$_2$O$_x$-NCNTs composite nanostructures as catalyst support for PEMFCs, Pt nanoparticles were deposited on these nanostructures. Cyclic voltammetry (CV) measurements were carried out to study the electrochemical properties of Pt/TiSi$_2$O$_x$-NCNT and Pt/*An*-TiSi$_2$O$_x$-NCNT composites. For comparison, Pt/NCNTs samples were examined under identical conditions. The CVs (Figure 5.4a) of these composite nanostructures were recorded in Ar-saturated 0.5 M H$_2$SO$_4$ aqueous solution at room temperature between -0.159 and 0.991 V vs Ag/AgCl (3M NaCl), with a scan rate of 50 mVs^{-1}. The voltammetric features of all the electrodes reveal the typical characteristics of Pt metal, with the adsorption and deposition of hydrogen between -0.154 to 0.1 V and Pt oxide formation and it reduction between 0.5 to 0.991 V. However, a closer observation on the reduction peak potential of Pt oxide of these three samples reveals that Pt/*An*-TiSi$_2$O$_x$-NCNTs shows a positive shift compared to other samples. Previous studies demonstrated a correlation between the oxide reduction peak potential and the particle size [48–50]. Millared et al. [49,50], showed that the potential of the oxide reduction peak is strongly influenced by the particle size, with larger particles showing higher potentials. In addition, this shift in Pt oxide reduction peak is visible between Pt nanowires and Pt nanoparticles with similar diameters [21,51,52]. Although the origin of this particle size effect still remains unclear, this shift observed in CV can be correlated to the difference in the morphology of Pt nanoparticles on the composite nanostructures.

The electrochemical surface area (ECSA) of the electrodes can be estimated from CV curves. The total charges of hydrogen desorption (Q$_H$) on the electrodes is calculated by integrating desorption peaks after excluding the double layer charging effect. Using Q$_H$ value and the Pt loading, it is possible to calculate the active Pt surface area (S$_{EL}$) according to the following formula.

$$S_{EL} = \frac{Q_H}{Q_{ref} \times Pt\ loading}$$

S_{EL} is expressed in cm^2mg^{-1} where Pt loading is in $mg_{pt}cm^{-2}$ and $Q_{ref} = 0.21$ $mCcm^{-2}$. This value corresponds to a surface density of 1.3 x 1015 atom cm^{-2} (a generally accepted value for a polycrystalline Pt electrode). Values of $S_{EL} = 288.6$ and 255.9 cm^2mg^{-1} have been obtained for Pt nanoparticles deposited NCNTs, $TiSi_2O_x$-NCNTs, respectively, while $S_{EL} = 179.6$ cm^2mg^{-1} has been calculated for Pt nanostructures deposited on *An*-$TiSi_2O_x$-NCNTs. This can be attributed to the intrinsic 1D morphology of Pt nanostructures compared to Pt nanoparticles deposited on composite nanostructures. This is in good agreement with previous results reported on Pt nanowires [21,51,52].

The electrocatalytic activities for ORR of the composite electrodes are compared in Figure 5.4b, by linear scanning voltammetry at a scan rate of $50mVs^{-1}$. Pt/*An*-$TiSi_2O_x$-NCNTs shows a higher peak potential than other two electrodes. The peak potential of Pt/*An*-$TiSi_2O_x$-NCNTs is 0.47 V while that of Pt/NCNTs and Pt/$TiSi_2O_x$-NCNTs are both at 0.44V, suggesting that Pt/*An*-$TiSi_2O_x$ exhibits a 30 mV positive shift of the peak potential compared to the latter two electrodes toward ORR. At peak potential, the mass activity on Pt/*An*-$TiSi_2O_x$-NCNTs (28.3 Ag^{-1}) is about 1.1 times higher than Pt/NCNTs (26.1 Ag^{-1}) and 1.02 times higher than Pt/$TiSi_2O_x$-NCNTs (27.7 Ag^{-1}). This improvement occurred in spite of a 50% lower Pt active surface area for the Pt/*An*-$TiSi_2O_x$-NCNTs compared to Pt/NCNTs. By taking into account the active surface area, specific ORR activity for Pt/*An*-$TiSi_2O_x$-NCNTs (1.54 Am^{-2}) is 1.7 times larger than Pt/NCNTs (0.9 Am^{-2}) and 1.4 times larger than Pt/$TiSi_2O_x$-NCNTs (1.08 Am^{-2}). The large specific activity and mass activity and more positive peak potential indicate that Pt/*An*-$TiSi_2O_x$-NCNTs has a higher intrinsic electrocatalytic activity than Pt/$TiSi_2O_x$-NCNTs which itself is higher than Pt/NCNTs.
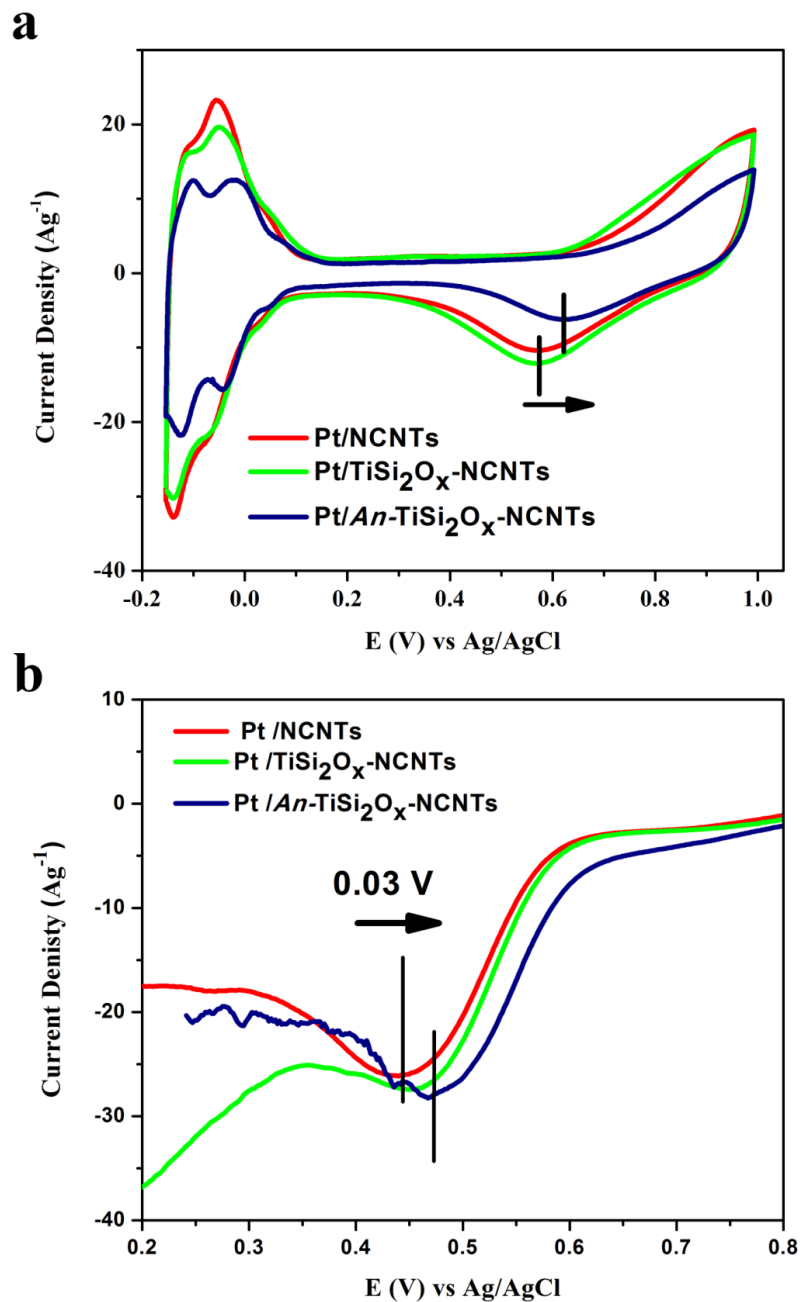
Figure 5.4 Electrochemical characterization of composite nanostructures. a) Cyclic voltammetry curves of Pt deposited composite nanostructures, b) Oxygen reduction curves of Pt deposited composite nanostructures. All samples were compared to Pt deposited nitrogen doped carbon nanotubes.

To elucidate the effect of composite supports on the activity of electrocatalysts towards ORR, the chemical, electronic structure and morphology of the Pt nanostructures on the composite supports were studied.

XANES at the Pt L_3 and L_2 edges for the Pt nanoparticles deposited on the composite structures are shown in Figure 5.5 including a Pt foil and Pt/NCNTs for comparison. It is seen that both Pt L_3 and L_2 edge XANES of supported Pt nanoparticles exhibit a considerably more intense whiteline (WL) compared to the Pt foil. The WL in Pt L_2 and L_3 edges arises from the dominant $2p_{1/2}$ and $2p_{3/2}$ transition to $5d_{3/2}$ and $5d_{5/2,3/2}$ respectively (dipole selection rule: $\Delta l = \pm 1$, $\Delta j = \pm 1, 0$) indicating the presence of unoccupied densities of states of Pt $5d_{5/2}$ and $5d_{3/2}$ characters in the samples [53,54]. The catalytic activity of Pt for various electrochemical reactions including ORR have been related to the densities of state of employed Pt [55–57]. Furthermore the interaction between the catalyst support and catalyst has been evaluated through study of XANES spectrum [17–19]. The qualitative and quantitative interpretation of Pt L_2 and L_3 edge WL and XANES has been widely used to probe the unoccupied density of d states in a variety of systems [53,54,58].

A close examination of the L_3 edge WL profile of the composite samples indicates that, there are small differences in the L_3 edge WL intensity and shape. Results indicate that the L_3 edge WL intensity increases in the following order: Pt foil < Pt/NCNTs Pt/TiSi$_2$O$_x$-NCNTs ~ Pt/*An*-TiSi$_2$O$_x$-NCNTs which is consistent with the ORR results of these electrocatalysts. All composite samples show a positive shift in the maximum energy (E$_{peak}$) with small negative shift in the threshold energy (E$_o$) (within experimental uncertainty). This indicates the Pt nanoparticles deposited on the composite supports are still metallic (a change in oxidation state to the common Pt (II) for example will induce a significant shift and the increase in the WL intensity compared to Pt foil is due to decrease in the number of electrons in the d orbital, confirming a strong interaction between Pt nanoparticles and their support in the direction that Pt's d charge is depleted.

The metallic behavior of these nanoparticles is also confirmed by the oscillations beyond the WL, which are characteristic of the FCC structure of Pt metal.
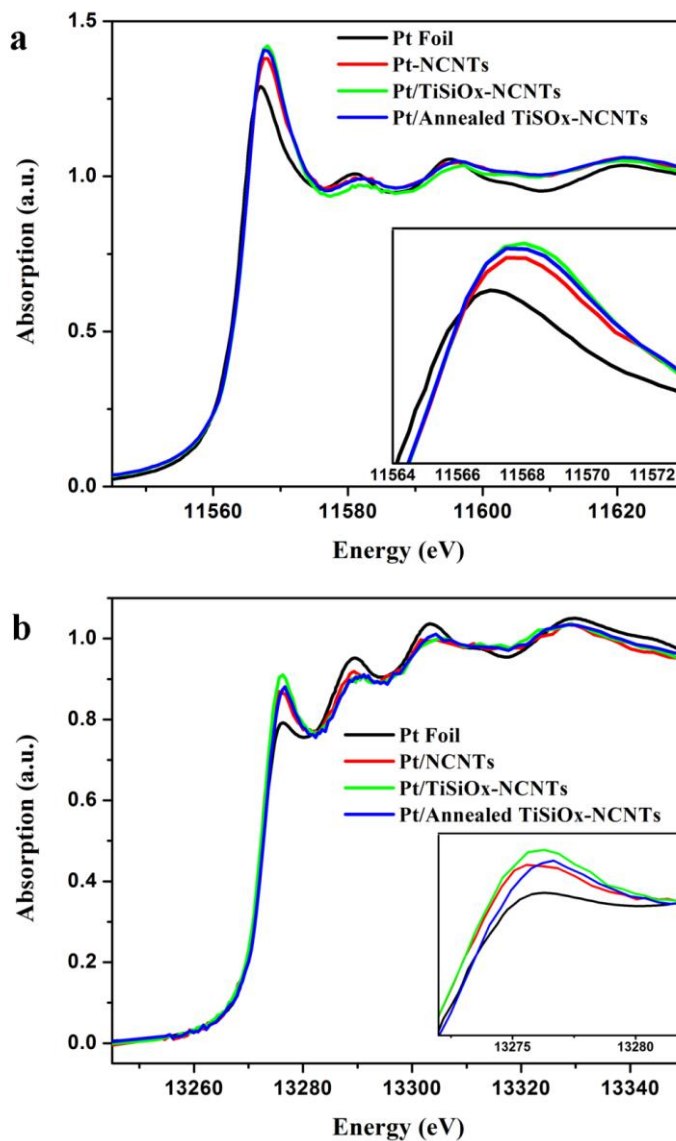
Figure 5.5 Normalized XANES spectra of Pt nanoparticles on composite catalyst support at a) Pt L$_3$ edge and b) Pt L$_2$ edge.

The corresponding L$_2$ edge WL (Figure 5.5b), shows a similar trend as that of Pt L$_3$ edge in E$_{peak}$ and E$_o$. However as seen in inset of Figure 5.5b, unlike the trend seen in Pt L$_3$

edge, the L_2 WL intensity of Pt/TiSi$_2$O$_x$-NCNTs is higher than that of Pt/*An*-TiSi$_2$O$_x$-NCNTs which may be due to different chemical sensitivity of 5d$_{5/2}$ and 5d$_{3/2}$ states in Pt d orbitals [58].

For a better understanding of the effect of the unoccupied densities of 5d states of Pt nanoparticles on different supports, quantitative WL intensity analysis has been conducted based on the method reported by Mansour et al.[58] and Sham et al. [54]. In this method, the Pt L_3 edge WL intensity is obtained by subtracting the Pt L_3 edge XANES from the corresponding XANES of Au. The area under the difference curve was integrated and ΔA_3 and ΔA_2 were calculated. These values can be expressed as:

$$\Delta A_3 = \int \mu(Pt)_{L_3WL} - \mu(Au)_{L_3WL}$$

$$\Delta A_2 = \int \mu(Pt)_{L_2WL} - \mu(Au)_{L_2WL}$$

and according to Sham et al. [54] the theoretical expression of these value are:

$$\Delta A_3 = C_o N_o E_3 \left(R_d^{2P_{3/2}}\right)^2 \left[\frac{6h_{5/2} + h_{3/2}}{15}\right]$$

$$\Delta A_2 = C_o N_o E_2 \left(R_d^{2P_{1/2}}\right)^2 (\tfrac{1}{3} h_{3/2})$$

where $C_o = 4\pi r^2 \alpha/3$ (α is the fine structure constant), N_0 the density of Pt atoms, h_j the 5d hole counts and E_2 and E_3 are the corresponding edge threshold, E_o for the L_2 and L_3 edges respectively. R term is the radial transition matrix element. By assuming R terms are similar for both edges:

$$C = C_o N_o R^2$$

and with this approximation:

$$h_{5/2} = \frac{1}{2C}\left[5\frac{E_2}{E_3}\Delta A_3 - \Delta A_2 \right]$$

$$h_{3/2} = \left[\frac{3\Delta A_2}{C} \right]$$

A C value of 7.484×10^4 cm^{-1} was derived for Pt metal by Matthesis et al.[59]. Table 5.1 summarizes the Pt L_3 and Pt L_2 edge threshold and WL parameters. These results quantitatively confirm the observations made on the Pt L_3 edge XANES, i.e., Pt/An-TiSi$_2$O$_x$-NCNTs and Pt/TiSi$_2$O$_x$ have the highest total unoccupied density of states of Pt 5d character compared to Pt/NCNTs indicating a higher SMSI between the composite supports and Pt catalysts. It can be concluded that this factor is one of the sources of catalytic activity enhancement of Pt/An-TiSi$_2$O$_x$-NCNTs and Pt/TiSi$_2$O$_x$-NCNTs compared to Pt/NCNTs.

Table 5.1 Pt L$_3$ edge and Pt L$_2$ edge whiteline parameters

Sample	Pt L$_3$ edge WL				Pt L$_2$ edge WL					
	E$_o$(eV)	E$_{Peak}$(eV)	Γ(eV)	ΔA_3	E$_o$(eV)	E$_{Peak}$(eV)	Γ(eV)	ΔA_2	h$_{5/2}$	h$_{3/2}$
Pt Foil	11564.00	11567.00	6.00	4.87	13273.00	13276.30	6.60	2.26	0.47	0.11
Pt/NCNTs	11563.98	11567.50	7.04	5.04	13272.98	13275.58	5.19	2.41	0.48	0.11
Pt/TiSiOx-NCNTs	11563.94	11568.06	8.23	5.10	13272.98	13276.38	6.81	3.15	0.49	0.15
Pt/An-TiSiOx-NCNTs	11563.98	11567.50	7.04	5.32	13273.00	13276.28	6.56	2.57	0.51	0.12

XANES studies of Pt catalysts provide detailed information on the electronic structure and chemical environment of Pt nanostructures; however they provide little information on the morphology, shape of the nanostructures. For this purpose, HRTEM analyses of Pt/composite supports were conducted.

The TEM observation Pt/TiSi$_2$O$_x$-NCNTs samples (Figure 5.6a and b) indicate Pt nanoparticles are mainly deposited on the bare surface of NCNT in contact with the TiSi$_2$O$_x$ coating. These Pt nanoparticles have similar morphology to Pt deposited on NCNTs [25] with uniform diameters of 3nm.

The non-uniformity of Pt nanoparticle deposition in the composite can be attributed to the presence of SiO_x on the surface of $TiSi_2O_x$ coating. Studies have shown that Pt deposition on SiO_2 containing surfaces using conventional methods leads to limited uniformity and small Pt loading. This is because the Pt deposition using reduction process requires a strong interaction between the Pt precursor and the substrate. When using H_2PtCl_6 as Pt precursor in an acidic environment (even as low as pH=1) the loading of Pt is reduced greatly since there is no strong interaction between $PtCl^-_6$ and SiO_2 surfaces.
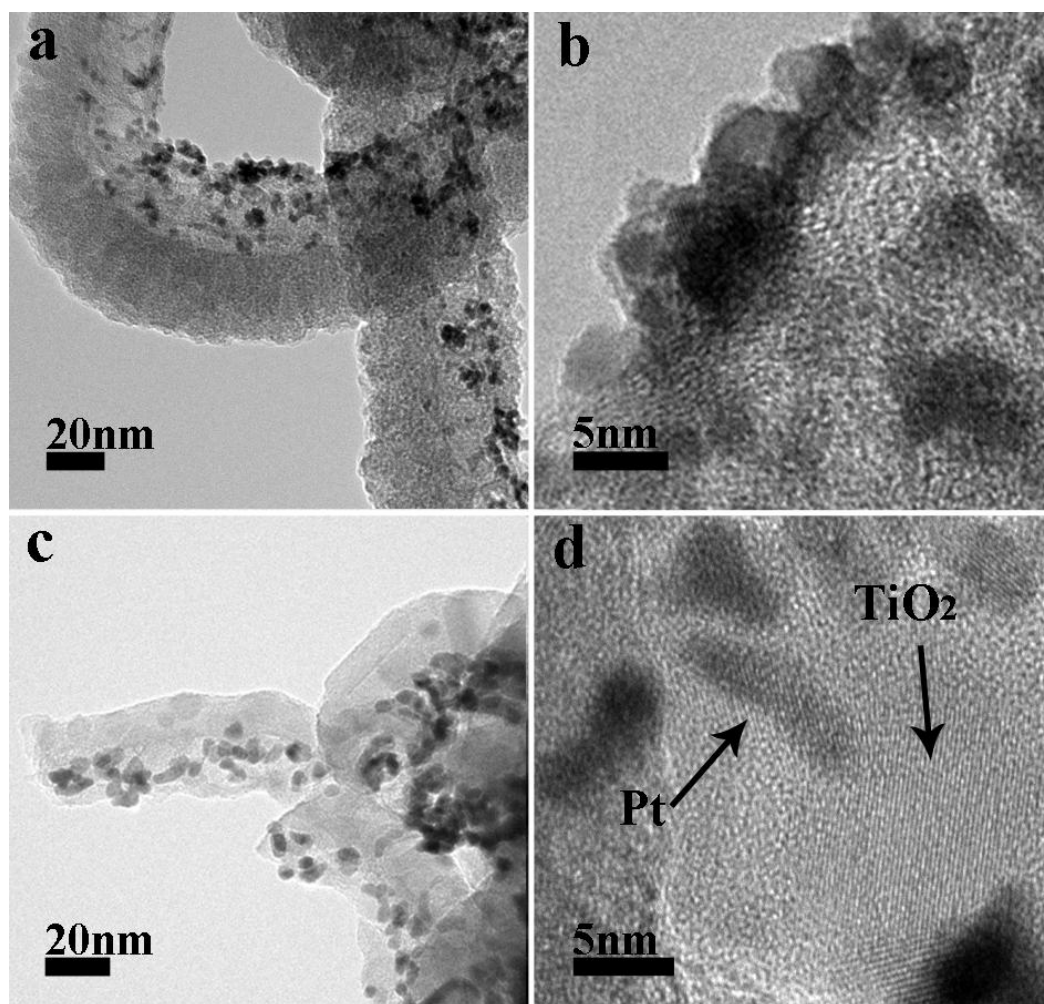
Figure 5.6 TEM images of Pt deposited nanostructures, a, b) $TiSi_2O_x$-NCNT; c, d) An-$TiSi_2O_x$-NCNT, grown on carbon paper.

 TEM images of Pt/*An*-TiSi$_2$O$_x$-NCNTs shown in Figure 5.6c reveal preferential deposition of Pt nanoparticles on the composite nanostructures which is similar to Pt/TiSi$_2$O$_x$-NCNTs. However as shown in HRTEM image of Pt/*An*-TiSi$_2$O$_x$-NCNTs there are some Pt nanoparticles deposited on the *An*-TiSi$_2$O$_x$ layer as shown in Figure 5.6d. These Pt nanoparticles are generally deposited in close proximity of the nanocrystals formed on the surface coated layer. Furthermore, HRTEM images reveal, in contrast to the untreated composite samples, the Pt nanoparticles deposited on *An*-TiSi$_2$O$_x$-NCNTs are not spherical and have an aspect ratio of 1 to 2.5 with small diameter of 3 to 4nm. Sun et al. [21,51,52,60] have reported the synthesis of Pt nanorods and nanowires on various nanostructured supports by the reduction of Pt salt via formic acid at room temperature. Their studies showed the formation of nanorod like Pt structures similar to those observed in Figures 3.6c and d. It is possible then, after annealing, the surface conditions of NCNTs promote the formation of rod-like Pt nanostructures under higher temperature within a short time.

A careful study of the XANES spectrum of Ti K-edge and Si K-edge of the Pt deposited composite supports did not reveal any significant changes compared to pristine composite supports. Therefore, to investigate the effects of TiSi$_2$Ox coating and the heat treatment on the structure of composite structures on the NCNTs, the nanostructures were characterized by means of Raman spectroscopy. Raman spectra of the three samples are plotted in Figure 5.7. In all of these three spectra, two prominent peaks at ~ 1350 cm^{-1} and ~ 1585cm^{-1} known as D band and G band, respectively, are observed. The I$_D$/I$_G$ ratios of the three samples measured in Figure 5.7 indicate that there is no considerable change, accounting for around 0.9 in all the three cases. This can be attributed to the relative lower annealing temperature (1000 $^{\circ}$C) compared to the graphitization temperature of carbon (normally above 1500 $^{\circ}$C) [61,62]. However, the comparison of FWHM of the D and G bands shows a considerable decrease in *An*-TiSi$_2$Ox-NCNT sample relative to NCNTs, indicating a change in the structure of composites. Furthermore the Raman spectrum of *An*-TiSi$_2$O$_x$-NCNTs shows well distinct peaks in the range of 2500 to 3000 cm^{-1}. The most prominent peak in this region corresponds to a second order Raman peak,

G' located at ~ 2700 cm^{-1}. Although the G' band is independent of the structural defects, studies have shown that the intensity, shape and position of this peak are sensitive to nitrogen incorporation in CNTs [63]. It has been reported that the intensity of G' band has inverse relation with the nitrogen content of CNTs. In addition, previous studies have shown that by annealing NCNTs at high temperatures (~1000°C), the nitrogen content decreases dramatically due to release of trapped N_2 molecules and depletion of pyridine like structures [64]. In this study, the appearance G' band is an indicative change of the nitrogen content and the structure of N-CNTs in annealed TiSi$_x$-NCNTs. This reduction in nitrogen content and changes in the degree of disorder in NCNTs along with the formation crystalline TiO_2 embedded in SiO_2 amorphous layer may collectively promote the formation of Pt nanorod like structures on *An*-TiSi$_2$O$_x$-NCNTs compared to Pt nanoparticles on TiSi$_2$O$_x$-NCNTs.
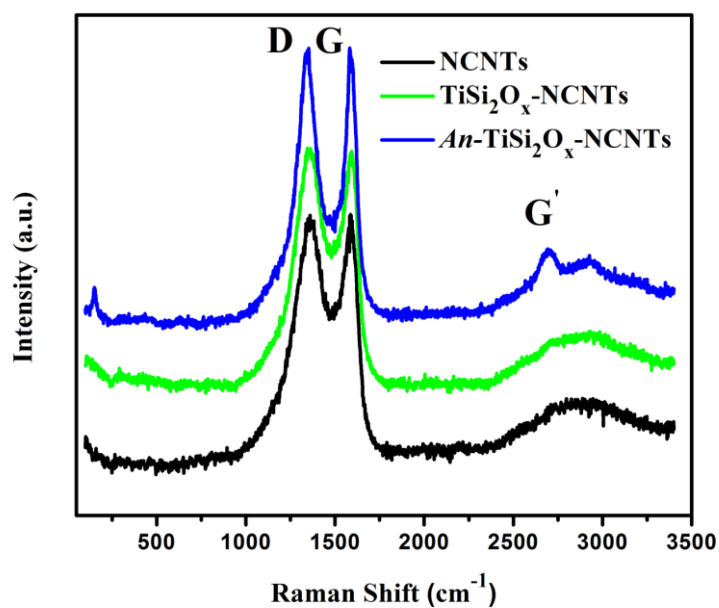
Figure 5.7 Raman spectrum of NCNTs and composite nanostructures deposited on carbon paper.

5.4   Conclusion

In summary, composite nanostructures of NCNTs coated with $TiSi_2O_x$ were synthesized for use as Pt catalysts support for ORR. The nanostructures were synthesized using a combination of CVD and magnetron sputtering processes. Experimental results showed that $TiSi_2O_x$ formed an amorphous layer with variable thickness on CNTs. Annealing treatment of the composite nanostructures promoted the formation of TiO_2 nanocrystals embedded in the amorphous $TiSi_2O_x$ matrix. XANES spectra of Ti K-edge and Si K-edge confirmed the presence of rutile TiO_2 and SiO_2 in the sputtered layer. Electrochemical properties of Pt deposited composite nanostructure were investigated. Compared to Pt/$TiSi_2O_x$-NCNTs and Pt/NCNTs, Pt/*An*-$TiSi_2O_x$ -NCNTs exhibited a 30mV positive potential and larger mass and specific activity for ORR. XANES spectra of Pt L_2-edge and Pt L_3 edge and their quantitative whiteline analysis of the three electrocatalysts confirmed the presence of higher density of unoccupied states in Pt 5d orbitals for Pt on composite supports compared to NCNTs. These results indicate a SMSI between composite supports and Pt, which leads to higher catalytic activity. TEM observations reveal the formation of Pt nanorod like structures on *An*-$TiSi_2O_x$-NCNTs compared to sphere like nanoparticles deposited on pristine $TiSi_2O_x$-NCNTs. The high performance of Pt/*An*-$TiSi_2O_x$-NCNTs than Pt/$TiSi_2O_x$-NCNTs is attributed to the nanorod like shape of Pt and the synergistic effect between Pt, SiO_x and TiO_2 on the annealed $TiSi_2O_x$ layer. Our results show that multi components composite nanostructures are promising supports for oxygen reduction reactions in PEMFCs.

5.5　　　References

[1]　　　Andress D, Das S, Joseck F and Dean Nguyen T 2012 Energy Policy 41 348–364

[2]　　　Higgins DC, Meza D and Chen Z 2010 The Journal of Physical Chemistry C 114 21982–21988

[3]　　　Saha MS, Li R, Sun X and Ye S 2009 Electrochemistry Communications 11 438–441

[4]　　　Chen Y 2009 Electrochemistry Communications 11 2071–2076

[5]　　　Xiong W, Du F, Liu Y, Perez A, Supp M, Ramakrishnan TS, Dai L and Jiang L 2010 Journal of the American Chemical Society 132 15839–15841

[6]　　　Chen Z, Higgins D, Tao H, Hsu RS and Chen Z 2009 The Journal of Physical Chemistry C 113 21008–21013

[7]　　　Gong K, Du F, Xia Z, Durstock M and Dai L 2009 Science 323 760 –764

[8]　　　Saha MS, Banis MN, Zhang Y, Li R, Sun X, Cai M and Wagner FT 2009 Journal of Power Sources 192 330–335

[9]　　　Saha MS, Li R, Cai M and Sun X 2007 Electrochemistry Solid-State Letters. 10 130–133

[10]　　Jeon MK Electrochemistry Communications 9 2692–2695

[11]　　Antolini E and Gonzalez ER 2009 Solid State Ionics, Diffusion & Reactions 180 746–763

[12]　　Antolini E 2010 Applied Catalysis B: Environmental 100 413–426

[13]   Kang SH, Sung Y-E and Smyrl WH Journal of Electrochemical Society 155 1128–1135

[14]   Beak S, Jung D, Nahm KS and Kim P 2010 Catalysis Letters 134 288–294

[15]   Wang R 2011 International Journal of Hydrogen Energy 36 5775–5781

[16]   Higgins DC, Meza D and Chen Z 2010 Journal of Physical Chemistry C 114 21982–21988

[17]   Zhou J Chemical Physics Letters 437 229–232

[18]   Jia J, Kou Y, Lin L, Xu Z, Zhang T, Niu J and Liang D 1998 Reaction Kinetics and Catalysis Letters 63 391–396

[19]   Boyanov BI and Morrison TI 1996 Journal of Physical Chemistry 100 16318–16326

[20]   Mazumder V, Lee Y and Sun S 2010 Advanced Functional Materials 20 1224–1231

[21]   Sun S, Jaouen F and Dodelet J 2008 Advanced Materials 20 3900–3904

[22]   Liu H, Zhang Y, Li R, Sun X, Désilets S, Abou-Rachid H, Jaidann M and Lussier L-S 2010 Carbon 48 1498–1507

[23]   Meng X, Zhong Y, Sun Y, Banis MN, Li R and Sun X 2011 Carbon 49 1133–1144

[24]   Chen Y, Wang J, Liu H, Banis MN, Li R, Sun X, Sham T-K, Ye S and Knights S 2011 Journal of Physical Chemistry C 115 3769–3776

[25]   Yang D-Q, Sun S, Dodelet J-P and Sacher E 2008 The Journal of Physical Chemistry C 112 11717–11721

[26]   Sun SH, Yang DQ, Villers D, Zhang GX, Sacher E and Dodelet JP 2008 Advanced Materials 20 571–574

[27]   Cheung CL, Kurtz A, Park H and Lieber CM 2002 The Journal of Physical Chemistry B 106 2429–2433

[28]   Wang X, Liu Y, Zhu D, Zhang L, Ma H, Yao N and Zhang B 2002 The Journal of Physical Chemistry B 106 2186–2190

[29]   He M, Zhou S, Zhang J, Liu Z and Robinson C 2005 The Journal of Physical Chemistry B 109 9275–9279

[30]   Saha MS, Li R, Sun X and Ye S 2009 Electrochemistry Communications 11 438–441

[31]   Broadbent EK 1987 Thin Solid Films 151 51–63

[32]   Pantel R, Levy D, Nicolas D and Ponpon JP 1987 J. Appl. Phys. 62 4319–4321

[33]   Wee ATS, Huan ACH, Osipowicz T, Lee KK, Thian WH, Tan KL and Hogan R 1996 Thin Solid Films 283 130–134

[34]   Nam C, Kim Y-S, Kim WB and Cho BK 2008 Nanotechnology 19 475703–475707

[35]   Wilson NR and Macpherson JV 2003 Nano Letters 3 1365–1369

[36]   Rogachev A and Bezryadin A 2003 Applied Physics Letters. 83 512–515

[37]   Sankur H and Gunning W 1989 Journal of Applied Physics 66 4747–4751

[38]   Goldstein JI, Choi SK, Van Loo FJJ, Bastin GF and Metselaar R 1995 Journal of the American Ceramic Society 78 313–322

[39]   Gencer Imer A, Yildiz I and Turan R 2010 Physica E: Low-dimensional Systems and Nanostructures 42 2358–2363

[40]   Sadoh T, Owatari M, Murakami Y, Kenjo A, Yoshitake T, Itakura M, Enokida T and Miyao M 2004 Thin Solid Films 461 77–80

[41]   Hofman D, Kleint C, Thomas J and Wetzig K 2000 Ultramicroscopy 81 271–277

[42]   Sammynaiken R et al. 2002 Journal of Applied Physics 92 3000–3006

[43]   Lee JS, Kim WB and Choi SH 2001 Journal of Synchrotron Radiation 8 163–167

[44]   Wu ZY et al. 2002 Applied Physics Letters 80 2973–2975

[45]   Yogi C et al. 2011 Journal of Physical Chemistry C 115 6554–6560

[46]   Farges F, Brown GE and Rehr JJ 1997 Physical Reviews B 56 1809–1819

[47]   Shuji M, Nahomi S and Hisanobu W 2005 Analytical Sciences 21 805–809

[48]   Ciapina EG 2010 Journal of Electroanalytical Chemistry 644 132–143

[49]   Maillard F, Schreier S, Hanzlik M, Savinova ER, Weinkauf S and Stimming U 2005 Physical Chemistry Chemical Physics 7 385–393

[50]   Maillard F, Eikerling M, Cherstiouk OV, Schreier S, Savinova E and Stimming U 2004 Faraday Discussions 125 357–377

[51]   Sun S, Zhang G, Geng D, Chen Y, Banis MN, Li R, Cai M and Sun X 2010 Chemistry - A European Journal 16 829–835

[52]   Sun S, Zhang G, Geng D, Chen Y, Li R, Cai M and Sun X 2011 Angewandte Chemie International Edition 50 422–426

[53]   Brown M, Peierls RE and Stern EA 1977 Physical Review B (Solid State) 15 738–744

[54]   Sham TK, Naftel SJ and Coulthard I 1996 Journal of Applied Physics 79 7134–7138

[55]   Min M-K, Cho J, Cho K and Kim H 2000 Electrochimica Acta 45 4211–4217

[56]   Lima F, Zhang J, Shao M, Sasaki K, Vukmirovic M, Ticianelli E and Adzic R 2008 Journal of Solid State Electrochemistry 12 399–407

[57]   Akalework NG, Pan C-J, Su W-N, Rick J, Tsai M-C, Lee J-F, Lin J-M, Tsai L-D and Hwang B-J 2012 Journal of Materials Chemistry 22 20977-20985

[58]   Mansour AN, Cook JW and Sayers DE 1984 Journal Physical Chemistry 88 2330–2334

[59]   Mattheiss LF and Dietz RE 1980 Physical Reviews B 22 1663–1676

[60]   Sun S, Yang D, Zhang G, Sacher E and Dodelet J-P 2007 Chemistry of Materials 19 6376–6378

[61]   Gong QM Materials Research Bulletin 42 474–481

[62]   Chen J Carbon 45 274–280

[63]   Bulusheva LG, Okotrub AV, Kinloch IA, Asanov IP, Kurenya AG, Kudashov AG, Chen X and Song H 2008 physica status solidi (b) 245 1971–1974

[64]   Choi HC, Bae SY, Jang W-S, Park J, Song HJ, Shin H-J, Jung H and Ahn J-P 2005 The Journal of Physical Chemistry B 109 1683–1688

Chapter 6

6   TiO$_2$ Nanoparticle Decorated Nitrogen Doped Carbon Nanotubes as Pt Catalyst Support for Low Temperature Fuel Cells[1,2]

In the previous chapter the authors introduced composite nanostructures of TiSi$_2$O$_x$-NCNTs as potential catalysts supports for PEMFCs. The Pt/TiSi$_2$O$_x$ NCNTs exhibited a higher catalytic activity towards oxygen reduction reaction compared to Pt/C catalysts and higher stability and CO tolerance as well.

In this chapter following the same concept, TiO$_2$ decorated NCNTs were prepared as catalyst supports for PEMFCs. These nanostructures were prepared by wet chemical etching of SiO$_2$ from annealed TiSi$_2$O$_x$-NCNTs in order to increase their electrical conductivity and interaction with Pt catalyst. Electrochemical characterization of Pt/TiO$_2$-NCNTs electrocatalyst show that these nanostructures have higher catalytic activity towards oxygen reduction, methanol oxidation and enhanced CO tolerance compared to the commercial Pt/C electrodes. X-ray absorption spectroscopy analysis of Pt L$_{2,3}$ edge of the Pt catalysts deposited on the composite nanostructures demonstrates a significant change in their electronic structure, indicating a strong metal support interaction, which promises the enhanced catalytic effect of the composite nanostructured electrocatalyst.

[1] Shuhui Sun[a], Yong Zhang[a], Ruying Li[a], Mei Cai[b] Tsun-Kong Sham[c] and Xueliang Sun[a]

a. Department of Mechanical and Materials Engineering, The University of Western Ontario, London, Ontario N6A 5B9 (Canada)
b. General Motors R&D Center, Warren, MI 48090-9055 (USA)
c. Department of Chemistry, University of Western Ontario, London, Ontario N6A 5B7 (Canada)
Email: xsun@eng.uwo.ca

6.1   Introduction

Fuel cells have attracted considerable attention as electrochemical energy conversion devices for transport, stationary and portable applications due to their high efficiency and low emissions.

The commercialization of fuel cells, despite the significant advances in this field, is hindered by three main issues: insufficient stability of the electrocatalysts, low activity of catalyst for oxygen reduction reaction (ORR) and high cost.[1−8] In order to obtain sufficient electrical output from a fuel cell, the electrochemical reaction must occur at a sufficient rate.

Catalysts exhibit great influence on both the reaction rate and the cost of PEMFCs. The support materials typically provide a physical surface for dispersion of small metal particles which is necessary for achieving high surface area. Highly dispersed platinum or platinum based catalysts on a conductive support such as carbon black are commonly used as electrode materials for oxidation and reduction reaction. However commercially available carbon black does not always exhibit ideal corrosion resistance required for catalyst support in fuel cell working environment [9].

Therefore various alternatives of electrocatalysts supports are being studied. Recently carbon material, such as carbon nanotubes, have been considered as new catalyst supports due to their good electrical conductivity and superior electrochemical corrosion resistance [10]. However studies have shown that the inert surface of CNTs lead to lower anchoring sites for Pt deposition [3,11,12]. To obtain better deposition of Pt nanoparticles on these nanostructures, nitrogen-doping on carbon nanotubes (NCNTs) has been reported as an effective way. It has been shown that Pt nanoparticles deposited on NCNTs (Pt/NCNTs) show remarkable electrochemical stability [5] and higher fuel cell performance [3,7]. Furthermore, research has indicated that NCNTs show ORR activity in alkaline fuel cells and this has been related to the nitrogen content and high degree surface defect of these nanostructures [1,13].

Inorganic metal oxides have also been studied as good corrosion resistant supports in PEMFCs. Studies have shown these materials can also interplay with catalytic metals, influencing the catalytic activity of Pt. Among the inorganic metal oxides, SnO_2, WO_x and TiO_2 nanostructures such as nanorods nanowires and nanotubes have been used as catalysts or supports on electrochemical applications. Saha et al. [13, 14] have shown $W_{18}O_{49}$ nanowires grown directly on carbon paper, can also act as good catalyst supports. Their results indicate $Pt/W_{18}O_{49}$ electrocatalysts exhibit higher activity toward ORR than the commercial Pt/C electrodes. Lim et al. [16] has reported the use of TiO_2 nanotubes as catalysts support for PEMFCs. They have shown that these materials act as a very durable supports compared to carbon supports. Furthermore, studies have shown TiO_2 may improve the Pt ORR activity through various mechanisms [17,18]. SnO_2 nanowires have been shown to enhanced the catalytic activity of Pt for ORR and methanol oxidation (MOR) as catalysts supports in low temperature fuel cells [4,19].

In spite of the various properties of metal oxides which make them potential candidates as catalyst supports in low temperature fuel cells, replacing carbon based material with metal oxides such as TiO_2 is difficult due to their low electrical conductivity at temperatures below $200^\circ C$ [20,21]. Therefore, composite metal oxide- carbon materials have been proposed as fuel cell catalyst supports [20,22]. These materials exhibit the desired properties as catalyst supports which are unattainable by their individual components. In composite supports, carbon is mainly used to stabilize highly dispersed metal oxide nanoclusters. This maximizes the interaction between the metal oxide material and the metal catalyst. For example TiO_2/C composites have been synthesized by different means such as hydrolysis of titanium alkoxides [23] or microwave assisted polyol process [8]. $Pt/TiO_2/C$ synthesized by these methods, exhibits an enhanced methanol tolerance and stability compared to Pt/C. Jiang et al.[8] studied the size effect of TiO_2 nanoparticle in $Pt/TiO_2/C$ electrocatalyst and revealed that TiO_2 with an average size of 20 nm enhanced the ORR activity and stability of the electrocatalyst.

In this study, to take advantage of the high surface area provided by NCNTs and interaction between TiO_2 and Pt catalysts, TiO_2 decorated NCNTs composite material was fabricated directly on carbon paper through CVD and magnetron sputtering process. The physical and electrochemical properties of the composite electrocatalysts were characterized. To understand the change in the electrochemical activity of the electrocatalysts, X-ray absorption fine structure (XAFS) spectroscopy was used. Ti K-edge, Si K-edge and Pt $L_{3,2}$ edge at the X-ray absorption near edge structure (XANES) provide detailed information about the chemical state and electronic structure of each component of the electrocatalysts.

6.2   Experimental Procedure

6.2.1 Composite Nanostructure Synthesis

TiO_2 nanoparticle decorated NCNTs were synthesized via combination of CVD, magnetron sputtering and solution etching processes. The composite nanostructures were grown on the commercially available carbon paper (E-TEK, a division of De Nora North America, Somerset, NJ), composed of carbon microfibers of 5-10mm in diameter.

The NCNTs were directly grown on carbon paper by CVD method, using thin layer of Fe as the catalyst and melamine ($C_3H_6N_6$, Aldrich, 99%) as the source of carbon and nitrogen. The detailed synthesis of NCNTs using this process has been reported elsewhere [11,24,25]. In detail, aluminum (Al) layer with a thickness of 30 nm was sputtered on the carbon paper as a buffer layer. Thin layer, 1-2 nm thick Fe layer was sputtered on the Al layer to act as the catalyst. The substrates were placed in the center of the quartz tube. Melamine was put at the low temperature region (upstream). The tube was mounted on a horizontal electric furnace and Ar (99.999%) was introduced into the system for 30 min to purge air out. The temperature was raised to 800 °C, and held at this temperature for 30 min. During this period a constant flow of Ar (300 sccm) was maintained in the system. After the experiment, a dark layer covered the substrate.

The NCNTs on carbon paper were placed in the plasma enhanced chemical vapor deposition-sputtering system (PECVD). A 100 nm layer of $TiSi_2O_x$ was deposited on the NCNTs from $TiSi_2$ target (Kurt J. Lesker, 2 inch, 99.9%) using a RF magnetron (150 W, 10 min). The oxygen was introduced from the residual oxygen in the sputtering chamber. The composite nanostructures were then heat-treated at 1000 ^{o}C for 6 hr under a constant flow of Ar (99.999%) to convert the $TiSi_2O_x$ layer into TiO_2 nanoparticles with controlled diameters and SiO_x layer.

The SiO_x layer was removed via NaOH treatment. The heat-treated nanostructures were submersed in NaOH solution (10 wt%) for 48 hr. The treated nanostructures (TiO_2-NCNTs) were washed in deionized water and dried at room temperature overnight.

6.2.2 Pt deposition

Pt nanoparticles were deposited on TiO_2-NCNTs nanostructures by a formic acid method [26]. In this method, the Pt precursor ($H_2PtCl_6.6H_2O$, Aldrich, 99.95%) and formic acid (HCOOH, Aldrich, 98%) were used as received. The synthesis was conducted in an environmentally friendly solution of deionized water. The reduction process is given by

$$H_2PtCl_6 + 2HCOOH = Pt + 6H^+ + 6Cl^- + 2CO_{2\ (g)}$$

In this process, 1 mL of 0.03 M $H_2PtCl_6.6H_2O$ and 1mL HCOOH were simultaneously mixed with 20 mL of water at room temperature. TiSix-NCNT nanostructures on carbon paper were immersed in the solution and the reaction was carried out in 80 °C for ~ 15 min. In this period the color of the solution turned from golden orange to dark brown, indicating the formation of Pt nanoparticles. After the solution was cooled down, the composite nanostructures on carbon paper was removed from the solution, washed by deionized water and dried at room temperature overnight.

6.2.3 Physical Characterization

The morphologies of the products were characterized using field emission scanning electron microscope (SEM, Hitachi S4800, operated at 5.0 kV) equipped with energy dispersive X-ray spectroscope (EDX), transmission electron microscope (TEM, Hitachi 7000, operated at 100 kV), and high resolution TEM (HRTEM, JEOL 2010, operated at 200 kV) along with selected area electron diffraction (SAED) pattern. The crystal structure and composition of the products was characterized by X-ray diffractometer (XRD) using Co Kα1 ($\lambda = 0.179$ nm) radiation operated at 45 kV and 35 mA.

6.2.4 X-ray Absorption Spectroscopy

Ti K-edge data were collected at the Soft X-ray Microcharacterization Beamline (SXRMB) of the Canadian Light Source (CLS, operated at 2.9 GeV) which has an energy range of 1.7 – 10 keV. Si (111) crystal monochromator was used to collect the XANES

spectra at Ti K-edge. The XANES were recorded in total electron yield (TEY) using specimen current detector.

The Pt $L_{3,2}$ edge adsorption spectra X-Ray Absorption Fine Structure (XAFS) measurements were performed on the Pacific Northwest Consortium X-ray science division (PNC-XSD) ID-20B beamline of the advance photon source (APS operated at 7 GeV) at Argonne National Laboratory. Measurements were made at room temperature in transmission mode for Pt foil and commercial Pt/C catalysts and in fluorescence mode using a solid state detector. The software package ATHENA version 0.8.056 was used for data reduction.

The Pt $L_{3,2}$ edge white line intensity was analyzed using the Au metal L3,2-edge XANES as the background since Au metal exhibits no white line and has the same face centered cubic structure as Pt metal. Both Au and Pt XANES were calibrated relative to the edge threshold (Eo, point of inflection of the rising edge jump) with the edge jump normalized to unity (atomic edge jump, for Pt unity edge jump at the L_3 and L_2 edge has a value of $2.5 \times 10^3 cm^{-1}$ and 1.13×10^3 cm^{-1}, respectively. Thus the area under the difference curve in the white line region between Pt and Au, denoted ΔA_3 and ΔA_2 for the L_3 and L_2 edge respectively, will be proportional to the unoccupied densities of states of Pt 5d character for the samples.

6.2.5 Electrochemical Measurements

Cyclic voltammetry was conducted at room temperature using an Autolab potentiostat/galvanostat (Model, PGSTAT-30, Ecochemie, Brinkman Instrument) with a standard three-electrode, two-compartment configuration. Pt wire and Ag/AgCl (3M NaCl) electrode were used as the counter and reference electrodes, respectively. For hydrogen electrosoprtion curves measurement, the potential was cycled between -0.159 V and 0.991 V at 50 mV/s to obtain the voltammograms of hydrogen adsorption in Ar-purged 0.5M H_2SO_4 aqueous solution. For ORR measurement, O_2 (99.99%) was first purged into solution at a position close to the working electrode for at least 30 min. The

measurements were done by linear potential sweeping from 0.8 V to 0.2 V. The electrochemical properties of the composite nanostructures were compared to two standard electrodes: Pt/NCNTs and 30wt% Pt/C commercial catalyst from ETEK. Pt nanoparticles were deposited on NCNTs via similar procedure mentioned above for Pt/TiO$_2$-NCNTs.

6.3   Results and Discussion

Physical characterization of composite nanostructures of TiO$_2$-NCNTs illustrates the successful deposition of TiO$_2$ nanoparticles with controlled diameters on NCNTs. Figure 6.1 shows the SEM and TEM micrographs of TiO$_2$-NCNTs samples. SEM observations of NCNTs before TiO$_2$ deposition and NaOH treatment showed these nanostructures grown on carbon fibers to have an open 3D morphology. SEM images of these nanostructures after TiO$_2$ deposition (Figure 6.1a) show no significant change in the morphology of composite nanostructures compared to pristine NCNTs, indicating TiO$_2$ deposition process does not alter the morphology of NCNTs significantly. High magnification SEM images, (Figure 6.1b) reveal the deposition of high density of nanoparticles on NCNTs. Further analyses of TiO$_2$-NCNTs via TEM, shown in Figure 6.1c, reveal that the nanoparticles have an average diameter of 12 nm. The regular trapezoid shape of most of the nanoparticles, and the SAED pattern of the composite nanostructure (inset of Figure 6.1c) confirm high crystallinity of TiO$_2$ nanoparticles. The SAED pattern can be closely indexed to the rutile TiO$_2$ tetragonal crystal structure (JCPDS 21-1276). Clear lattice fringes of these nanoparticles shown in the HRTEM image; imply the TiO$_2$ nanoparticles to be single crystals. The measured distance of these lattice fringes correspond to the (110) plane of the rutile TiO$_2$ crystal.
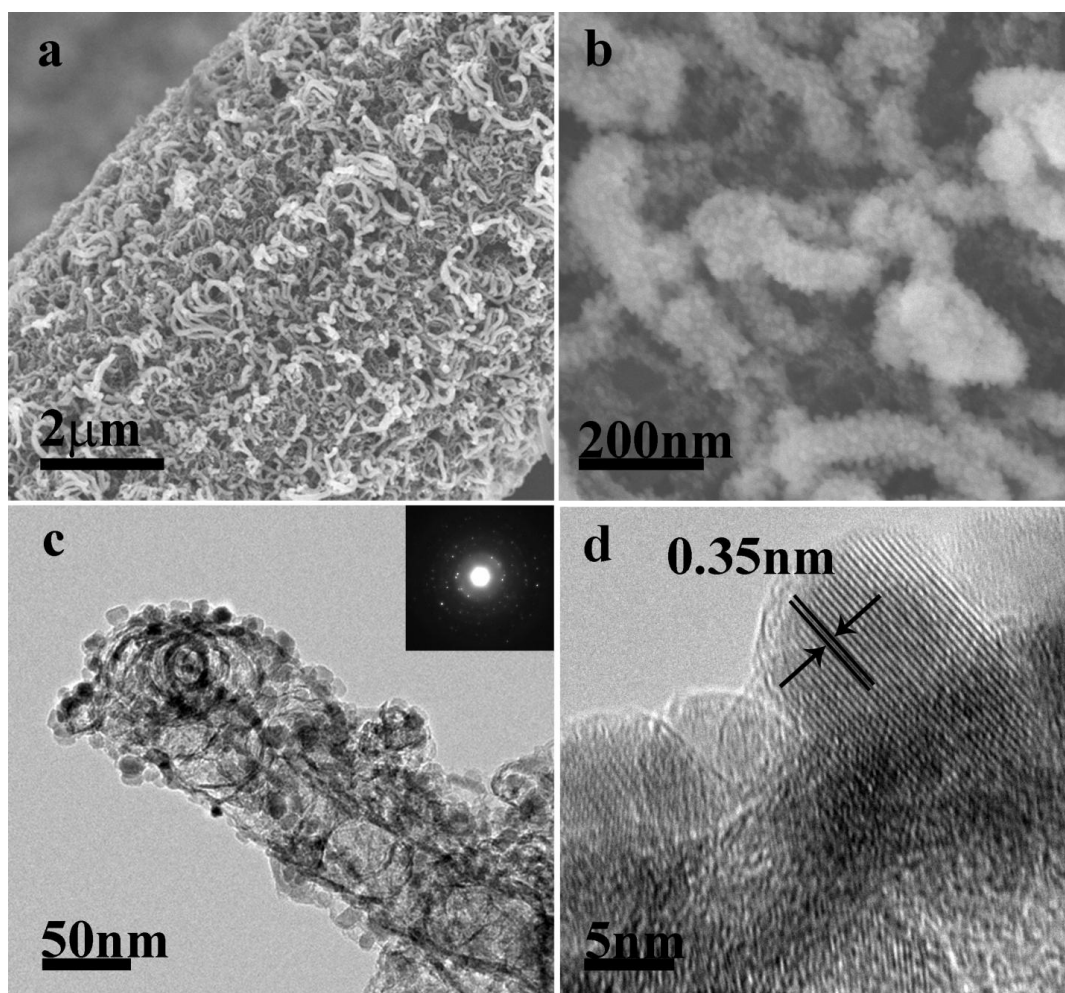
Figure 6.1 a) SEM and b) High magnification SEM, c) TEM and HRTEM images of TiO$_2$-NCNTs nanostructures.

Further characterization of the composite nanostructures was conducted through analysis of XANES spectra of composite nanostructures including TiO$_2$-NCNTs and Pt/TiO$_2$-NCNTs at Ti K edge. Figure 6.2 shows the Ti K edge XANES of these nanostructures in the range of 4960 to 5040 eV, together with the spectra of rutile TiO$_2$ reference sample. All spectra were normalized to an edge jump of unity for comparison. Ti K-edge XANES study confirms the structure of the sample evidenced by TEM and SAED pattern indicating the rutile nature of the TiO$_2$ nanoparticles.
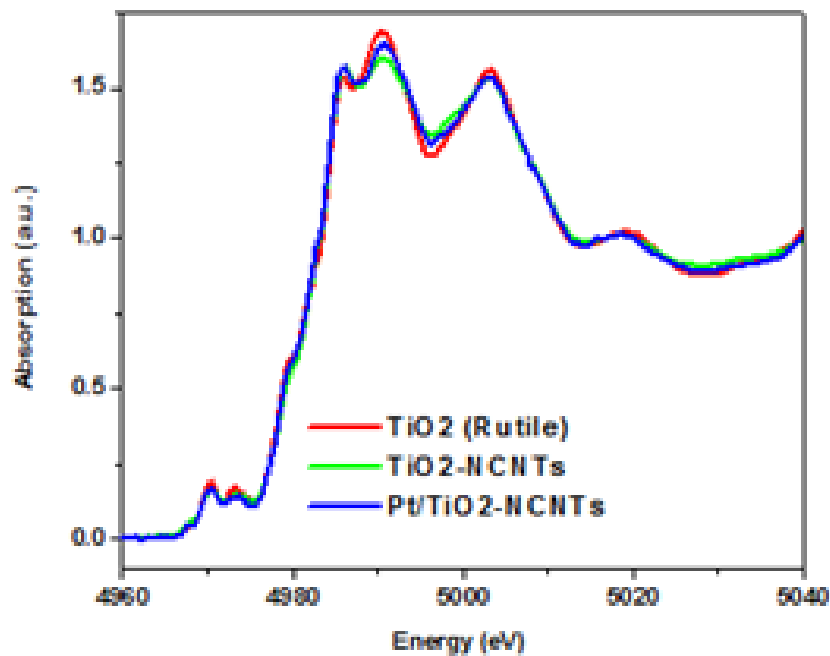
Figure 6.2 The normalized XANES spectra of composite nanostructures at Ti K edge.

Figure 6.3 shows TEM and HRTEM images of Pt nanoparticles deposited on TiO_2-NCNTs nanostructures. TEM observation, reveal high density of Pt nanoparticles with an average size of 4 nm deposited on exposed surfaces of NCNTs, this is consistent with previous reports on the deposition of Pt nanoparticles on carbon surfaces via similar process by Yang et al [26].
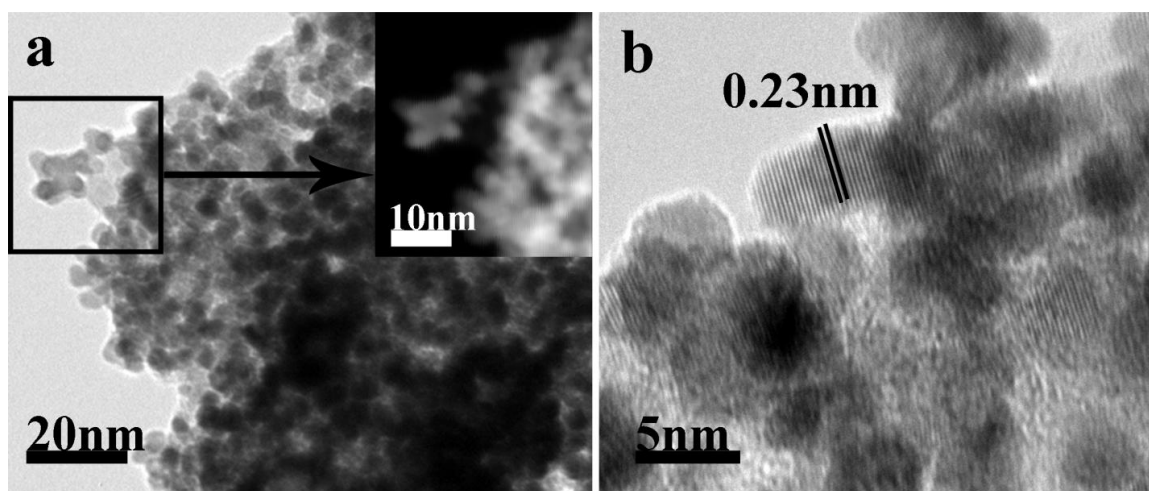
Figure 6.3 a) TEM and b) HRTEM image of Pt nanoparticles deposited on TiO₂-NCNTs (Pt/TiO₂-NCNTs). Inset in (a) shows the HADDF image of Pt nanoparticles deposited on TiO₂ nanoparticles.

Studies have shown that Pt deposition on metal oxides and SiO_2 containing surfaces using reduction methods leads to limited uniformity and low Pt loading. This is due to strong interaction requirement between the Pt precursor and the substrate. When H_2PtCl_6 is used as Pt precursor in an acidic environment (even as low as PH=1), since there is no strong interaction between $PtCl_6^{2-}$ and oxide surfaces, the loading of Pt is greatly reduced [27]. In this study, TEM observations confirm the deposition of Pt nanoparticles on TiO_2 surfaces (relatively lower density compared to NCNTs). Inset image of Figure 6.3a shows high-angle annular dark field (HAADF) image of the selected area in Figure 6.3a, clearly indicating the presence of Pt nanoparticles (bright particles) on the top of TiO_2 nanoparticles (darker particles). The HRTEM image (Figure 6.3b) of the Pt nanoparticles deposited on the composite structures shows the deposition of single crystalline Pt nanoparticles with clear lattice fringes. The measured spacing of these fringes confirms the metallic nature of the Pt nanoparticles. Furthermore, these images indicate, in contrast to other Pt deposition processes, Pt nanoparticles deposited via formic acid reduction method have small nanorod like morphology. HRTEM measurements reveal these Pt nanoparticles to have an aspect ratio of around 2. This can be attributed to the Pt

deposition process and the substrate, similar results have been reported by Sun et al.[28,29]. They reported the synthesis of Pt nanorods and nanowires by modifying the Pt deposition process to promote one dimensional growth of the Pt nanostructures.

The electrochemical properties of Pt/TiO$_2$-NCNTs composites were evaluated using cyclic voltammetry (CV). For comparison Pt/NCNTs and cPt/C commercial catalyst were examined under identical conditions. The CVs (Figure 6.4a) of these composite nanostructures were recorded in Ar-saturated 0.5 M H$_2$SO$_4$ aqueous solution at room temperature between -0.159 and 0.991 V vs Ag/AgCl (3M NaCl), with a scan rate of 50 mVs^{-1}. The voltammetric features of all the electrodes reveal the typical characteristics of Pt metal, with the adsorption and deposition of hydrogen between -0.154 to 0.991 V and Pt oxide formation and its reduction between 0.5 and 0.991 V.

Multiple peaks for hydrogen adsorption and desorption were seen on Pt/TiO$_2$-NCNTs and Pt/NCNTs electrocatalysts compared to a single broad peak seen on Pt/C. This phenomenon implies the reaction involved multiple exposed crystallographic planes. The electrochemically active surface area (ECSA) of the samples can be estimated based on the total charge of hydrogen desorption (Q$_H$) according to the following equation:

$$A_{EL} = Q_H/(210\mu Ccm^{-2} \text{ x Pt loading})$$

The A$_{EL}$ is expressed in cm^{2}mg^{-1} where the Pt loading is in mg$_{pt}$cm^{-2}. Values of A$_{EL}$= 59.3, 276.6 and 123.4 cm^{2}mg^{-1} have been obtained for Pt/TiO$_2$-NCNTs, Pt/NCNTs and Pt/C respectively. The high value of A$_{EL}$ for Pt/NCNTs is well documented, and has been attributed to the high surface area of NCNTs and 3D open structures of these nanomaterials grown on carbon paper [10]. The significant reduction in the active surface of Pt/TiO$_2$-NCNTs can be attributed to the intrinsic 1D morphology of Pt nanostructures compared to Pt nanoparticles deposited on composite nanostructures. In addition the presence of residual SiO$_2$ on the surface of NCNTs further reduces the ESCA of these electrocatalysts.
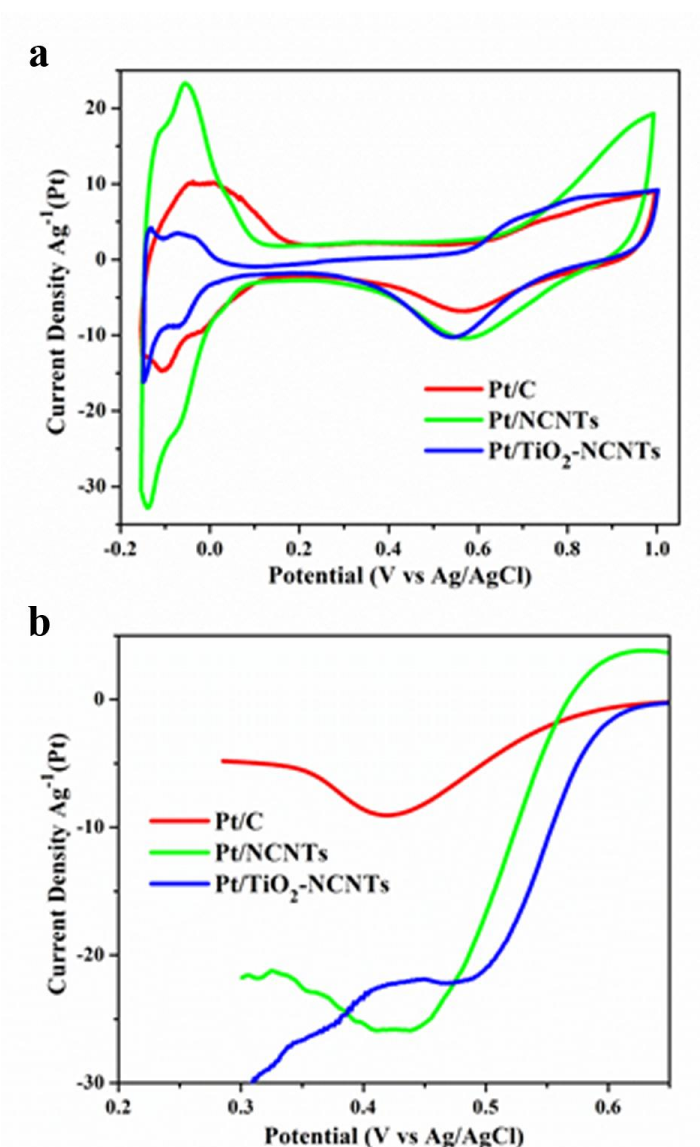
Figure 6.4 Electrochemical characterization of composite nanostructures. a) Cyclic voltammetry curves, b) Oxygen reduction curves of Pt/TiO$_2$-NCNTs composite electrodes. The samples were compared to Pt deposited nitrogen doped carbon nanotubes (Pt/NCNT NCNTs) and Pt/C. Potential scan rate 50 mVs^{-1}.

The electrocatalytic activities for ORR of the composite electrodes are compared in Figure 6.4b, by linear scanning voltammetry, at a scan rate of 50mVs^{-1}. Results illustrate the higher peak potential of Pt/TiO$_2$-NCNTs compared to other two selected. The peak

potential of Pt/TiO$_2$-NCNTs is 0.47 V while that of Pt/NCNTs and Pt/C are at 0.44 V and 0.41 V respectively. At peak potential the mass activity of Pt/TiO$_2$-NCNTs (22.2 Ag^{-1}) is 2.42 times higher than Pt/C (9 Ag^{-1}). However, it is 0.15% smaller than Pt/NCNTs (26 Ag^{-1}). By taking into account the active surface area, specific ORR activity for Pt/TiO$_2$-NCNTs (3.83 Am^{-2}) is 5.5 times higher than Pt/C (0.73 Am^{-2}) and 4 times higher than Pt/NCNTs (0.94 Am^{-2}). As reported previously, these results indicate that the presence of TiO$_2$ nanoparticles enhances the electrocatalytic activity of Pt nanoparticles towards ORR [8]. However, Pt/TiO$_2$-NCNTs supports show lower mass activity compared to Pt/NCNTs due to low conductivity of TiO$_2$ [8].

The electrocatalytic activity of the Pt/TiO$_2$-NCNTs for methanol oxidation was also examined in a solution containing 1M MeOH and 0.5M H$_2$SO$_4$. The corresponding results are shown in figure 6.5a. Before the deposition of Pt nanoparticles no methanol oxidation was observed (not shown). After the Pt deposition typical features of methanol oxidation were detected, which are in good agreement with literature [19,29]. As shown in Figure 6.5a, the peak potential for methanol oxidation in the forward scan on Pt/TiO$_2$-NCNTs (0.64 V) is lower than Pt/NCNTs (0.69) and Pt/C electrode (0.7). This indicates that Pt nanoparticles supported on TiO$_2$-NCNT composite are able to significantly reduce the overpotential in methanol oxidation. Furthermore, the oxidation peak current for the Pt/TiO$_2$-NCNTs [126 Ag^{-1} (Pt)] is about 1.4 and 1.9 times higher than Pt/NCNTs [90.6 Ag^{-1} (Pt)] and Pt/C [66.7Ag^{-1} (Pt)] respectively. In terms of the activity per unit active surface, the difference between Pt/TiO$_2$-NCNTs and the two reference materials should be larger considering the lower surface of area of Pt/TiO$_2$-NCNTs, which suggests a positive effect of TiO$_2$ on the catalytic activity of Pt towards methanol oxidation.

Figure 6.5b, shows adsorbed CO (CO$_{ads}$) stripping voltammograms for Pt/TiO$_2$-NCNTs composite along with Pt/NCNTs and Pt/C electrodes in 0.5M H$_2$SO$_4$ solution at a scan rate of 50mVs^{-1}. CO was purged while holding at -0.159V vs Ag/AgCl (3M NaCl) for 30min at 25°C. The observed peak potential at 0.59V for the Pt/TiO$_2$-NCNTs, is lower than Pt/NCNTs (0.61V) and Pt/C (0.66V). The results indicate that the CO$_{ads}$ oxidation

becomes energetically more favorable at Pt/TiO$_2$-NCNTs compared the other two electrodes, indicating that the presence of TiO$_2$, allows the adsorbed CO to be oxidized at lower potentials confirming the methanol oxidation observations. This result is in good agreement with the reports on the effect of titanium oxides on the CO tolerance and methanol oxidation of Pt catalyst nanoparticles [6,18,21,23].
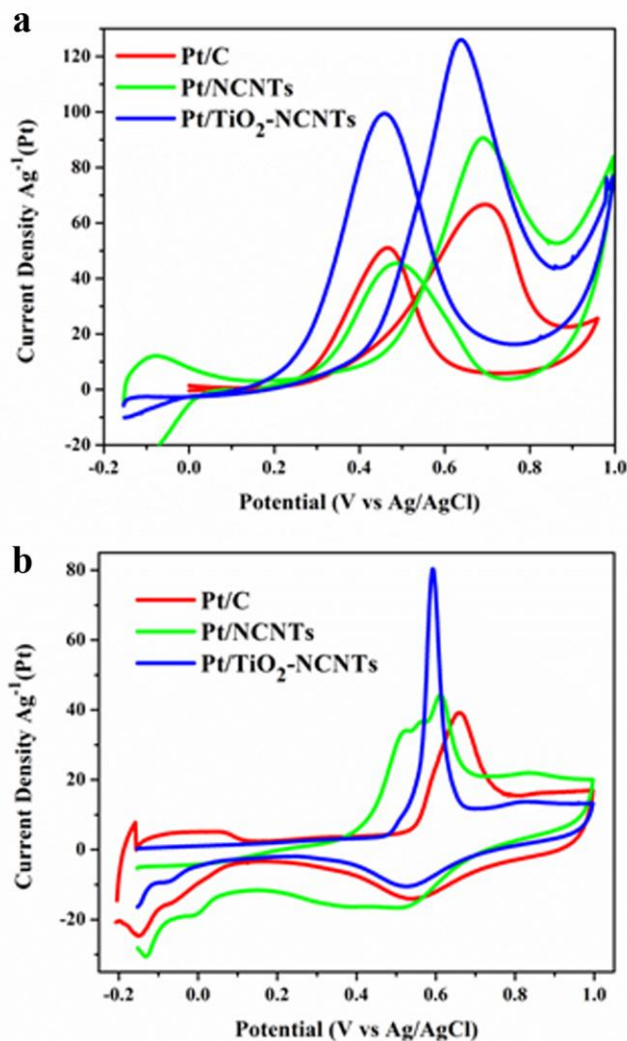
Figure 6.5 Cyclic voltammograms for a) methanol oxidation (1M methanol in 0.5M H$_2$SO$_4$) b) in the presence of CO in 0.5M H$_2$SO$_4$ aqueous solution at room temperature for Pt/TiO$_2$-NCNTs, Pt/NCNTs and Pt/C electrode. Potential scan rate 50 mVs^{-1}.

An important aspect of reactivity in fuel cell electrocatalysts is the interaction between the metal catalysts (Pt) and the support. Recently, significant progress has been made towards understanding the nature of these interactions [30], and their effect on the activity of electrocatalysts. Strong metal support interaction (SMSI) has been reported between metal oxides such as TiO_2 support and Pt catalysts [31,32]. Studies have shown that SMSI results in the change of metal catalyst electronic structure, subsequently changing the catalytic activity of the catalyst. Zhang et al. [33] discussed the correlation between the d-band center and ORR activity of the catalysts. Their result shows that stronger or weaker binding energy of atomic oxygen at various substrates causes a sluggish ORR. Todae et al. [34] have also studied the electronic effects of alloyed catalysts on the ORR in acid electrolytes. Their results indicate that ORR activity strongly depends on the Pt d-band vacancies. Other reports have also confirmed that the catalytic activity of Pt for various electrochemical reactions including ORR is related to the density of state of employed Pt [35–37]. Furthermore, the metal support interactions between the catalyst support and catalyst has been evaluated through study of XANES spectrum [38–40]. The qualitative and quantitative interpretation of Pt L_2 and L_3 edge WL and XANES has been widely used to probe the unoccupied density of d states in a variety of systems [41–43].

To further elucidate the effect of composite supports on the activity of electrocatalysts, the chemical, electronic structures of the Pt nanostructures on the composite supports are studied using X-ray absorption spectroscopy.

XANES at the Pt L_3 and L_2 edges for the Pt nanoparticles deposited on the composite structures are shown in Figure 6.6 including a Pt foil, Pt/NCNTs and Pt/C for comparison. It is seen that both Pt L_3 and L_2 edge XANES of supported Pt nanoparticles exhibit a considerable whiteline (WL) compared to the Pt foil. The WL in Pt L_2 and L_3 edges arises from the dominant $2p_{1/2}$ and $2p_{3/2}$ transition to $5d_{3/2}$ and $5d_{5/2,3/2}$ resectively

(dipole selection rule: $\Delta l = \pm 1$, $\Delta j = \pm 1, 0$) indicating the presence of unoccupied densities of states of Pt $5d_{5/2}$ and $5d_{3/2}$ characters in the samples [41,42].
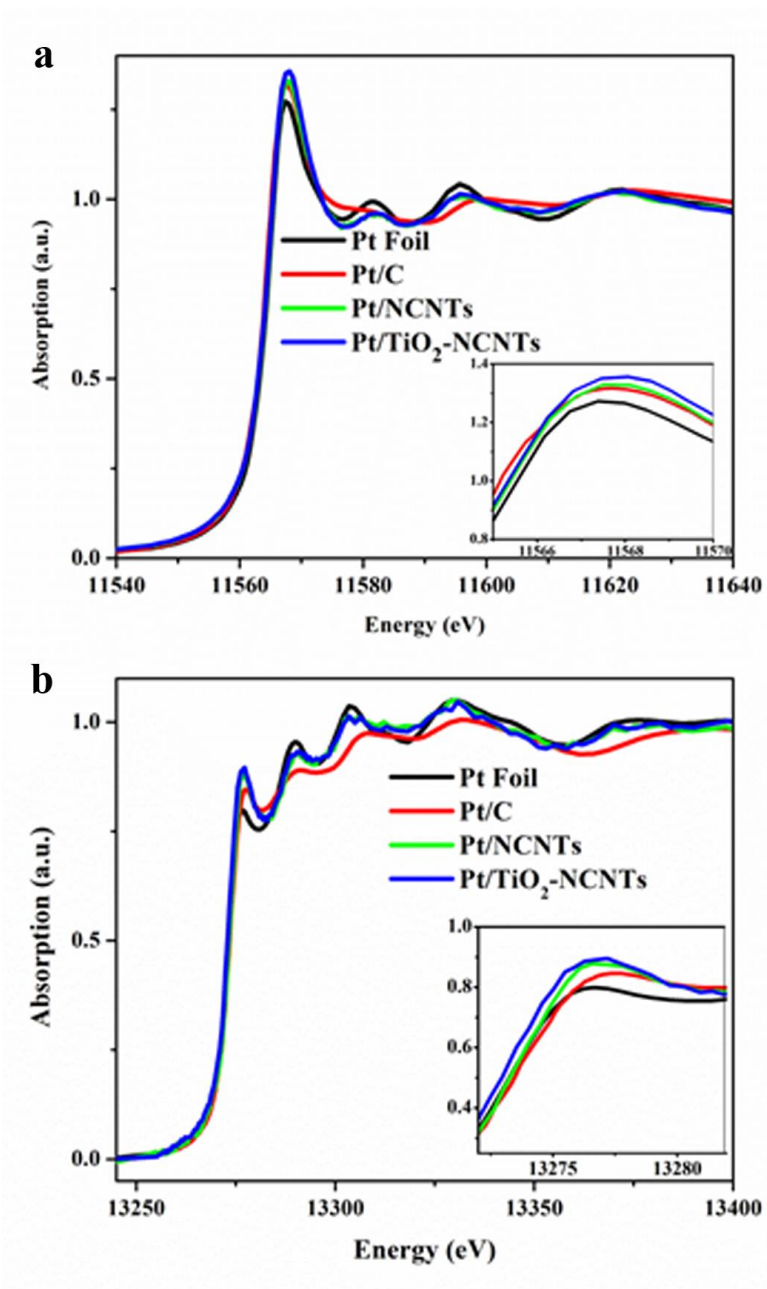
Figure 6.6 X-ray absorption studies of the Pt deposited composite nanostructures. The normalized XANES spectra at a) Pt L3 edge and b) Pt L2 edge.

A close examination of the L_3 edge WL profile of the composite samples indicate, there are small differences in the L_3 edge WL intensity of and shape. Results indicate that the L_3 edge WL intensity increases in the following order: Pt foil < Pt/C<Pt/NCNTs < Pt/TiO$_2$-NCNTs which are consistent with the ORR results of these electrocatalysts. All composite samples show a positive shift in the maximum energy (E_{peak}) with small negative shift in the threshold energy (E_o) (within experimental uncertainty). This indicates the Pt nanoparticles deposited on the composite supports are still metallic. The metallic behavior of these nanoparticles is also confirmed by the oscillations beyond the WL, which are characteristic of the FCC structure of Pt metal.

The increase in the WL intensity compared to Pt foil is due to decrease in the number of electrons in the d orbital, confirming a strong interaction between Pt nanoparticles and their support in the form of Pt atoms d charge depleted. The corresponding L_2 edge WL (Figure 6.6b), show a similar trend as that of Pt L_3 edge in E_{peak} and E_o.

For a better understanding of the effect of the unoccupied densities of 5d states of Pt nanoparticles on different supports, quantitative WL intensity analysis has been conducted based on method reported by Mansour et al.[43] and Sham et al. [41]. In this method, the Pt L_3 edge WL intensity is obtained by subtracting the Pt L_3 edge XANES from the corresponding XANES of Au. The area under the difference curve was integrated and ΔA_3 and ΔA_2 were calculated. These values can be expressed as:

$$\Delta A_3 = \int \mu(Pt)_{L_3WL} - \mu(Au)_{L_3WL}$$

$$\Delta A_2 = \int \mu(Pt)_{L_2WL} - \mu(Au)_{L_2WL}$$

and according to sham et al. [41] the theoretical expression of these value are:

$$\Delta A_3 = C_o N_o E_3 \left(R_d^{2p_{3/2}} \right)^2 \left[\frac{6h_{5/2} + h_{3/2}}{15} \right]$$

$$\Delta A_2 = C_o N_o E_2 \left(R_d^{2p_{1/2}} \right)^2 (\tfrac{1}{3} h_{3/2})$$

Where $C_o = 4\pi r^2 \alpha/3$ (α is the fine structure constant), N_0 the density of Pt atoms, h_j the 5d hole counts and E_2 and E_3 are the corresponding edge threshold, E_o for the L_2 and L_3 edges respectively. R term is the radial transition matrix element. By assuming R terms are similar for both edges:

$$C = C_o N_o R^2$$

and with this approximation:

$$h_{5/2} = \frac{1}{2C} \left[5 \frac{E_2}{E_3} \Delta A_3 - \Delta A_2 \right]$$

$$h_{3/2} = \left[\frac{3\Delta A_2}{C} \right]$$

A C value of 7.484×10^4 cm^{-1} was derived for Pt metal by Matthesis et al.[44]. Table 6.1 summarizes the Pt L_3 and Pt L_2 edge threshold and WL parameters. These results quantitatively confirm the observations made on the Pt L_3 edge XANES, i.e., Pt/TiO$_2$-NCNTs has the highest total unoccupied density of states of Pt 5d character compared to Pt/C indicating a stronger metal support interaction between the composite supports and Pt catalysts. Such an increase of 5d vacancies as reported by Toda et al.[34], leads to an increased 2π electron donation from O$_2$ to the surface of Pt, resulting in an increased O$_2$ adsorption and a weakening of the O-O bond. As a result, increasing the catalytic activity of Pt supported on TiO$_2$-NCNTs compared to Pt/NCNTs and Pt/C.

Table 6.1 Summary of WL analysis on Pt L3,2 edge of composite electrodes

Sample	Pt L$_3$ edge WL				Pt L$_2$ edge WL					
	E$_o$(eV)	E$_{Peak}$(eV)	Γ(eV)	ΔA$_3$	E$_o$(eV)	E$_{Peak}$(eV)	Γ(eV)	ΔA$_2$	h$_{5/2}$	h$_{3/2}$
Pt Foil	11564.00	11567.00	6.00	4.87	13273.00	13276.30	6.60	2.26	0.47	0.11
Pt/C	11564.00	11567.70	7.40	4.95	13272.99	13277.00	8.02	2.58	0.47	0.12
Pt/NCNTs	11563.98	11567.50	7.04	5.04	13272.98	13276.20	6.44	2.41	0.48	0.11
Pt/TiO2-NCNTs	11563.93	11567.80	7.74	5.44	13272.92	13276.90	7.96	2.73	0.52	0.13

6.4   Conclusion

In summary, TiO$_2$ nanoparticle decorated NCNTs were synthesized using a combination of CVD and magnetron sputtering. SEM and TEM observations reveal that the nanoparticles are single crystalline with an average diameter of 14 nm. Ti K-edge XAFS study indicates these nanoparticles have a rutile TiO$_2$ phase. Pt nanoparticles were deposited on these nanostructures. TEM investigations indicate the deposition of Pt on both TiO$_2$ and NCNTs surfaces. The electrochemical characterizations of the Pt/TiO$_2$-NCNTs revealed that the deposition of TiO$_2$ reduced the active surface area of Pt. However, results indicated a significant increase in the activity of Pt/TiO$_2$-NCNTs towards ORR and MOR. Furthermore, CO stripping voltammetry, revealed higher tolerance of these electrocatalysts to CO poising. XANES studies and WL analysis of the Pt L$_{2,3}$ edge reveal an increase in the Pt 5d vacancies of the Pt/TiO$_2$-NCNTs. These results illustrate a higher SMSI between the Pt catalysts and composite TiO$_2$-NCNTs supports. This opens up the possibility of fine tuning the electronic structure of Pt catalysts via composite catalyst supports.

6.5   References

[1]   Gong K, Du F, Xia Z, Durstock M and Dai L 2009 Science 323 760 –764

[2]   Elvington MC and Colon-Mercado HR 2012 Electrochemical and Solid-State Letters 15 K19–K22

[3]   Chen Z, Higgins D and Chen Z 2010 Electrochimica Acta 55 4799–4804

[4]   Chen Y, Wang J, Meng X, Zhong Y, Li R, Sun X, Ye S and Knights S 2011 International Journal of Hydrogen Energy 36 11085–11092

[5]   Chen Y 2009 Electrochemistry Communications 11 2071–2076

[6]   Selvarani G, Maheswari S, Sridhar P, Pitchumani S and Shukla AK 2009 Journal of Electrochemical Society 156 1354–1360

[7]   Saha MS, Li R, Sun X and Ye S 2009 Electrochemistry Communications 11 438–441

[8]   Zheng-Zhi Jiang, Da-Ming Gu, Zhen-Bo Wang, Wei-Li Qu, Ge-Ping Yin and Ke-Jian Qian 2011 Journal of Power Sources 196 8207–8215

[9]   Borup R et al. 2007 Chemical Reviews 107 3904–3951

[10]   Saha MS, Li R and Sun X 2008 Journal of Power Sources 177 314–322

[11]   Chen Y, Wang J, Liu H, Banis MN, Li R, Sun X, Sham T-K, Ye S and Knights S 2011 Journal of Physical Chemistry C 115 3769–3776

[12]   Chen Z, Higgins D, Tao H, Hsu RS and Chen Z 2009 Journal of Physical Chemistry C 113 21008–21013

[13]   Xiong C 2012 Journal of Power Sources 215 216–220

[14]   Saha MS, Banis MN, Zhang Y, Li R, Sun X, Cai M and Wagner FT 2009 Journal of Power Sources 192 330–335

[15]   Saha MS, Zhang Y, Cai M and Sun X 2012 International Journal of Hydrogen Energy 37 4633–4638

[16]   Lim D-H, Lee W-J, Macy NL and Smyrl WH 2009 Electrochemistry Solid-State Letter 12 123–125

[17]   Huang S-Y, Ganesan P and Popov BN 2011 Applied Catalysis B: Environmental 102 71–77

[18]   Bauer A, Lee K, Song C, Xie Y, Zhang J and Hui R 2010 Journal of Power Sources 195 3105–3110

[19]   Saha MS, Li R, Cai M and Sun X 2007 Electrochemistry Solid-State Letter 10 130–133

[20]   Antolini E 2010 Applied Catalysis B: Environmental 100 413–426

[21]   Antolini E and Gonzalez ER 2009 Solid State Ionics, Diffusion & Reactions 180 746–63

[22]   Eder D 2010 Chemical Reviews 110 1348–1385

[23]   von Kraemer S, Wikander K, Lindbergh G, Lundblad A and Palmqvist AEC 2008 Journal of Power Sources 180 185–190

[24]   Liu H, Zhang Y, Li R, Sun X, Désilets S, Abou-Rachid H, Jaidann M and Lussier L-S 2010 Carbon 48 1498–1507

[25]   Meng X, Zhong Y, Sun Y, Banis MN, Li R and Sun X 2011 Carbon 49 1133–1144

[26]   Yang D-Q, Sun S, Dodelet J-P and Sacher E 2008 The Journal of Physical Chemistry C 112 11717–11721

[27]   Yao N Microporous and Mesoporous Materials 44-45 377–384

[28]   Sun S, Jaouen F and Dodelet J 2008 Advanced Materials 20 3900–3904

[29]   Sun S, Zhang G, Geng D, Chen Y, Banis MN, Li R, Cai M and Sun X 2010 Chemistry - A European Journal 16 829–835

[30]   Chang S-H, Su W-N, Yeh M-H, Pan C-J, Yu K-L, Liu D-G, Lee J-F and Hwang B-J 2010 Chemistry – A European Journal 16 11064–11071

[31]   Colmenares JC, Magdziarz A, Aramendia MA, Marinas A, Marinas JM, Urbano FJ and Navio JA 2011 Catalysis Communications 16 1–6

[32]   Ocal C and Ferrer S 1986 Journal of Chemical Physics 84 6474–6478

[33]   Zhang J, Vukmirovic MB, Xu Y, Mavrikakis M and Adzic RR 2005 Angewandte Chemie 117 2170–2173

[34]   Toda T, Igarashi H, Uchida H and Watanabe M 1999 Journal of Electrochemical Society 146 3750–3756

[35]   Min M-K, Cho J, Cho K and Kim H 2000 Electrochimica Acta 45 4211–4217

[36]   Lima F, Zhang J, Shao M, Sasaki K, Vukmirovic M, Ticianelli E and Adzic R 2008 Journal of Solid State Electrochemistry 12 399–407

[37]   Akalework NG, Pan C-J, Su W-N, Rick J, Tsai M-C, Lee J-F, Lin J-M, Tsai L-D and Hwang B-J 2012 Journal of Materials Chemistry 22 20977-20985

[38]   Zhou J Chemical Physics Letters 437 229–232

[39]   Boyanov BI and Morrison TI 1996 Journal of Physical Chemistry 100 16318–16326

[40]   Jia J, Kou Y, Lin L, Xu Z, Zhang T, Niu J and Liang D 1998 Reaction Kinetics and Catalysis Letters 63 391–396

[41]   Sham TK, Naftel SJ and Coulthard I 1996 Journal of Applied Physics 79 7134–7138

[42]   Brown M, Peierls RE and Stern EA 1977 Physical Review B 15 738–744

[43]   Mansour AN, Cook JW and Sayers DE 1984 Journal of Physical Chemistry 88 2330–2334

[44]   Mattheiss LF and Dietz RE 1980 Physical Reviews B 22 1663–1676

Chapter 7

7 One-step tunable synthesis of pristine, sulfur-doped $W_{18}O_{49}$ nanowires and $WS_2/W_{18}O_{49}$ nanocables[1,2]

There is a growing trend of studies on the deposition of Pt catalysts on tungsten oxide nanostructures ($W_{18}O_{49}$) owing to their high electrochemical stability and good electrical conductivity, which promises improved catalytic activity and stability of the electrocatalysts compared to commercial Pt/C catalyst. Recently, our group along with other research groups have reported that $W_{18}O_{49}$ supported Pt catalysts show high electrocatalytic activity towards oxygen reduction reactions, thus enhancing the fuel cell performance.

Following this concept, to increase the Pt utilization and forming freestanding electrocatalysts of Pt on $W_{18}O_{49}$ catalyst support, our research efforts have been expanded to controlled synthesis of tungsten oxide nanowires directly from tungsten powder. The advantages of these studies is the synthesis of tungsten oxide nanowires with small diameters and larger specific surface area, higher gas permeability and modification of their surface chemistry for better Pt catalyst deposition and metal support interaction. In addition, sulfur doping has been introduced in the tungsten oxide nanowires to modulate the morphology and size of the nanowires and create complex architecture of $WS_2/W_{18}O_{49}$ nanocables as well, which may display distinct catalytic properties.

---

[1] Yong Zhang, Ruying Li, and Xueliang Sun

Department of Mechanical and Materials Engineering, The University of Western Ontario, London, Ontario N6A 5B9 (Canada)
E-mail:xsun@eng.uwo.ca

7.1   Introduction

One dimensional nanostructures have become the focus of considerable research due to their intriguing properties, high surface to volume ratios and potential applications in various technologies and high performance nanoscale devices. Among which, tungsten based nanostructures such as tungsten oxides (WO_{3-x}) and tungsten sulfides (WS_2) are of particular interest. WO_{3-x} nanostructures have been found to exhibit semiconductor, conductor or superconductor properties depending on their oxidization states [1]. The properties and imperfection in the structure of nonstoichiometric tungsten oxides has led to their application in gas sensors, optical devices [2] solar cell energy conversion, photoelectrochromatic applications [3] and field emission technologies [1]. Tungsten oxides nanostructures such as $W_{18}O_{49}$ nanowires have been proposed as catalysts supports in low temperature fuel cells in enhancing the catalytic activity of the electrocatalyst [4,5].

WS_2 nanotubes were the first artificial non-carbon nanotubes since the discovery of carbon nanotubes in 1992. It was shown that these nanostructures have a layered structure and are unstable in the planar form and they fold on themselves giving rise to polyhedral fullerene like structures and nanotubes. The properties of these nanostructures have been intensively investigated in recent years. WS_2 nanotubes are promising material for solid state lubricants[6], tips of scanning electron microscopes [7] and applications such as solar cells [8], Li ion batteries [9], photodetectors [8]. Studies have also shown that hybrid nanostructures of WS_2/WO_{3-x} show excellent mechanical properties making them suitable as shock resistant material [10].

Various strategies have been adapted for the preparation of WO_{3-x} nanostructures including solvothermal synthesis [11], thermal evaporation [12] and vapor deposition [13–15]. Among these methods, synthesis of WO_{3-x} nanostructures such as $W_{18}O_{49}$ nanowires using vapor deposition of tungsten metal in the presence of water vapor is the most promising method for large scale synthesis of these nanostructures [13].

Furthermore, $W_{18}O_{49}$ nanostructures can be subsequently used as precursors of WS_2 nanotubes via direct metathesis reaction with gaseous H_2/H_2S in two step process [16].

However, several key issues have to be addressed prior to implementation of these nanostructures in their prospective applications. The main challenge is the synthesis of the nanostructures with tunable morphology which promises adjustable properties of the corresponding nanodevices. Studies have shown that the morphology of the nanostructures can be manipulated by the introduction of a foreign element into their crystal structure, which is so-called doping [17–19]. Zhai et al [19], have reported the synthesis of various morphologies of In_2Se_3 nanostructures via sulfur doping.

Up to now, many different factors have been studied for the controlled growth of WO_{3-x} nanowires and subsequently WS_2 nanotube. Here, we report a one-step tunable synthesis of pristine, sulfur-doped $W_{18}O_{49}$ nanowires and $WS_2/W_{18}O_{49}$ nanocables by controlled sulfur doping, and structure evolution of the products was investigated.

7.2 Experimental Details

The pristine and sulfur-doped $W_{18}O_{49}$ nanowires as well as $WS_2/W_{18}O_{49}$ nanocables were grown via a chemical vapor deposition method using tungsten powder (99%, Aldrich) as the source material and high purity Ar as the carrier gas. Sulfur powder (99%, Aldrich) was added to the system for the synthesis of S-doped $W_{18}O_{49}$ nanostructures and $WS_2/W_{18}O_{49}$ nanocables. Tungsten powder was placed in center of the tube furnace, which acted as both tungsten source and the substrate. Sulfur powder was positioned in the upstream region of the furnace. Prior to heating the furnace, the chamber was saturated with water vapor by introducing high purity Ar, passed through a water bubbler, into the synthesis chamber for 30min at a rate of 300sccm (standard cubic centimeters per minute). The system was rapidly heated to $750^{o}C$ over 15 min and kept at this temperature for 60min at a constant flow of water vapor saturated Ar. After the experiment the system was cooled down to room temperature slowly.

The product collected from the tungsten powder was characterized initially using a Hitachi S-4800 field emission scanning electron microscope (SEM) operated at 5.0 kV and Philips CM10 transmission electron microscope (TEM). Further detailed characterization was conducted by a JEOL 2010 field emission gun high resolution transmission electron microscope (HRTEM) operated at 200kV and energy dispersive X-ray spectrometer (EDX).

7.3   Results and Discussion

Tungsten based one dimensional nanostructures were synthesized using vapor deposition method. In this process the morphology of nanostructures was controlled by adjusting the concentration of sulfur vapor in the CVD chamber.

Figure 7.1 shows typical SEM images of nanostructures synthesized from tungsten powder under various sulfur vapor flow rates. SEM images of nanostructures synthesized in the absence of sulfur vapor in the chamber are shown in Figure 7.1a and b, similar morphologies to tungsten oxide nanostructures have been previously reported [13,20]. SEM observations indicate these nanostructures have length up to few micrometers, and a wide range of diameters between 50 nm to 700 nm. The close examination of the large $W_{18}O_{49}$ nanostructures shown in Figure 7.1b, clearly shows the presence of thinner nanowires on the edges of $W_{18}O_{49}$ nanostructures. As reported by Gu et al. [13], these nanostructures are composed of bundle of smaller diameter $W_{18}O_{49}$ nanowires growing in the same crystal direction. Each component of these thinner nanowires has an average diameter of 20 nm. Furthermore, hollow like feature is formed in the composite nanostructure, due to multi-component structure of the $W_{18}O_{49}$ nanowire bundle. SEM observations indicate that more than 90% of the tungsten powder is converted into $W_{18}O_{49}$ nanostructure bundles.
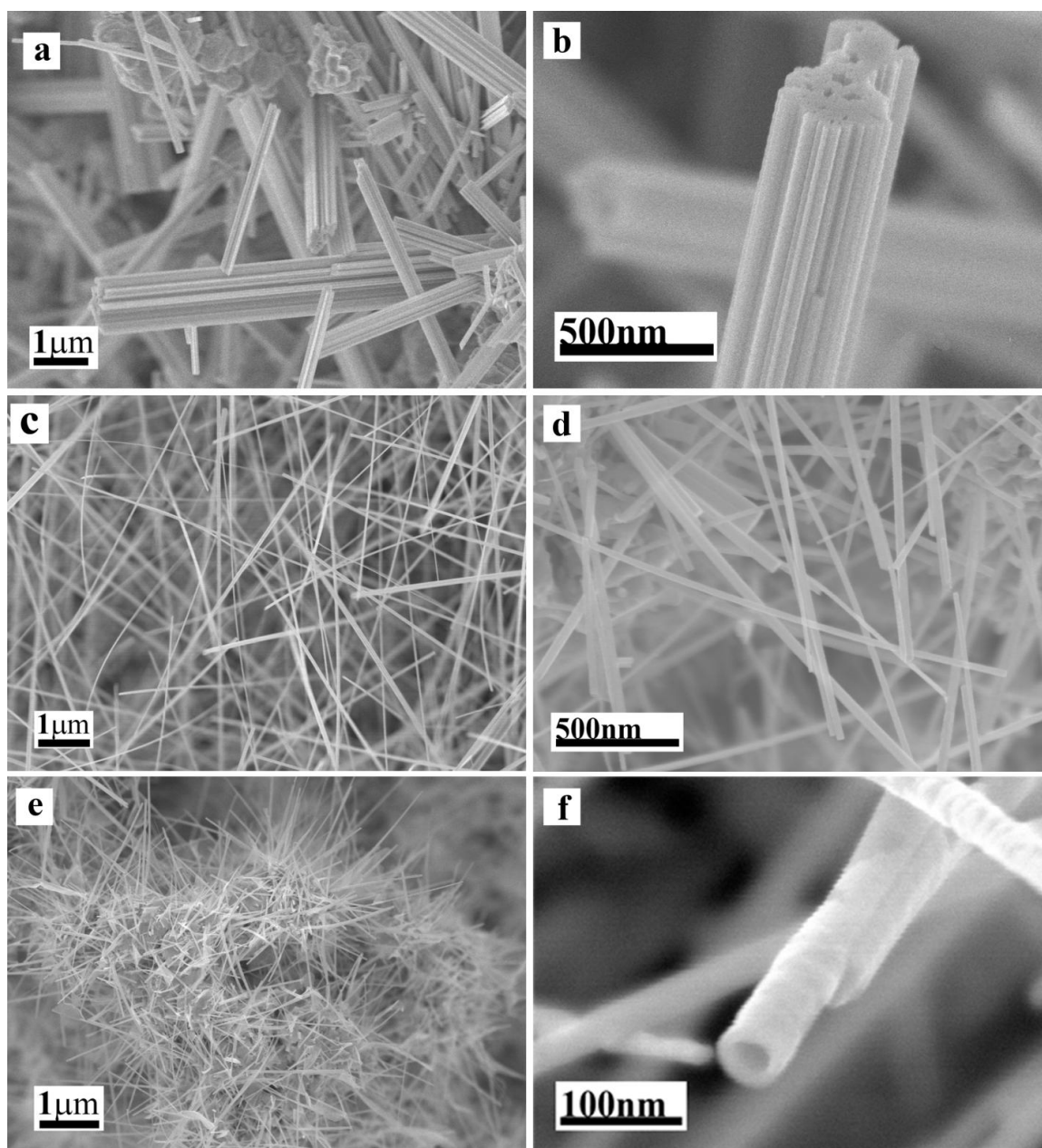
Figure 7.1 SEM images of a,b) W$_{18}$O$_{49}$ nanowire bundles, c,d) S-W$_{18}$O$_{49}$(60) nanowires, e,f) S-W$_{18}$O$_{49}$(150) nanocables.

After addition of sulfur vapor into the synthesis process, striking changes were observed in the morphology of W$_{18}$O$_{49}$ nanostructures. SEM images of products formed under

60mgh^{-1} sulfur flow rate (S-W$_{18}$O$_{49}$(60), Figure 7.1c and d), show high density of nanowires formed on tungsten powder. These nanowires have uniform and thinner diameters compared to pristine W$_{18}$O$_{49}$ nanostructures (Figure 7.1b), with an average diameter of 35 nm and length up to 5 µm. High magnification image of individual S-W$_{18}$O$_{49}$(60) nanostructures shown in Figure 7.1d, illustrates that these nanostructures are composed of smaller number of W$_{18}$O$_{49}$ nanowires.

With further increase of sulfur vapor flow rate to 150mgh^{-1} (S-W$_{18}$O$_{49}$(150)) , significant decrease in the density and length of nanostructures deposited on tungsten powder is observed (Figure 7.1e). SEM observations reveal that by increasing the sulfur flow rate, the rate of tungsten powder conversion to tungsten based nanostructures is decreased. However, no obvious change in the diameter of these nanostructures compared to S-W$_{18}$O$_{49}$(60) nanostructures could be seen. High magnification SEM images of S-W$_{18}$O$_{49}$(150) shown in Figure 7.1f, indicate the presence of open ended nanostructures on tungsten powder, implying the formation of tube like structures. SEM observations show, that further increase of the sulfur vapor flow rate in the synthesis process reduces the overall density of tungsten based nanostructures but increase the ratio of tube like nanostructures to nanowires.

To further analyze the composition and structure of the products EDX analysis under TEM was carried out. Figure 7.2a shows a typical image of W$_{18}$O$_{49}$ nanowire bundles. As seen in TEM images, these nanostructures have a wide range of diameters and lengths and the composite nature of these nanostructures can clearly identified. EDX spectrum of W$_{18}$O$_{49}$ (Figure 7.2b) nanostructures shows the presence of tungsten and oxygen as the main components of these nanostructures. The Cu peaks result from the TEM grid holding the nanostructures. TEM images of S-W$_{18}$O$_{49}$ (60) nanostructures (Figure 7.2c), confirm the SEM observation results, indicating a uniform diameter distribution of S-W$_{18}$O$_{49}$(60) nanostructures compared to W$_{18}$O$_{49}$ nanostructures resulting from the presence of sulfur in the synthesis chamber. EDX spectrum of these nanostructures (Figure 7.2d) reveals the presence of small amount of sulfur in addition to tungsten and

oxygen peaks. Figure 7.2e, shows the TEM image of S-$W_{18}O_{49}$(150) nanostructures, revealing their core/shell structure. As shown in TEM images, these nanocables have open ended structure with inner diameters between 11 nm and 40 nm and outer diameter of 20 nm to 45 nm. EDX analysis of S-$W_{18}O_{49}$(150) nanocables indicate the higher atomic ratio of sulfur compared to S-$W_{18}O_{49}$(60) nanostructures.
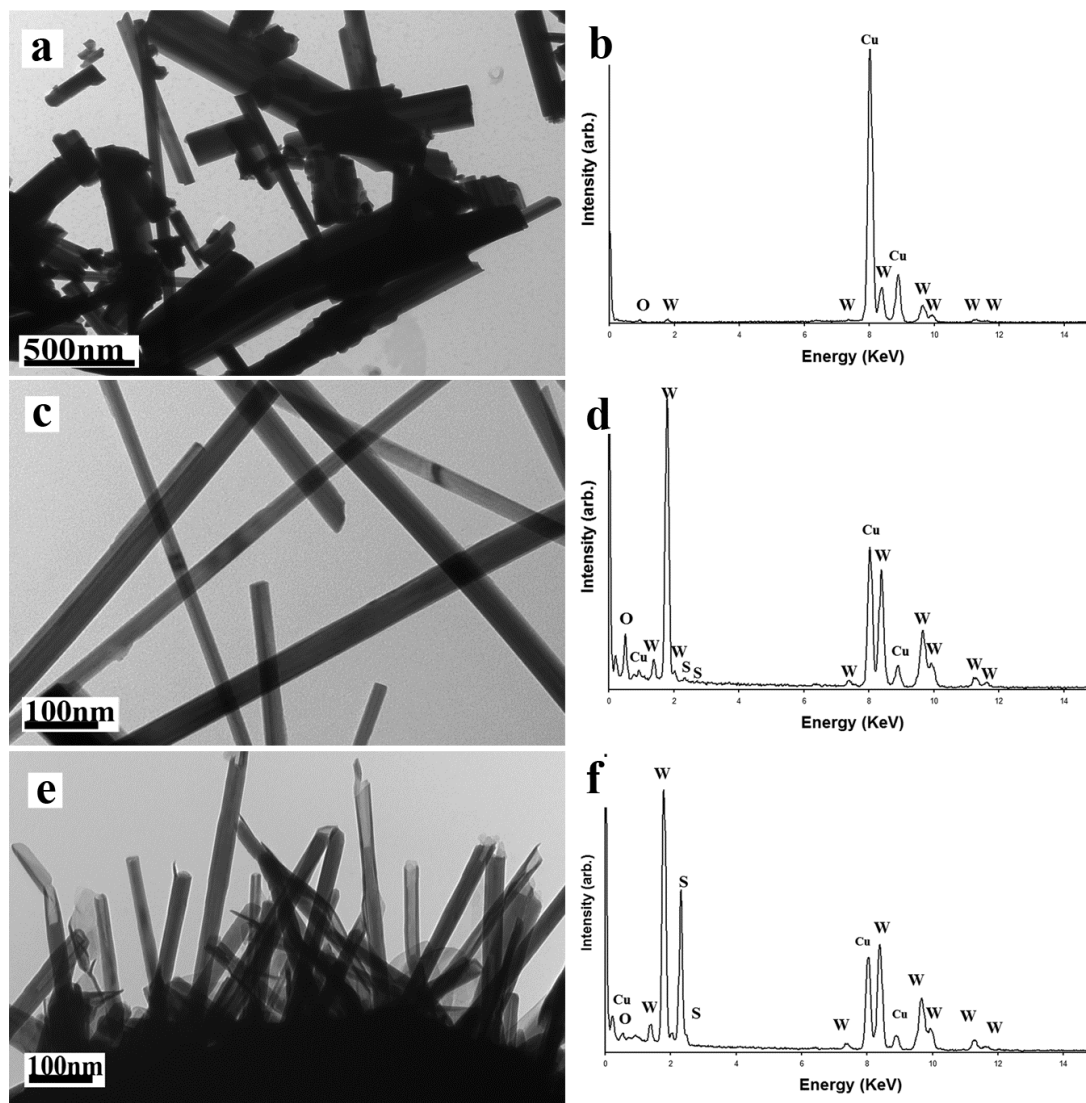

Figure 7.2 TEM images and EDX spectrum of a,b) $W_{18}O_{49}$ nanowire bundles, c,d) S-$W_{18}O_{49}$(60) nanowires, e,f) S-$W_{18}O_{49}$(150) nanocables.

The HRTEM analysis was used to study the crystal structure of deposited nanostructures in detail. HRTEM image of $W_{18}O_{49}$ composite nanowires shown in figure 7.3a, reveal that each nanowire of the nanostructure bundle is a single crystal. Selected area electron diffraction pattern (support information 1a) confirms the monoclinic $W_{18}O_{49}$ crystal structure of the nanowires. As shown in Figure 7.3b, the nanowires in the nanostructure bundle grow perpendicularly to {010} plane which is the close packed plane of the crystalline monoclinic $W_{18}O_{49}$. HRTEM image of S-$W_{18}O_{49}$(60) nanowires shown in Figure 7.3c, reveals a similar structure to $W_{18}O_{49}$ nanostructure bundles, with the distance of core lattice fringes corresponding to (010) plane of $W_{18}O_{49}$ crystal structure (Figure 7.3c, lower inset) . However, detailed measurement of distance between lattice fringes at the edge of the nanowires (Figure 7.3c, top inset) indicates a small increase in distance compared to the core of nanowires. This increase can be related to diffusion of another element such as sulfur, replacing the oxygen in the $W_{18}O_{49}$ monoclinic crystal structure, as illustrated in Figure 7.3d.

The HRTEM observation of the nanocables S-$W_{18}O_{49}$(150) nanostructures, shown in Figure 5.3e, clearly reveal the presence of crystalline core covered by multi walled crystalline shell. HRTEM observations indicate that the number of walls in the shell section of the nanocables is between 4 and 16. Further detailed study of the core section (Figure 7.3e, lower inset) indicates this section to have a crystalline $W_{18}O_{49}$ structure similar to $W_{18}O_{49}$ nanocomposites, growing in [010] crystal direction. The HRTEM image of the shell area (Figure 7.3e, top inset), the formation of the nanotubes around $W_{18}O_{49}$ core nanowires. The distance the nanowalls correspond to (0002) planes of WS_2 hexagonal crystal structures grown along [10$\bar{1}$0] direction. Figure 7.3f, shows the relaxed atomic model of 2H-WS_2 covering the $W_{18}O_{49}$ nanowires.
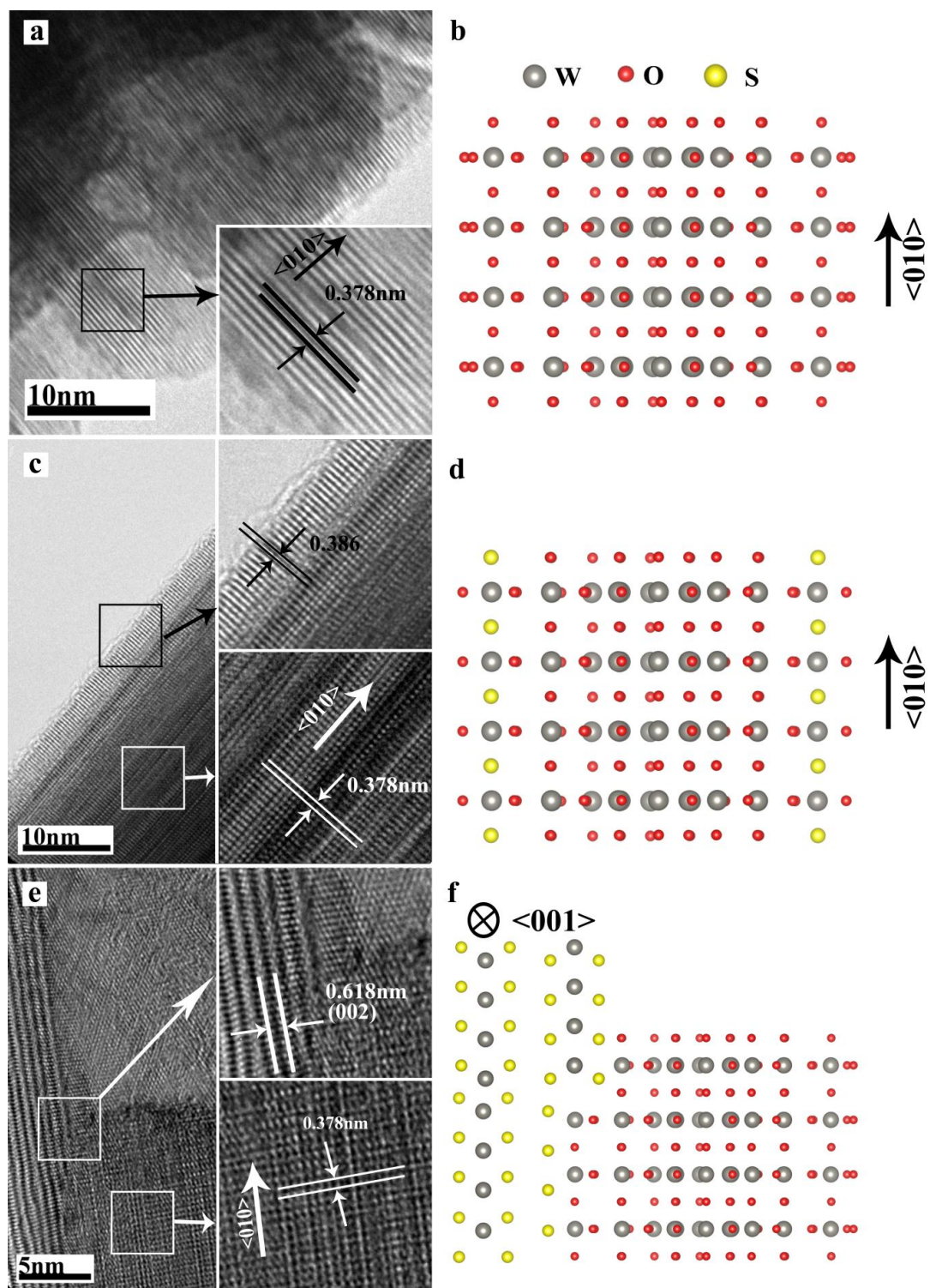
Figure 7.3 HRTEM and relaxed atomic models of W$_{18}$O$_{49}$ nanowire bundles, c,d) S-W$_{18}$O$_{49}$(60) nanowires, e,f) S-W$_{18}$O$_{49}$(150) nanocables.

In the synthesis of $W_{18}O_{49}$ nanostructures, since no catalyst was used, vapor-solid mechanism can be proposed for their synthesis process. In this process as described in previous studies [13,14,20], water vapor plays a key role in the formation of $W_{18}O_{49}$ nanostructures at relatively low temperature. Based on the experimental results, the synthesis of $W_{18}O_{49}$ nanocomposites can result from following reactions:

$$W + H_2O \rightarrow WO_x + H_2$$

$$WO_x + nH_2O \rightarrow WO_x.nH_2O$$

$$WO_x.nH_2O + H_2 \rightarrow W_{18}O_{49} + H_2O$$
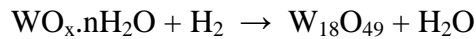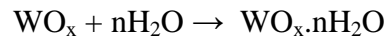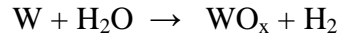
This process has been well reported [13,14,20]. In this mechanism, first a thin WO_x layer is formed on the surface of W powder. The volatile tungsten compound ($WO_x.nH_2O$) is formed from this surface layer via reaction with water. During the experiment, by further oxidation of the W powder, the vapor pressure of $WO_x.nH_2O$ is increased on the surface of the source powder. The supersaturation and decomposition of $WO_x.nH_2O$ on the surface of the W powder, leads to the formation of $W_{18}O_{49}$ crystal nuclei. The continuous decomposition of volatile $WOx.nH_2O$ on the nuclei, allows the formation of the crystalline $W_{18}O_{49}$ nanowires along [010] direction away from the tungsten powder. Further decomposition of $WO_x.nH_2O$ from gas phase, as seen in the SEM and TEM observations will facilitate the growth of secondary single nanowires parallel to the first nanowire forming nanostructure bundles with larger diameters. Studies have shown that various parameters such as the size of tungsten precursor, water vapor pressure affect the overall diameter and morphology of the synthesized nanostructures [13,16]. However, as reported by Jin et al.[13], the vapor-solid process of the formation of $W_{18}O_{49}$ on the surface of the $W_{18}O_{49}$ initial nanowire plays a key role in the synthesis of the nanostructure bundles. In this process, surface properties of the substrate (walls of $W_{18}O_{49}$ initial nanowire in this case,) affect the deposition rate and growth of nanostructures.

By introduction of sulfur into the synthesis process, as seen in TEM observations the surface structure of the $W_{18}O_{49}$ nanowires changes. As shown in Figure 7.3c and d, we believe the diffusion of sulfur between the (010) planes of monoclinic $W_{18}O_{49}$ crystal increases their inter-planner distances on the surface of the nanowires. This increase results in change in local chemistry and surface energy of nanowires surfaces. Consequently, affecting their adsorption properties for the volatile $WO_x.nH_2O$ species, and inhibiting the formation of composite nanowires with large diameters.

Experimental results indicate the diameter of the $W_{18}O_{49}$ nanowires before the formation of nanocables is dependent on the sulfur vapor pressure in the CVD chamber. This can be related to the diffusion rate of sulfur in the $W_{18}O_{49}$ crystal structure.

The formation of WS_2 nanotubes around $W_{18}O_{49}$ nanowires has been extensively reported [10,16,21−23]. In these studies, the synthesis is reported in two stage experiments: 1) Synthesis of WO_x nanostructures (mostly whiskers [16,21] or nanorods [10,22]), 2) conversation of WO_x nanostructures into WS_2 nanotubes. According to these studies, H_2 is diffused into WO_x structures, forming oxygen vacancies in the structure by forming H_2O and reducing the structure to tungsten suboxides such as $W_{18}O_{49}$ [21,22]. In the next stage, following the oxide to sulfide mechanism, $WS_2/W_{18}O_{49}$ nanocables are formed via H_2S reaction. In this mechanism, sulfur diffuses into the surface of the $W_{18}O_{49}$ nanostructures forming a sulfide skin around the oxide core. Subsequent sulfur gradually proceeds inward forming the inner layers.

In this study, we believe the reported two stages occur simultaneously with synthesis of $W_{18}O_{49}$ nanowires and gradual conversion toWS_2, due to diffusion controlled process of the latter reaction. Furthermore, the presence of H_2O vapor and synthesis of $W_{18}O_{49}$ suboxides with sufficient oxygen vacancies and diffusion pathways, eliminates the need for the introduction of external H_2 gas into the synthesis chamber.

It is noteworthy that in contrast to the most reported WS_2 [16,21] from a WO_x precursor, our results show the formation of long, and mainly open ended nanotubes. We believe

this feature arises from typical morphology of $W_{18}O_{49}$ nanowires and the sulfur diffusion pathways. As shown in Figure 7.3b and d, $W_{18}O_{49}$ nanowires are synthesized along [010] direction in the close packed plane of the monoclinic crystal structure. This reduces the diffusion of sulfur into the $W_{18}O_{49}$ crystal structure in [010] direction thus forming open ended nanotubes.

Furthermore, the radial diffusion of sulfur through WS_2 is thought to be very slow so as proposed previously [22], sulfur diffusion occurs along the nanowalls of WS_2 nanotubes to reach the $W_{18}O_{49}$ crystal structure and diffuse radially. This will result into gradual inward radial conversion of the core section of nanocables from their tip as highlighted in Figure 7.3e.

7.4   Conclusion

In summary, $W_{18}O_{49}$ nanowires with well determined diameters were synthesized directly on tungsten powder. The morphology of these nanowires was controlled by sulfur doping of their surface crystal planes, via exposing to sulfur containing vapor. Experimental results indicated the change in the surface properties of the $W_{18}O_{49}$ nanowires inhibits the formation of nanostructure bundles with large diameters. Further increase of sulfur vapor flow rate resulted in the one-step synthesis of open ended, long $WS_2/W_{18}O_{49}$ nanocables. The growth process of these hybrid materials is based on the vapor solid mechanism, and diffusion of sulfur vapor along the WS_2 nanowalls and radial diffusion in $W_{18}O_{49}$ crystal structure. It has been shown that the extent of oxide to sulfide conversion can be controlled with sulfur concentration in the CVD chamber. This method has great potential for large scale synthesis of $W_{18}O_{49}$ nanowires and $WS_2/W_{18}O_{49}$ nanocables with uniform size distribution. These materials have great potential in various applications such as catalyst support, field emitters and energy industries.

7.5   References

[1]   Yue S, Xu T, Li W, Yan J and Yi H 2012 Journal of Semiconductors 33 063002-063006

[2]   Xiao Z, Zhang L, Tian X and Fang X 2005 Nanotechnology 16 2647–2650

[3]   Hsieh YT, Chen US, Hsueh SH, Huang MW and Shih HC 2011 Applied Surface Science 257 3504–3509

[4]   Saha MS, Banis MN, Zhang Y, Li R, Sun X, Cai M and Wagner FT 2009 Journal of Power Sources 192 330–335

[5]   Saha MS, Zhang Y, Cai M and Sun X 2012 International Journal of Hydrogen Energy 37 4633–4638

[6]   Rapoport L, Bilik Y, Feldman Y, Homyonfer M, Cohen SR and Tenne R 1997 Nature 387 791–793

[7]   Rothschild A, Cohen SR and Tenne R 1999 Applied Physics Letters 75 4025–4027

[8]   Zhang C et al. 2012 Applied Physics Letters 100 243101–243106

[9]   Feng C, Huang L, Guo Z and Liu H 2007 Electrochemistry Communications 9 119–122

[10]   Remskar M, Virsek M and Jesih A 2008 Nano Letters 8 76–80

[11]   Yoo SJ, Lim JW, Sung Y-E, Jung YH, Choi HG and Kim DK 2007 Applied Physics Letters 90 173126–173129

[12]   Huang K, Pan Q, Yang F, Ni S and He D 2007 Physica E: Low-dimensional Systems and Nanostructures 39 219–222

[13]   Jin YZ, Zhu YQ, Whitby RLD, Yao NN, Renzhi M, Watts PCP, Kroto HW and Walton DRM 2004 Journal of Physical Chemistry B 108 15572–15577

[14]   Zhang Y, Chen Y, Liu H, Zhou Y, Li R, Cai M and Sun X 2009 Journal of Physical Chemistry C 113 1746–1750

[15]   Zhou Y, Zhang Y, Li R, Cai M and Sun X 2009 Journal of Materials Research 24 1833–1841

[16]   Rothschild A, Sloan J and Tenne R 2000 Journal of the American Chemical Society 122 5169–5179

[17]   Wirths S et al. 2011 Journal of Applied Physics 110 053709–053717

[18]   Yan J-F 2011 Chinese Physics B 20 048102-048106

[19]   Zhai T, Ma Y, Li L, Fang X, Liao M, Koide Y, Yao J, Bando Y and Golberg D 2010 Journal of Materials Chemistry 20 6630-6637

[20]   Gu G, Zheng B, Han WQ, Roth S and Liu J 2002 Nano Lett. 2 849–851

[21]   Rothschild A, Frey GL, Homyonfer M, Tenne R and Rappaport M 1999 Materials Research Innovations 3 145–149

[22]   Li Y-H, Zhao YM, Ma RZ, Zhu YQ, Fisher N, Jin YZ and Zhang XP 2006 Journal of Physical Chemistry B 110 18191–18195

[23]   Chen J, Li S-L, Gao F and Tao Z-L 2003 Chemistry of Materials 15 1012–1019

Chapter 8

8   Conclusion and Future Perspective

8.1   Conclusion

Nanomaterials, material with at least one dimension in nanoscale, have been extensively studied, due to their unique structure and properties. These materials have been applied in many applications such as fuel cells to address their challenges. Fuel cells, specifically proton exchange membrane fuel cells (PEMFCs), are one of the environmentally friendly energy systems that offer the direct conversion of chemical energy to electricity with high efficiency. However, the high cost of Pt used as catalyst is a big roadblock inhibiting the wide scale commercialization of PEMFCs. The application of nanomaterials with controlled morphology has been shown as a promising solution to address the challenges in the field of PEMFCs.

The main objective of this thesis has been the development of various novel nanomaterials as catalyst support of Pt electrocatalysts to improve the PEMFCs performance. The synthesis process and growth mechanism of these nanomaterials have been studied in detail. The morphology, structure and properties of the nanostructured catalyst supports have been characterized via various techniques such as scanning and transmission electron microscopy, X-ray diffraction, energy dispersive X-ray spectroscopy, Raman spectroscopy and X-ray absorption spectroscopy. Electrochemical characterization of the nanostructures has been conducted to study the performance of these supports with Pt catalysts in PEMFCs environment.

Metal silicides are potential candidates as catalyst supports in PEMFCs due to their unique properties such as high electrical conductivity, high corrosion and oxidation resistance. In this thesis, WSi_2 nanostructures were synthesized using a low pressure

CVD method. The results indicated that the concentration changes of the tungsten precursor and partial pressure of oxygen affected the morphology and composition of the products, forming nanowires, nanonets and nanosheets. The growth mechanism was proposed based on the formation of a silica sheath on several (111) planes of WSi_2 nuclei. The nanostructures were formed in three stages: i) forming nanoparticles, ii) growing into nanonets and iii) evolving to nanosheets. Cyclic voltammetry measurements of the nanostructures indicate that WSi_2 nanosheets exhibited higher capacitance compared to WSi_2 nanoribbons.

Ta_5Si_3 complex nanostructures were also synthesized via low pressure CVD process. The experimental results indicated that the morphology of nanostructures is very sensitive to precursor and silica vapor pressure along the CVD chamber. The networked nanowires were synthesized in high precursor and silica concentration while networked nanoribbons and nanosheets were grown in lower concentration region. A vapor solid mechanism based on the formation of silica sheath on {001} crystal planes of Ta_5Si_3 nanostructures was proposed. Cyclic voltammetry measurements of Ta_5Si_3 nanostructures with different morphologies indicated that networked nanoribbons and nanosheets exhibit higher capacitance compared to other morphologies. These nanostructures are expected to be great potential material for new electronic and energy related applications.

The nanostructured $TiSi_2O_x$-NCNTs composites were synthesized as support of Pt catalysts for PEMFC applications. The nanostructures were synthesized using a combination of CVD and magnetron sputtering processes. The experimental results showed that $TiSi_2O_x$ formed an amorphous layer with variable thickness on carbon nanotubes. Annealing treatment of the composite nanostructures promoted the formation of TiO_2 nanocrystals in the amorphous $TiSi_2O_x$ matrix. X-ray absorption near edge structure (XANES) spectra of Ti K-edge and Si K-edge confirmed the presence of rutile TiO_2 and SiO_2 in the sputtered layer. Pt was deposited on the composite nanostructures via reduction method. The electrochemical characterization of Pt deposited catalysts supports indicated that the Pt/An-$TiSi_2O_x$-NCNTs exhibited 30mV positive potential and

larger mass and specific activity for oxygen reduction reaction (ORR) compared to Pt/TiSi$_2$O$_x$-NCNTs and Pt/NCNTs. The quantitative and qualitative analysis of whiteline in XANES spectra of Pt L$_2$ edge and Pt L$_3$ edge confirmed the presence of higher density of unoccupied states in Pt 5d orbitals for Pt nanoparticles deposited on composite catalyst supports compared to NCNTs, resulting in the higher catalytic activity of these catalysts. The higher performance of *An*-TiSi$_2$O$_x$-NCNTs relative to TiSi$_2$O$_x$ is attributed to the change in the morphology of Pt nanoparticles deposited on these composite nanostructures and the synergistic effect between Pt, SiO$_x$ and TiO$_2$ species on the annealed TiSi$_2$O$_x$ layer. These results suggest that multi component composite nanostructures are promising catalyst supports for PEMFC applications.

Further, in the next step TiO$_2$ nanoparticle decorated NCNTs were synthesized by removal of SiO$_2$ amorphous layer in *An*-TiSi$_2$O$_x$-NCNTs. SEM and TEM observations reveal the presence TiO$_2$ nanoparticles with diameters around 14nm. XANES spectra of Ti K edge confirmed the rutile nature of these nanoparticles. Pt nanoparticles were deposited on the composite nanostructures. Electrochemical characterization of Pt/TiO$_2$-NCNTs revealed a significant increase in the activity of these composite electrocatalysts towards ORR and methanol oxidation. In addition, CO stripping voltammetry revealed higher tolerance of these electrocatalysts to CO poising compared to Pt/NCNTs and Pt/C. XANES spectra of Pt L$_2$ and L$_3$ edge illustrated the increase in the density of unoccupied density of states in Pt 5d orbitals with the presence of TiO$_2$ nanoparticles. These results indicate a strong metal support interaction between Pt catalysts and TiO$_2$-NCNTs supports. This opens up the possibility of fine tuning the electronic structure of Pt catalysts via composite catalyst supports.

The synthesis of W$_{18}$O$_{49}$ nanowires and WS$_2$/W$_{18}$O$_{49}$ nanocables were studied. W$_{18}$O$_{49}$ nanowires were synthesized using a chemical vapor deposition (CVD) method. The morphology of nanostructures deposited on tungsten powder was controlled by sulfur doping of the W$_{18}$O$_{49}$ nanowires via exposing to sulfur containing vapor. The experimental results indicated that the change in the surface properties of tungsten oxide

nanowires enables the synthesis of $W_{18}O_{49}$ nanowires with smaller diameters (~20 nm). Further increase of sulfur vapor flow rate resulted in the one step synthesis of open ended long $WS_2/W_{18}O_{49}$ nanocables. A vapor solid mechanism was proposed for the growth of these nanowires and nanocables. It was proposed that the transformation of $W_{18}O_{49}$ to WS_2 is based on the diffusion of sulfur along WS_2 nanowalls and radial diffusion in $W_{18}O_{49}$ crystal structure. The results indicated that the rate of tungsten oxide to sulfide conversion can be controlled by the sulfur concentration in the CVD chamber. This method has a great potential for large scale synthesis of $W_{18}O_{49}$ nanowires $WS_2/W_{18}O_{49}$ nanocables with controlled morphology for various applications such as PEMFCs.

The major contributions of this study can be summarized as follows:

The authors successfully developed a method for deposition of $W_{18}O_{49}$ nanowires with controlled morphology. Further, $WS_2/W_{18}O_{49}$ nanocables were synthesized in a one-step process. A novel method was proposed for the synthesis of composite nanostructures based on NCNTs. It was shown that multi-component catalyst supports have great potential as catalyst supports in PEMFCs, affecting the electronic structure of Pt catalysts. TiO_2 decorated NCNTs with controlled diameters were developed through a combination of CVD and magnetron sputtering. Metal silicide complex nanostructures were synthesized using a CVD method and a growth mechanism based on silica sheath formation of certain crystal planes was proposed. This method can be expanded for the synthesis of other metal silicide and oxide nanostructures.

8.2   Future perspective

Despite the advances shown in this thesis, many issues remain unsolved. Future work could be focused on the following aspects:

- In this thesis, it was shown that doping of nanostructures, for example sulfur doping of tungsten oxide nanowires, is a suitable method for the synthesis of nanostructures with controlled morphology and composition. Similar methods can be developed for the synthesis of other metal oxide and carbide nanostructures. Further, since doping of nanostructures involves a change in the surface chemistry of nanostructures, it is noteworthy to study the electrochemical properties of doped and pristine nanostructures as electrocatalysts for PEMFC applications.

- The method developed in this research for the synthesis of composite nanostructures opens a path to development of new type nanostructures such as oxide, silicide, carbide and organic thin films. These composite nanostructures can be used in various applications such as PEMFCs.

- In the preparation of TiO_2 nanoparticle decorated NCNTs, the size of TiO_2 was kept constant. However, the synthesis method of these nanostructures provides the means of synthesis of TiO_2 nanoparticles with well controlled diameters. It is possible to study the dependence of various properties of these nanostructures on TiO_2 nanoparticle such as interaction of composite nanostructures with Pt catalysts.

- Metal silicide nanostructures due to their properties can be potential catalyst supports for PEMFCs. However, the presence of silicon oxide on these nanostructures can be an obstacle in the road for application of these nanostructures. Thus, development of a new synthesis method or a post treatment process for the removal of the silicon oxide layer would be of great interest.

- Study of interaction of between the catalyst support and Pt catalyst nanoparticles using X-ray absorption spectroscopy has revealed that the catalyst supports can greatly affect the electronic structure of Pt nanoparticles. To design a highly active electrocatalysts for PEMFCs, it is required to further understand the effect of novel catalyst support, especially multi component supports on electronic structure of the catalysts.

Curriculum Vitae

Name: Mohammad Norouzi Banis

Post-secondary Education and Degrees:

Sharif University of Technology
Tehran, Iran
2000-2005 B.Sc.

The University of Western Ontario
London, Ontario, Canada
2006-2008 M.Sc.

The University of Western Ontario
London, Ontario, Canada
2008- 2013 (expected) Ph.D.

Honours and Awards:

Ontario Graduate Scholarship in Science and Technology
2009-2010

Ontario Graduate Scholarship
2010-2011, 2011-2012

Graduate Thesis Award
2010-2011
2011-2012

Related Work Experience

Teaching Assistant
The University of Western Ontario
2006-2012

Publications:

[1] **Banis MN**, Zhang Y, Banis HN, Li R, Sun X, Jiang X and Nikanpour D "Controlled Synthesis and Characterization of Single Crystaline MnO Nanowires and Mn-Si Oxide and their Heterostructures by Vapor Phase Deposition." 2011 Chemical Physics Letters 501 470–474

[2] **Banis MN**, Zhang Y, Li R, Sun X, Jiang X and Nikanpour D "Vanadium Oxide Assisted Synthesis of Networked Silicon Oxide Nanowires and Their Growth Dependence." 2011 Particuology 9 458–464

[3] **Banis MN**, Meng X, Zhang Y, Cai M, Li R, and Sun X, "Spatial Sequential Growth of Various WSi$_2$ Networked Nanostructures and Mechanism" 2012, submitted to Journal of Materials Chemistry XX

[4]] **Banis MN**, Meng X, Zhang Y, Cai M, Li R, and Sun X, "Tailoring Growth of Single Crystalline Complex Ta$_5$Si$_3$ Nanostructures: From Networked Nanowires to Nanosheets" Submitted to General Motors for review.

[5] **Banis MN,** Sun S, Meng X, Zhang Y, Li R, Cai M, Sham TK, and Sun X, "TiSi$_2$O$_x$ Coated N-doped Carbon Nanotubes for the Oxygen Reduction Reaction in Proton Exchange Membrane Fuel Cells" 2012 submitted to Journal of Physical Chemistry C.

[6] **Banis MN,** Sun S, Zhang Y, Li R, Cai M, Sham TK, and Sun X, "TiO$_2$ Nanoparticle Decorated Nitrogen Doped Carbon Nanotubes as Pt Catalyst Support for Low Temperature Fuel Cells" Submitted to General Motors for review.

[8] **Banis MN**, Zhang Y, Li R, Sun X, "One Step Tunable Synthesis of Pristine Sulfur doped W$_{18}$O$_{49}$ Nanowires and WS$_2$/W$_{18}$O$_{49}$ Nanocables" submitted to General Motors for review.

[9] Chen Y, Wang J, Liu H, **Banis MN**, Li R, Sun X, Sham T-K, Ye S and Knights S "Nitrogen Doping Effects on Carbon Nanotubes and the Origin of the Enhanced Electrocatalytic Activity of Supported Pt for Proton Exchange Membrane Fuel Cells." 2011 Journal of Physical Chemistry C 115 3769–3776

[10] Li X, Meng X, Liu J, Geng D, Zhang Y, Banis MN, Li Y, Li R, Sun X, Cai M, Verbrugge M, "Tin Oxide with Controlled Morphology and Crystallinity by Atomic Layer Deposition onto Graphene Nanosheets for Enhanced Lithium Storage" 2012 Advanced Functional Materials 22 1647–1654

[11] Li Y, Wang J, Zhang Y, **Banis MN**, Liu J, Geng D, Li R and Sun X "Facile Controlled Synthesis and Growth Mechanisms of Flower-like and Tubular MnO$_2$ Nanostructures by Microwave-assisted Hydrothermal Method." 2012 Journal of Colloid and Interface Science 369 123–128

[12] Li Y, Wang J, Li X, Geng D, **Banis MN**, Li R and Sun X "Nitrogen-doped Graphene Nanosheets as Cathode Materials with Excellent Electrocatalytic Activity for High Capacity Lithium-oxygen Batteries" 2012 Electrochemistry Communications 18 12–15

[13] Liu J, Meng X, Hu Y, Geng D, **Banis MN**, Cai M, Li R and Sun X "Controlled Synthesis of Zirconium Oxide on Graphene Nanosheets by Atomic Layer Deposition" 2012 submitted to Carbon

[14]   Liu J, Meng X, **Banis MN**, Cai M, Li R and Sun X "Crystallinity-Controlled Synthesis of Zirconium Oxide Thin Films on Nitrogen-doped Carbon Nanotubes by Atomic Layer Deposition." 2012 Journal of Physical Chemistry C 116 14656–14664

[15]   Meng X, Zhong Y, Sun Y, **Banis MN**, Li R and Sun X "Nitrogen-doped Carbon Nanotubes Coated by Atomic Layer Deposited SnO_2 with Controlled Morphology and Phase." 2011 Carbon 49 1133–1144

[16]   Meng X, Ionescu M, **Banis MN**, Zhong Y, Liu H, Zhang Y, Sun S, Li R and Sun X "Heterostructural Coaxial Nanotubes of CNT@Fe_2O_3 via Atomic Layer Deposition: Effects of Surface Functionalization and Nitrogen-doping." 2011 Journal of Nanoparticle Research 13 1207–1218

[17]   Meng X, Geng D, Liu J, **Banis MN**, Zhang Y, Li R and Sun X "Non-Aqueous Approach to Synthesize Amorphous/Crystalline Metal Oxide-Graphene Nanosheet Hybrid Composites." 2010 Journal of Physical Chemistry C 114 18330–18337

[18]   Saha MS, **Banis MN**, Zhang Y, Li R, Sun X, Cai M and Wagner FT "Tungsten Oxide Nanowires Grown on Carbon Paper as Pt Electrocatalyst Support for High Performance PEM Fuel Cells." 2009 Journal of Power Sources 192 330–335

[19] Wang J., Yang J., Zhang Y., Li Y., **Banis M. N.**, Li X., Li R., Sun X, Liang G, Gauthier M, "Interaction of Carbon Coating on $LiFePO_4$: Local Visualization Study of the Influence of Impurity Phases". 2012 Advanced Functional Materials In press.

[20]   Sun S, Zhang G, Geng D, Chen Y, **Banis MN**, Li R, Cai M and Sun X ""New Insight into the Conventional Replacement Reaction for the Large-Scale Synthesis of Various Metal Nanostructures and their Formation Mechanism**""** 2010 Chemistry - A European Journal 16 829–835

[21]   Zhang Y, Geng D, Liu H, **Banis MN**, Ionescu MI, Li R, Cai M and Sun X "Designed Growth and Characterization of Radially Aligned Ti_5Si_3 Nanowire Architectures." 2011 Journal of Physical Chemistry C 115 15885–15889

[22]   Zhang G, Sun S, **Banis MN**, Li R, Cai M and Sun X "Morphology-controlled Green Synthesis of Single Crystalline Silver Dendrites, Dendritic Flowers and Rods, and their Growth Mechanism. " 2011 Crystal Growth and Design 11 2493–2499

[23]   Zhou J, Wang J, Liu H, **Banis MN**, Sun X and Sham T-K "Imaging Nitrogen in Individual Carbon Nanotubes." 2010 Journal of Physical Chemistry Letters 1 1709–1713